**Deep Earth Seismic Structure and Earthquake Source Processes from
Long Period Waveform Modelling**

by

Mark Paul Panning

B.S. (Indiana University) 1999

A dissertation submitted in partial satisfaction of the
requirements for the degree of
Doctor of Philosophy

in

Geophysics

in the

GRADUATE DIVISION
of the
UNIVERSITY of CALIFORNIA at BERKELEY

Committee in charge:

Professor Barbara Romanowicz, Chair
Professor Douglas Dreger
Professor David Brillinger

Fall 2004

The dissertation of Mark Paul Panning is approved:

_____

Chair   Date

_____

                                               Date

_____

                                               Date

University of California at Berkeley

Fall 2004

Deep Earth Seismic Structure and Earthquake Source Processes from Long Period Waveform Modelling

Abstract

Deep Earth Seismic Structure and Earthquake Source Processes from Long Period
Waveform Modelling

by

Mark Paul Panning

Doctor of Philosophy in Geophysics

University of California at Berkeley

Professor Barbara Romanowicz, Chair

We model long-period seismic waveforms to investigate both the deep Earth ve-
locity structure as well as earthquake source parameters. We utilize a normal mode-
based perturbation approach to model and invert a global dataset of 3 component
long-period seismic waveforms. The approach, which has been used for modelling
isotropic velocity structure, is extended for modelling radial anisotropy, which de-
scribes an anisotropic medium with a vertical axis of symmetry. A model for shear
velocity anisotropy near the core-mantle boundary is developed, and the stability and
significance of the fit to the data is analyzed. The model has important implications
for relations between flow and observable seismic anisotropy in this important thermal,
chemical, and mechanical boundary layer. This modelling approach is extended to a
multiple iteration inversion appropriate for a non-linear problem, and the anisotropic
structure of the whole mantle is examined. Tests of the stability of the model and the
influence of assumptions made in the modelling process are examined. Relations be-
tween mantle flow and seismic anisotropy are examined for a variety of depth ranges.
We also perform inversions for earthquake source parameters using the same wave-
form modelling approach, using the improved velocity model. Small, but systematic,
relocations of events are observed, as well as small perturbations to the orientation of
the mechanisms, and the updated sources result in significant improvement in fit to

the data. We also use a finite-difference approach to model regional, rather than tele-seismic, long-period waveforms to determine the significance of observed volumetric components of earthquakes in a volcanic region of eastern California.

Professor Barbara Romanowicz
Dissertation Committee Chair

Contents

List of Figures

List of Tables

Acknowledgements

Like nearly everything else in my life, I had no idea what I was getting into when I started as a graduate student in Berkeley in 1999. I had no specific project, no specific advisor, and no real plan except trying to add the letters Ph.D. after my name. Therefore I obviously needed a lot of help along the way.

I need to thank my committee members, Barbara Romanowicz, Doug Dreger, and David Brillinger. Dr. Brillinger was almost a sight-unseen addition to my orals committee, and a professor of statistics, a subject in which I was under-educated. He was obviously a source of a lot of stress for me at that time. His good questions during the exam, and discussion afterwards, though, inspired me to try to use statistics in a more exact fashion than is sometimes the case for mantle tomography, which I believe we both think is important. He's also recently given me some pretty good advice on raising twins, as he has twin grandchildren. Doug Dreger was basically my co-advisor, particularly in the first few years, when we worked together on what became chapter 5 of the dissertation. He's also a great guy to play poker with, although I'm pretty certain I've always left with less money than I showed up with. It's good to see a faculty member who socializes well with the graduate students, whether at a poker or pool game, or just at Triple Rock for the first Monday of the month. Barbara has turned out to be an amazing advisor. On paper, having an advisor who is simultaneously department chair, director of the Seismological Laboratory, and frequent traveller to Europe with several graduate students to supervise sounds like a recipe for disaster. Somehow, though, she always responded to questions promptly, and was an active part of all my research, even if sometimes only by email. I'm also quite certain that we had more group and individual research meetings than many of the faculty members here at Berkeley with far less time commitments managed.

Several other faculty members, researchers, and grad students in the department were helpful in one way or another as well. So much of my research was collaborative with Yuancheng Gung, I certainly could not have done it without him. I also collaborated with Hrvoje Tkalčić on the research of chapter 5. The other students in Barbara's research group, Ludovic, Charles, Chaincy, Junkee, Akiko, and Aimin

helped me out many times. I enjoyed T.A.ing classes with Rudy Wenk, Chi Wang, and Peggy Hellweg. The researchers here in BSL were always good people to talk with about my research and other areas of seismology as well, particularly Lind Gee, Bob Uhrhammer, Bob Nadeau, Rick McKenzie, and Pete Lombard. My two days of "field work" with Wade Johnson, John Friday, and Bill Karavas were also a good time, if a little brief compared with some other Earth scientists' field experience.

I should thank the faculty of the Department of Geological Sciences at Indiana University, who got me into this field in the first place, and encouraged me to come to Berkeley for grad school. I particularly would like to thank Abhijit Basu, Al Rudman, Jim Brophy, and Gary Pavlis.

The current and former students and postdocs here definitely kept me sane (or sometimes not). This is too long a list of people for me to hope to get it right, but I'll make a quick attempt. I have to thank Matt, Mo, Doug, Dave, Bunny, Dick, Wade, Karrie, Sarah, Elowyn, Jellinek, Lisa, Chris, Kim, Roland (XL and XS), Thijs, Laurent and many others I'm probably neglecting.

Getting away from the department, there were a lot of friends from my pre-Berkeley life that helped me make it through the last 5 years. The old Columbus crew of friends has been amazingly constant, although no longer geographically contiguous. Clint, Brian, Keyvan, Tom, and David have been good friends for far longer than I probably deserve. Drew, whom I somehow didn't meet until after Columbus, even has made it out to become a fellow East Bay resident and coffee shop companion.

Of course, the most important anchor through all this is my family, which has grown significantly during this time. Emily Angyus (now Panning) was brave enough to move out to a place where she had no job or contacts to live with a guy making no money in the most expensive area in the country, and quickly found a good job to support our luxurious lifestyle, and pay for our beautiful wedding on August 4th, 2002. And now she's brave enough to face raising our brand new twin daughters, Elsa Claire and Lillian Ruth, who held off being born just long enough for me to get a complete draft to my committee members before September 14, 2004. I can't imagine how she's doing it, because they're exhausting me, and I didn't have to be pregnant with them, and I'm not feeding them yet! I can't believe how much my life has

changed for the better since I moved out here back in the 20th century. My parents, Ron and Kathy Panning, have also of course been very supportive and helpful both in my academic and personal life, and I literally wouldn't be here without them, both in the sense of being my parents, as well as being the people who moved me out here from Indiana 5 years ago. I should also thank my in-laws, John and Melissa Angyus, who not only raised a wonderful daughter, but were unbelievably helpful in helping us take care of two newborn twin girls who had us at a loss while I was finishing up the final revisions of this dissertation.

Anything that takes as long to finish as a Ph.D. dissertation certainly requires a lot of help along the way, and of course there are a lot of people I need to thank, some of which I almost certainly forgot. To those I left out, I apologize profusely.

Chapter 1

Introduction

In this dissertation, we apply the modelling and inversion of long-period seismic waveforms to look at deep Earth anisotropic velocity structure as well as earthquake source processes on the global and regional scale.

In chapter 2, we review the theory behind the waveform modelling used. Sections 2.1-2.3 illustrate the development of the perturbation-based mode-coupling theory used in chapters 3 and 4. We progress from the equations describing the normal modes of a simple particle system to a simple, spherically symmetric Earth model. From there we discuss the effects of introducing lateral heterogeneity using first order perturbation theory. Although this approach allows robust determination of seismograms and their partial derivatives with respect to model parameters, it is expensive computationally. Therefore, in section 2.3, we review the derivation of an asymptotic calculation, *NACT*. In section 2.4, we discuss how to apply this approach to a radially anisotropic model with our desired final parameterization. Other modifications to the seismogram calculated in a spherically symmetric model are discussed in section 2.5. Finally, in section 2.6 we discuss the finite-difference approach, which we apply to model long-period waveforms for a regional-scale model with very heterogeneous velocity structure in chapter 5.

The normal-mode based waveform modelling techniques of chapter 2 are applied to develop a model of anisotropic shear velocity structure near the core-mantle boundary in chapter 3. This is a region of the mantle with ample obervations of anisotropy on fine, regional scales, but little work done on global-scale anisotropic structure.

Our resulting model has a strong spherically symmetric anisotropic signature with horizontally polarized shear wave velocity greater than that for vertically polarized waves. The strongest deviations from this signature are associated with large-scale low velocity regions under the Pacific and Africa, which are commonly called superplumes. We compare these results with previous more localized studies of shear anisotropy in the lowermost mantle, and perform some tests to determine how well-resolved and robust our results are in this depth range. The pattern suggests anisotropy generated in the predominantly horizontal flow of a mechanical boundary layer at the base of the mantle, analogous to the strong spherically symmetric anisotropic signature of the uppermost mantle. The deviations near the superplumes suggest a change of signature due to the onset of vertical flow at the large-scale upwellings. Chapter 3 has been published in *Science* under the reference [*Panning and Romanowicz,* 2004a].

In chapter 4, the modelling techniques of chapter 3 are extended to develop a multiple iteration model of radially anisotropic shear velocity structure in the whole mantle. As the inverse problem is non-linear, an iterative inversion is required to ensure that we achieve the best fit to the dataset. We also invert for the source mechanisms for the events in our dataset, as the waveforms observed depend on both the velocity structure and the earthquake source mechanism. Given the new source parameters, we perform two more iterations of the velocity inversion to obtain our final model.

We examine the resultant model in a variety of depth ranges, and quantitatively and qualitatively relate the observed anisotropy with the flow of the convecting mantle. Notably, we observe a horizontal flow signature at different depths beneath oceans and continents, as well as a vertical flow signature under mid-ocean ridges with strength of anisotropy correlated to surface spreading rates. In the transition zone, an anisotropic

pattern seems to correlate with some subducting slab regions, particularly in the western Pacific. We also confirm and further explore the reliability of the anisotropic pattern of the core-mantle boundary region discussed in chapter 3. We relate this observed signature to recent developments in experimental and theoretical mineral physics. We also make several tests about the effects of our modelling assumptions on our final model, as well as examining the resolution and errors of our dataset.

We also inverted for the source parameters of the events in our dataset. More than 80% of the events had sufficient coverage to have a stable inversion that showed improvement in fit to the data. In general, the changes in source parameters from published mechanisms using longer-period data and a simpler velocity model were small, but resulted in significant improvement in fit for the whole dataset. Initial tests showed the inversion method introduced some bias in the determination of event magnitude, so we fixed the scalar seismic moment of each event for the final source inversions. We examined the revised models to see if the new velocity model imposed any systematic relocations, and several events in the major circum-Pacific subduction zones showed small but non-random relocations. After the source parameters of the dataset were updated, and the data weighting values were recalculated, two more iterations of the velocity model were performed to converge on the final model. The final model, SAW16B16-AN, with the revised source parameters, showed a variance reduction of 55.7% over the whole dataset compared with 45.6% for the pre-source inversion velocity model. Chapter 4 will be submitted to *Geophysical Journal International* under the reference [*Panning and Romanowicz,* 2004b].

Long period waveforms can also be used to look at the tradeoffs between source mechanisms and velocity structure on a regional basis, although the normal mode based approach of chapters 3 and 4 are no longer applicable. In chapter 5, we analyze the effects on waveforms of the strongly heterogeneous velocity structure near the volcanic region of Long Valley in Eastern California. Previous studies have shown evidence that the mechanisms of some events in earthquake swarms in 1980 and the late 1990's are not adequately described by a simple double-couple fault dislocation model. Re-

cent work with a regional waveform moment tensor inversion scheme showed that several events even contained terms related to volumetric expansion during the earthquake source process. However, this inversion scheme only modelled waveforms in a simple 1D layered velocity model. To determine whether the complex 3D velocity structure in the Long Valley region leads to biases in the waveform inversion approach, we use a finite-difference code to model waveforms propagating through a regional tomographic model with a series of known sources. These waveforms were then inverted using simplified 1D models to determine whether spurious volumetric terms are introduced in the recovered source mechanisms. Our work showed that unmodelled 3D structure could lead to incorrect recovery of non-double-couple component, but was unlikely to lead to the large volumetric component observed for some events in the late 1990's. Chapter 5 has been published in *Geophysical Research Letters* under the reference [*Panning et al.,* 2001].

Chapter 2

Theoretical background

In chapters 3 and 4, we use asymptotic normal mode coupling theory to model long period seismic waveforms. In this chapter, we review and develop the formalism necessary for this approach. In section 2.1 we start from a simple model of a system of particles, and develop the formalism needed to calculate seismograms using the superposition of normal modes in a simple, spherical Earth model. In section 2.2, we extend this theory to a model with slight deviations from sphericity, using a first order perturbation approach. Although the method developed is robust, it is computationally expensive, so in section 2.3, we discuss asymptotic calculations of the mode-coupling in an aspherical Earth model, which we use to model waveforms in chapters 3 and 4. In section 2.4, we develop sensitivity kernels neccessary to model a radially anisotropic Earth. We discuss the effects of other deviations from the simple spherical model in section 2.5, and in section 2.6, we briefly discuss the numerical approach to waveform modelling used in chapter 5.

2.1 Normal mode summation in a simple, spherical Earth model

Any finite body, from a guitar string to the Earth, will respond to mechanical forcing by excitation of oscillations of discrete frequencies and spatial distributions. The total motion of the body can be expressed as a superposition of these normal modes. Here we review the formalism used to synthesize seismograms with normal mode summation for an SNREI (spherical, non-rotating, elastic and isotropic) Earth model excited by a point source, such as an earthquake.

To illustrate the development of a normal mode formalism, we follow *Gilbert*, [1971] and start by considering a particle system. Consider a conservative system of N particles in a small oscillation about a state of stable equilibrium. The change in internal forces between particles is assumed to be a linear function of displacement, so the equation for the conservation of linear momentum can be expressed as

$$m_\alpha \frac{d^2 \mathbf{u}_\alpha(\mathbf{t})}{dt^2} + \sum_{\beta=0}^{N} \mathbf{V}_{\alpha\beta} \cdot \mathbf{u}_\beta = \mathbf{F}_\alpha, \qquad (2.1)$$

where $\mathbf{u}_\alpha$ is the displacement of the αth particle, $\alpha = 1, ..., N$, m_α is its mass, $\mathbf{f}_\alpha$ is the force applied to it, and $\mathbf{V}_{\alpha\beta}$ is the symmetric, positive definite potential energy matrix representing the internal restoring forces.

Given each particle's 3 degrees of freedom, it can be shown [*Gilbert*, 1971] that the displacement of a particle, given an initial force that is a step function in time and a point source in space, can be described by the superposition of $3N$ eigenvectors, or normal modes. Therefore the motion of any particle depends only on the total excitation of the normal modes by the initial force,

$$\mathbf{u}_\alpha(t) = \sum_{j=1}^{3N} \left(\sum_\beta {}_j\mathbf{u}_\beta^* \cdot \mathbf{F}_\beta \right) {}_j\mathbf{u}_\alpha \frac{1 - \cos\omega_j t}{\omega_j^2}, \tag{2.2}$$

where j is a mode index, ${}_j\mathbf{u}_\alpha$ and ω_j are the eigenvector and eigenfrequency of the jth normal mode, and $(\sum_\beta {}_j\mathbf{u}_\beta^* \cdot \mathbf{F}_\beta)$ is the excitation of the jth mode by the initial force system. The asterisk denotes complex conjugation.

To extend the discrete particle system described above to a mass described as a continuum, such as the Earth, we replace the particle sum over β by a volume integral taken over the whole Earth. (2.2) becomes

$$\mathbf{u}(\mathbf{x}, t) = \sum_j \left(\int_V \mathbf{u}_j^*(\xi) \cdot \mathbf{f}(\xi)\, dv \right) \mathbf{u}_j(\mathbf{x}) \frac{1 - \cos\omega_j t}{\omega_j^2}, \tag{2.3}$$

where j denotes the jth normal mode of the whole Earth, and $\mathbf{f}$ is the body force per unit volume. Because we are treating the Earth as a continuum, the sum in (2.3) is now an infinite sum, but it converges because of the factor ω_j^{-2} [$Rayleigh$, 1945]. The modes in (2.3) are normalized by

$$\int_V \rho(\xi)\mathbf{u}_j^*(\xi) \cdot \mathbf{u}_k(\xi)\ dv = \delta_{jk}, \tag{2.4}$$

where ρ is the density.

In a spherical Earth, we can express the eigenvectors for displacement in a general form

$$\mathbf{u}_i(\mathbf{x}) = {}_nU_l^m(r)Y_l^m(\theta, \phi)\hat{r} + {}_nV_l^m(r)\nabla_1 Y_l^m(\theta, \phi) + {}_nW_l^m(r)\hat{r} \times \nabla_1 Y_l^m(\theta, \phi), \tag{2.5}$$

where (n, l, m) are the radial, angular and azimuthal orders of a mode, (r, θ, ϕ) are spherical coordinates of $\mathbf{x}$, $\hat{r}$ is the unit vector in the direction of increasing radius,

Y_l^m are fully normalized spherical harmonics [*Edmonds*, 1960], $_nU_l^m$, $_nV_l^m$ and $_nW_l^m$ are the radial eigenfunctions for the Earth, and ∇_1 is the surface gradient operator:

$$\nabla_1 Y_l^m = \frac{\partial Y_l^m}{\partial \theta}\hat{\theta} + \frac{1}{\sin(\theta)}\frac{\partial Y_l^m}{\partial \phi}\hat{\phi}. \tag{2.6}$$

It has been shown (e.g. chapter 8 of *Aki and Richards* [2002]) that when (2.5) is substituted into the equations of motion for an SNREI Earth model, the equations defining U and V (neglecting subscripts for convenience) are decoupled from those describing W. This decoupling means the normal modes can be divided into two categories: spheroidal modes, for which $W = 0$, and toroidal modes, for which $U = V = 0$. Furthermore, the equations have no dependence upon azimuthal order m, meaning that for each combination of radial and angular order n and l, there exist $2l + 1$ degenerate modes (singlets) with the same eigenfrequency (referred to as the multiplet frequency), as well as the same radial eigenfunctions U, V and W.

For seismology, it is useful to have the initial forcing term in (2.3) to be an earthquake. The equivalent body force system of a shear dislocation, such as an earthquake, can be expressed concisely using moment tensors [*Aki and Richards*, 2002]

$$f_p(\xi, t) = -\mathbf{M}_{pq}(t)\ \frac{\partial}{\partial \xi_q}\delta(\xi - \mathbf{x}_s), \tag{2.7}$$

where the source volume is considered to be small relative to the wavelengths of interest, and so can be treated as a point source.

Assuming $\mathbf{M}$ acts as a step function in time, (2.7) can be directly subtituted into the excitation term in (2.3)

$$\begin{aligned} \int_V \mathbf{u}_j^*(\xi) \cdot \mathbf{f}(\xi)\, dv &= -\mathbf{M}_{pq}\int_V (\mathbf{u}_j)_p^*(\xi)\frac{\partial}{\partial \xi_q}\ \delta(\xi - \mathbf{x}_s)\, dv(\xi) \\ &= (e_j)_{pq}^*(\mathbf{x}_s)\mathbf{M}_{pq}, \end{aligned} \tag{2.8}$$

where $(e_j)_{pq}$ is the (pq) strain component of the jth normal mode, $e_{pq} = \frac{1}{2}(\partial u_p/\partial \xi_q + \partial u_q/\partial \xi_p)$. Substituting (2.8) into (2.3), and differentiating twice to convert displacement to acceleration, we obtain

$$\frac{\partial^2 \mathbf{u}}{\partial t^2}(\mathbf{x}, t) = \Re e \sum_j (-\mathbf{M} : \epsilon^*)(\mathbf{x}_s) \, \mathbf{u}_j(\mathbf{x}) \exp(i\omega_j t), \qquad (2.9)$$

where $\mathbf{u}_j$ and ω_j are, respectively, the spatial eigenvector and eigenfrequency of the jth mode, and $\mathbf{M} : \epsilon^*$ is tensor notation for the excitation term, $\sum_{pq} \mathbf{M}_{pq}(e_j)^*_{pq}$. The sum extends over all modes. To further simplify (2.9), we introduce the receiver vector, R_K^m, and the source vector, S_K^m [*Woodhouse*, 1983]:

$$R_K^m \equiv \mathbf{v} \cdot \mathbf{u}_K^m(\mathbf{x}), \qquad (2.10)$$

$$S_K^m \equiv -(\mathbf{M} : \epsilon^{m*})(\mathbf{x}_s), \qquad (2.11)$$

where K is the multiplet index, which incorporates overtone number n, angular order l, and mode type (toroidal/spheroidal mode); m is the azimuthal order of each singlet in multipler K, and $\mathbf{v}$ is the unit vector in the direction of seismic observation. With these definitions, (2.9) becomes the expression for the normal mode summation in an SNREI model

$$u_0(\mathbf{x}, t) = \Re e \sum_K \exp(i\omega_K t) \sum_{m=-l}^{l} R_K^m S_K^m, \qquad (2.12)$$

where $u_0 \, (= \mathbf{v} \cdot \frac{\partial^2 \mathbf{u}}{\partial t^2})$ is the $\mathbf{v}$ component of acceleration in a spherical symmetric Earth model. Note the eigenfrequency does not depend on the azimuthal order m, due to the degeneracy discussed above.

2.2 First-order perturbation in a slightly aspherical Earth

Now that we have a compact expression for the evaluation of seismograms in a simple Earth model, we need to extend the method to allow for lateral structure which slightly deviates from the spherically symmetric model. We use first-order perturbation theory to develop expressions for long-period seismograms in a slightly aspherical Earth model by summing normal modes [*Woodhouse*, 1983; *Tanimoto*, 1984].

The equation governing the displacement field $\mathbf{u}(\mathbf{x}, t)$ due to an earthquake may be written

$$(\mathcal{H} + \rho\partial_t^2)\mathbf{u} = \mathbf{f}, \tag{2.13}$$

where $\mathcal{H}$ is an integro-differential tensor operator representing the effects of the elastic restoring force and the gravitational force, ∂_t is the operator representing differentiation with respect to time, and $\mathbf{f}$ is the initial force system, which we earlier defined using the moment tensor for a point-source earthquake in (2.7).

We wish to convert (2.13) into a matrix equation. To do so, we first express the displacement as a sum over normal modes, as in (2.3),

$$\mathbf{u}(\mathbf{x}, t) = \sum_j a_j(t)\mathbf{u}_j(\mathbf{x}), \tag{2.14}$$

where $\mathbf{u}_j$ are the normal modes of the spherically symmetric model as in section 2.1, and the mode excitation and time dependence are now incorporated into the term $a_j(t)$.

Woodhouse [1983] shows that the solution to (2.13) for an initially quiescent Earth

model ($\mathbf{a}(0) = \partial_t \mathbf{a}(0) = 0$, where $\mathbf{a}(t) = \{a_j(t)\}_{j=0}^{\infty}$) is given through the coefficients $\{a_j\}$, which can be expressed as a matrix equation

$$\mathbf{a}(t) = \Re e \left(\int_0^t \mathbf{X}^{-2} \left(\mathbf{I} - \exp\left[i(t - \tau)\mathbf{X}\right] \right) \mathbf{P}^{-1} \partial_t \mathbf{s}(\tau) \, d\tau \right), \qquad (2.15)$$

where $\mathbf{I}$ is the identity matrix, and the elements of $\mathbf{P}$, $\mathbf{H}$ and $\mathbf{s}$ are given by

$$H_{jk} \equiv \int_V \mathbf{u}_j^* \cdot \mathcal{H} \, \mathbf{u}_k \, dv, \qquad (2.16)$$

$$P_{jk} \equiv \int_V \mathbf{u}_j^* \cdot \rho \, \mathbf{u}_k \, dv, \qquad (2.17)$$

$$s_j \equiv \int_V \mathbf{u}_j^* \cdot \mathbf{f} \, dv, \qquad (2.18)$$

and $\mathbf{X}$ is defined through $\mathbf{X}^2 \equiv \mathbf{P}^{-1}\mathbf{H}$.

For a step-function source, a particular component of acceleration, $u(t) = \mathbf{v} \cdot \partial_t^2 \mathbf{u}(\mathbf{x}_r, t)$, can be expressed as

$$u(t) = \Re e \{ \mathbf{R} \, \exp[i \, \mathbf{X} \, t] \mathbf{P}^{-1} \, \mathbf{S} \}, \qquad (2.19)$$

where $\mathbf{R}$ and $\mathbf{S}$ are the receiver and source vectors defined in (2.10) and (2.11). Note that in an SNREI model, (2.19) reduces to (2.12), as the normalization convention then mandates that $\mathbf{P} = \mathbf{I}$, and $\mathbf{X}$ reduces to a diagonal matrix of the eigenfrequencies. As noted by *Woodhouse* [1983], although the formal expression (2.19) is an exact solution to (2.13), it is not practical for computation. In the following, we apply perturbation theory to derive an approximate expression.

A slightly aspherical Earth can be thought of as a small perturbation of the spherical symmetric reference Earth model, e.g., $\rho = \rho^{(0)} + \rho^{(1)}$. The superscript (0) refers to the reference model and superscript (1) to the small perturbation. In the same way, we

may approximate the operator $\mathbf{\Theta}$, by decomposing it into the sum of a reference term (evaluated for the reference model) and a small perturbation term: $\mathbf{\Theta} = \mathbf{\Theta}^{(0)} + \mathbf{\Theta}^{(1)}$, $\mathbf{\Theta} \in \{\mathbf{P}, \mathbf{H}, \mathbf{X}\}$. Then to first-order in the perturbation (i.e. second-order quantities are neglected), we have [*Woodhouse*, 1983]:

$$P_{jk}^{-1} = \left(P_{jk}^{(0)} + P_{jk}^{(1)}\right)^{-1} \approx I_{jk} - P_{jk}^{(1)}, \tag{2.20}$$

$$X_{jk} = X_{jk}^{(0)} + X_{jk}^{(1)} \approx \omega_j I_{jk} + \frac{Z_{jk}}{\omega_j + \omega_k}, \tag{2.21}$$

where $Z_{jk} \equiv H_{jk}^{(1)} - \omega_k^2 P_{jk}^{(1)}$. Using this notation, we express (2.19) to first order as

$$u(t) = \Re e \sum_{jk} R_j \left[\exp(iX_{jk}t) - \exp(i\omega_j t)P_{jk}^{(1)}\right] S_k. \tag{2.22}$$

(2.22) indicates that the aspherical structure introduces perturbations to the both the phase and amplitude of the normal modes of the reference model. The effect of the complex phase perturbation in the first term (X_{jk}) on the shape of waveforms increases with time, and eventually dominates that of the amplitude perturbation, which results from density perturbations $(P_{jk}^{(1)})$, which generally only affects the longest wavelengths. It is therefore common to neglect the effect of amplitude perturbation [*Woodhouse*, 1980; *Romanowicz*, 1987; *Li and Tanimoto*, 1993], which leaves:

$$u(t) = \Re e \sum_{jk} R_j \exp\left[it\left(\omega_j I_{jk} + \frac{Z_{jk}}{\omega_j + \omega_k}\right)\right] S_k. \tag{2.23}$$

As shown by *Tanimoto* [1984], (2.23) represents the first-order 'Born' solution to the displacement in a slightly heterogeneous Earth.

2.3 Nonlinear asymptotic coupling theory

Computing seismograms from (2.23) becomes very computationally expensive as the angular degree l of modes becomes large, and the number of coupled modes increases. Therefore, further approximations are required to allow for practical application to seismic tomography.

To zeroth-order in $1/l$, when only coupling along the same dispersion branch is considered, the approximated coupling effect is equivalent to path-average approximation (*PAVA*) [*Woodhouse & Dziewonski*, 1984], in which seismograms are sensitive only to the horizontally averaged structure along the great circle between the source and receiver [*Romanowicz*, 1987; *Park*, 1987]. *PAVA* has been shown to predict the perturbation of the seismogram well for fundamental mode surface waves, but is inaccurate for body waves, because it fails to describe the concentration of sensitivities to structure in the vicinity of the ray path [*Li and Tanimoto*, 1993].

To account for perturbation effects on body waves, we also need to include the across-branch coupling effects among modes. Under the assumption that heterogeneity is laterally smooth, using a short-time approximation, *Li & Tanimoto* [1993] linearized the exponential term in (2.23), and developed a formulation for calculating body wave seismograms. This is further improved by non-linear asymptotic coupling theory (*NACT*) [*Li and Romanowicz,* 1995], in which only across-branch coupling effects are linearized. Although we will not go through a rigorous derivation of this approach, we will summarize the important equations necessary for its application. Please refer to [*Li and Tanimoto*, 1993; *Li and Romanowicz,* 1995; *Mégnin*, 1999] for further details on the development of this theoretical approach.

Let us introduce apparent frequency shifts $\delta\omega_j$ which are the same for all the singlets belonging to the same multiplet and, generally speaking, are functionals of the locations of the source and receiver and of the given 3-D Earth model. We may then modify the phase terms in (2.23)

$$\omega_j I_{jk} + \frac{Z_{jk}}{\omega_j + \omega_j} \quad \Rightarrow \widehat{\omega}_j I_{jk} + \frac{\widehat{Z}_{jk}}{\omega_j + \omega_k}, \qquad (2.24)$$

where $\widehat{\omega}_j = \omega_j + \delta\omega_j$ and $\widehat{Z}_{jk} = Z_{jk} - 2\omega_j\omega_k\delta_{jk}$. The modified exponential term can be linearized as [*Li and Romanowicz,* 1995; *Mégnin,* 1999]:

$$\exp\left[it\left(\widehat{\omega}_j I_{jk} + \frac{\widehat{Z}_{jk}}{\omega_j + \omega_k}\right)\right] \quad \approx \quad \exp(i\widehat{\omega}_j t)I_{jk} - it\delta\omega_j \exp(i\widehat{\omega}_j t)$$
$$+ \quad Z_{jk}\frac{\exp(i\widehat{\omega}_j t) - \exp(i\widehat{\omega}_k t)}{(\omega_j + \omega_k)(\widehat{\omega}_j - \widehat{\omega}_k)}. \qquad (2.25)$$

In *NACT*, the contribution of along-branch and across-branch coupling effects are considered separately. We first derive the expression for *PAVA* seismogram. Using multiplet index K and azimuthal order index m, following *Woodhouse* [1983], we can define the apparent frequency shifts by

$$\delta\omega_K = \frac{\sum\limits_{mm'} R_K^m Z_{KK}^{mm'} S_K^{m'}}{2\omega_K \sum\limits_m R_K^m S_K^m}. \qquad (2.26)$$

It can also be defined as the average frequency shift over the path from source to receiver, and we will adopt this definition in what follows. This can be evaluated using the path average approximation,

$$\delta\omega_K \equiv \frac{1}{\widehat{SR}} \int_S^R \delta\omega_{local}^K d\phi, \qquad (2.27)$$

where $\delta\omega_{local}^K$ is the local frequency introduced by *Jordan* [1978] (please see (2.36) for definition), the integral is taken along the great circle from the source S to the receiver R, and $d\phi$ denotes the differential angular distance element. Note that the path here is the whole path from source to receiver, not just the minor arc (i.e. the integrtaion should be on the major arc for 2nd orbit phases, and include the appropriate number

of trips around the great-circle path for higher orbit phases). The *PAVA* seismogram is then expressed by

$$u_{pava}(t) = \Re e \sum_K A_K \exp(i\widehat{\omega}_K t), \tag{2.28}$$

where

$$A_K = \sum_m R_K^m S_K^m, \tag{2.29}$$

$$\widehat{\omega}_K = \omega_K + \delta\omega_K. \tag{2.30}$$

Using (2.28) and the modified phase terms in (2.25), we may rewrite (2.23)

$$\begin{aligned} u(t) &= \Re e \left[\sum_K A_K \exp(i\widehat{\omega}_K t) \right. \\ &\quad \left. - \sum_K it\, \delta\omega_K\, A_K \exp(i\widehat{\omega}_K t) + \sum_{KK'} A_{KK'} D_{KK'}(t) \right], \end{aligned} \tag{2.31}$$

where

$$A_{KK'} \equiv \sum_m R_K^m Z_{KK'}^{mm'} S_{K'}^{m'}, \tag{2.32}$$

$$D_{KK'}(t) \equiv \frac{\exp(i\widehat{\omega}_K t) - \exp(i\widehat{\omega}_{K'} t)}{(\omega_K + \omega_{K'})(\widehat{\omega}_K - \widehat{\omega}_{K'})}. \tag{2.33}$$

(2.31) expresses the seismogram in two parts. The first term on the right hand side is the *PAVA* seismogram, which is calculated in the same way as in a spherically symmetric model using a 1-D theory, with the eigenfrequencies $\widehat{\omega}_K$ evaluated for a model obtained by horizontally averaging structure along the great circle connecting

the source and receiver; while the other terms represent any further correction from across-branch couplings, for which we consider a linear approximation.

Because the evaluation of $A_{KK'}$ for $K \neq K'$ becomes rapidly impractical with increasing l, it is advantageous to derive an asymptotic approximation for $A_{KK'}$.

Because across-coupling effects are small unless $\omega_{K'}$ and ω_K are very close, we may write the frequency in $Z_{KK'}^{mm'}$, $\omega_{K'} \approx \frac{\omega_K + \omega_{K'}}{2} \approx \omega_{KK'}$, so that

$$Z_{KK'}^{mm'} = H_{KK'}^{(1)\,mm'} - \omega_{K'}^2\, P_{KK'}^{(1)\,mm'} \approx H_{KK'}^{(1)\,mm'} - \omega_{KK'}^2\, P_{KK'}^{(1)\,mm'}. \tag{2.34}$$

If lateral heterogeneities vary smoothly relative to the horizontal wavelength of modes, we can generalize the expansion for self coupling $(Z_{KK}^{mm'})$ introduced by *Woodhouse & Girnius* [1982], and approximate $Z_{KK'}^{mm'}$ as [*Romanowicz*, 1987]

$$Z_{KK'}^{mm'} = 2\,\omega_{KK'} \int_\Omega \delta\omega_{KK'}(\theta, \phi)\, Y_l^{m\,*}(\theta, \phi)\, Y_{l'}^{m'}(\theta, \phi)\, d\Omega, \tag{2.35}$$

where Ω is the unit sphere, and the local frequency $\delta\omega_{KK'}$ is

$$\delta\omega_{KK'} = \frac{1}{2\,\omega_{KK'}} \left[\int_0^a \delta\mathbf{m} \cdot \mathbf{M}_{KK'}(r) r^2\, dr - \sum_d r_d^2\, h_d\, H_{KK'}^d \right], \tag{2.36}$$

where a is the radius of the Earth, $\delta\mathbf{m}$ represents the heterogeneous perturbations to Earth structure, and h_d is the perturbation to the radius r_d of the dth discontinuity. The kernels $\mathbf{M}_{KK'}(r)$ and $H_{KK'}^d$ are given by *Woodhouse* [1980] for an isotropic model, and modified for anisotropy in section 2.4. The local frequency $\delta\omega_{local}^K$ in (2.27) is also calculated through (2.36) with $K = K'$.

After expressing the source and receiver vectors in generalized spherical harmonics [*Phinney and Burridge*, 1973], combining with (2.35), and using the addition theorem

for spherical harmonics, we can reduce (2.32) to an integral over associated Legendre functions. These can be further simplified by using an asymptotic (short-wavelength) approximation, and evaluating the integrals with a stationary-phase approximation [*Romanowicz & Roult*, 1986]. After these steps (discussed in more detail in [*Li and Romanowicz*, 1995; *Mégnin*, 1999; *Gung*, 2003]), we reduce the *NACT* seismogram to

$$u(t) = u_{pava}(t) + u_1(t) + \sum_K \sum_{K' \in \Gamma_K} D_{KK'}(t)E_{KK'}, \qquad (2.37)$$

where $u_1 = -\sum_K i\,t\,\delta\omega_K\,A_K\,\exp(i\widehat{\omega}_K t)$, Γ_K is the set of multiplets with eigenfrequencies $\omega_{K'} \geq \omega_K$, and the asymptotic scattering term $E_{KK'}$ is given by:

$$E_{KK'}(t) \equiv \frac{1}{2\pi}\left[Q^{(1)}_{KK'}\int_0^{2\pi}\delta\omega^2_{KK'}\cos(j\phi)d\phi + Q^{(2)}_{KK'}\int_0^{2\pi}\delta\omega^2_{KK'}\sin(j\phi)d\phi\right], \quad (2.38)$$

where $Q^{(1)}_{KK'}$ and $Q^{(2)}_{KK'}$ are functionals of the source and receiver, and ϕ is the angular distance along the great circle path (between the source and receiver). $Q^{(1)}_{KK'}$ and $Q^{(2)}_{KK'}$ are given by

$$Q^{(i)}_{KK'} \equiv (-1)^{i+1}\left(P^{(i)}_{KK'} + P^{(i)}_{K'K}\right), \qquad (2.39)$$

$$P^{(i)}_{KK'} \equiv g^{(1)}_l(\Delta)T^{(i)}_{KK'} + (-1)^i g^{(2)}_l(\Delta)T^{(i)}_{KK'}, \qquad (2.40)$$

$$g^{(1)}_l(\Delta) \equiv \sqrt{\frac{2}{\kappa\pi\sin\Delta}}\cos\left(\kappa\Delta - \frac{\pi}{4}\right), \qquad (2.41)$$

$$g^{(2)}_l(\Delta) \equiv \sqrt{\frac{2}{\kappa\pi\sin\Delta}}\sin\left(\kappa\Delta - \frac{\pi}{4}\right), \qquad (2.42)$$

$$T^{(1)}_{KK'} \equiv \sum_{NM} i^{N+M} R^N_K S^M_{K'}\cos\left(\frac{N+M}{2}\pi\right), \qquad (2.43)$$

$$T_{KK'}^{(2)} \equiv \sum_{NM} i^{N+M} R_K^N S_{K'}^M \sin\left(\frac{N+M}{2}\pi\right), \tag{2.44}$$

where Δ is the angular distance between source and receiver, and N and M are quantities related to the expansion of the source and receiver vectors in generalized spherical harmonics [*Woodhouse & Girnius*, 1982] with N ranging from -1 to 1, and M ranging from -2 to 2.

2.4   Anisotropic sensitivity kernels

The perturbed coupled frequency shift in (2.36), which is critical in *NACT* calculations, utilizes kernels defined in *Woodhouse*, [1980]. These, however, are only valid for an isotropic model, and need to be modified for use with a radially anisotropic model, such as the 1D PREM [*Dziewonski and Anderson*, 1981], and the 3D models developed in chapters 3 and 4.

We choose to parameterize our models in terms of radial anisotropy, which can be described with 5 elastic parameters, most commonly desribed as the Love parameters: A, C, L, N and F [*Love*, 1927]. Radial anisotropy is dicussed in more detail in chapters 3 and 4.

We wish to extend the kernels from *Woodhouse*, [1980] to an anisotropic medium (e.g. *Mochizuki*, [1986]; *Romanowicz and Snieder*, [1988]). It is shown in Appendix C of *Li and Romanowicz*, [1996], that with a model parameterized in spherical harmonics and under the assumption of smooth structure, we can express (2.36) as

$$\delta\omega_{KK'} = \frac{1}{2\,\omega_{KK'}}\left\{\sum_{st}\left(\int_0^a [\delta z_{st}]\, r^2\, dr - \sum_d r_d^2\, h_d^{st}\, [z_s]_-^+\right)\right\}, \tag{2.45}$$

where s and t refer to the angular and azimuthal order of the spherical harmonics expansion of the model, and

$$\delta z_{st} = \delta A_{st}\bar{A}_s + \delta C_{st}\bar{C}_s + \delta L_{st}\bar{L}_s + \delta N_{st}\bar{N}_s + \delta F_{st}\bar{F}_s + \delta\rho_{st}R_s^{(2)} \tag{2.46}$$

and

$$z_s = A\tilde{A}_s + C\tilde{C}_s + L\tilde{L}_s + N\tilde{N}_s + F\tilde{F}_s + \rho R_s^{(1)}. \tag{2.47}$$

In (2.46), δA_{st}, δC_{st}, δL_{st}, δN_{st}, δF_{st} and $\delta\rho_{st}$ refer to the coefficients in the spherical harmonic expansion of the perturbation of the 5 anisotropic parameters and density. In (2.47), A, C, L, N, F and ρ refer to the values of those parameters as a function of depth in the reference model. The kernels $R_s^{(1)}$ and $R_s^{(2)}$ are defined in *Woodhouse*, [1980], and the other kernels, $\bar{A}_s$, $\bar{C}_s$, $\bar{L}_s$, $\bar{N}_s$, $\bar{F}_s$; and $\tilde{A}_s$, $\tilde{C}_s$, $\tilde{L}_s$, $\tilde{N}_s$, $\tilde{F}_s$ are given by

$$\bar{A}_s = Aff'B_{l'sl}^{(0)+} \tag{2.48}$$

$$\bar{C}_s = C\dot{U}\dot{U}'B_{l'sl}^{(0)+} \tag{2.49}$$

$$\bar{L}_s = L\left((XX' + ZZ')B_{l'sl}^{(1)+} + (ZX' - XZ')iB_{l'sl}^{(1)-}\right) \tag{2.50}$$

$$\bar{N}_s = N\left(-ff'B_{l'sl}^{(0)+} + \frac{1}{r^2}(VV' + WW')B_{l'sl}^{(2)+} + \frac{1}{r^2}(WV' - VW')iB_{l'sl}^{(2)-}\right) \tag{2.51}$$

$$\bar{F}_s = F(\dot{U}f' + \dot{U}'f)B_{l'sl}^{(0)+} \tag{2.52}$$

$$\tilde{A}_s = ff'B_{l'sl}^{(0)+} \tag{2.53}$$

$$\tilde{C}_s = -\dot{U}\dot{U}'B_{l'sl}^{(0)+} + \frac{1}{r}(V\dot{U}'B_{ll's}^{(1)+} + V'\dot{U}B_{l'ls}^{(1)+}) + \frac{1}{r}(\dot{U}W' - \dot{U}'W)iB_{l'sl}^{(1)-}) \tag{2.54}$$

$$\tilde{L}_s = (XX' + ZZ' - \dot{V}X' - \dot{V}'X - \dot{W}Z' - \dot{W}'Z)B_{l'sl}^{(1)+}$$
$$+(ZX' + XZ' - \dot{V}Z' - \dot{V}'Z - \dot{W}X' - \dot{W}'X)iB_{l'sl}^{(1)-} \tag{2.55}$$

$$\tilde{N}_s = -ff'B_{l'sl}^{(0)+} + \frac{1}{r^2}(VV' + WW')B_{l'sl}^{(2)+} + \frac{1}{r^2}(WV' - VW')iB_{l'sl}^{(2)-} \tag{2.56}$$

$$\tilde{F}_s = \frac{1}{r}(Vf'B_{ll's}^{(1)+} + V'fB_{l'ls}^{(1)+}) + \frac{1}{r}(fW' - Wf')iB_{l'sl}^{(1)-} \tag{2.57}$$

with

$$f = \frac{1}{r}[2U - l(l+1)V] \tag{2.58}$$

$$X = \dot{V} + \frac{1}{r}(U - V) \tag{2.59}$$

$$Z = \dot{W} - \frac{1}{r}W \tag{2.60}$$

and

$$B_{l'sl}^{(N)\pm} = \frac{1}{2}(1 \pm (-1)^{l'+s+l}) \left[\frac{(l'+N)!(l+N)!}{(l'-N)!(l-N)!}\right]^{1/2} (-1)^N \begin{pmatrix} l' & s & l \\ -N & 0 & N \end{pmatrix}, \tag{2.61}$$

where

$$\begin{pmatrix} l' & s & l \\ -N & 0 & N \end{pmatrix}$$

is in Wigner $3-j$ notation [*Edmonds*, 1960]. U, V and W are the radial eigenfunctions of each mode, and the primes refer to the properties of the second mode in each coupled pair. Note that (2.48)-(2.52) differ from equations C4-C8 in *Li and Romanowicz,* [1996], as we assume here that the model perturbations are relative, dimensionless perturbations (i.e. δA_{st} refers to the coefficient in the spherical harmonic expansion of $\delta \ln A$) rather than absolute perturbations of the elastic values.

We wish to reparameterize, as described in chapters 3 and 4, in terms of Voight average V_P and V_S, and the three anisotropic parameters ξ, ϕ and η. We use this parameterization due to practical concerns of the inversion process. In general, given

sufficient coverage, an iterative least-squares inversion, such as the approach we use in our modelling [*Tarantola and Valette,* 1982] has better resolution of the 3D pattern of structure than the amplitude of that structure, due to the *a priori* damping scheme applied. If we choose a parameterization such as the Love coefficients, the anisotropy, which is the quantity we are interested in, is defined by the differences between inverted parameters. Interpreting the difference of two terms with uncertainties in amplitude from the damping procedure is very problematic both in terms of amplitude and even sign, so we choose to invert directly for the anisotropic parameters.

To define the Voight average equivalent isotropic velocities, we start from the definition of the equivalent Voight average bulk and shear moduli in a radially anisotropic medium [*Babuska and Cara,* 1991],

$$\kappa = \frac{1}{9}(C + 4A - 4N + 4F) \tag{2.62}$$

$$\mu = \frac{1}{15}(C + A + 6L + 5N - 2F). \tag{2.63}$$

The isotropic velocities are defined in terms of the bulk and shear moduli,

$$V_P^2 = \frac{\kappa + \frac{4}{3}\mu}{\rho} \tag{2.64}$$

$$V_S^2 = \frac{\mu}{\rho}, \tag{2.65}$$

and so we can substitute (2.62) and (2.63) into (2.64) and (2.65) to obtain

$$\rho V_P{}^2 = \frac{1}{15}(3C + (8 + 4\eta)A + 8(1 - \eta)L) \tag{2.66}$$

$$\rho V_S{}^2 = \frac{1}{15}(C + (1 - 2\eta)A + (6 + 4\eta)L + 5N), \tag{2.67}$$

where

$$\eta = \frac{F}{A - 2L},\tag{2.68}$$

which is equal to 1 in an isotropic model, and effectively describes anisotropy in the Lamé parameter λ. The relationships between the Love coefficients and observable seismic velocities can be defined as

$$A = \rho V_{PH}^2 \tag{2.69}$$

$$C = \rho V_{PV}^2 \tag{2.70}$$

$$L = \rho V_{SV}^2 \tag{2.71}$$

$$N = \rho V_{SH}^2, \tag{2.72}$$

where V_{PH} and V_{PV} are the velocities of horizontally and vertically polarized P waves, and V_{SH} and V_{SV} are the horizontal velocities of horizontally and vertically polarized S waves. Note that the average isotropic velocities defined in (2.66) and (2.67) depend on all four of the observable seismic velocities in (2.69)-(2.72), as well as η. However, in the case of small anisotropy which we assume for our perturbation-based approach, we can assume $\eta \simeq 1$, and make the first order approximation to neglect the quantity $C-A$ in comparison with $10L+5N$ in (2.67), and simplify the Voight average velocities to

$$V_S^2 = \frac{2L + N}{3\rho} = \frac{2V_{SV}^2 + V_{SH}^2}{3}\tag{2.73}$$

$$V_P^2 = \frac{C + 4A}{5\rho} = \frac{V_{PV}^2 + 4V_{PH}^2}{5},\tag{2.74}$$

such that the average isotropic S velocity depends only on V_{SV} and V_{SH}, and the P velocity only depends on V_{PV} and V_{PH}.

We also define the following anisotropic parameters:

$$\xi = \frac{N}{L} \tag{2.75}$$

$$\phi = \frac{C}{A} \tag{2.76}$$

and obtain the differentials,

$$\delta \ln V_S = \frac{2\delta L + \delta N}{4L + 2N} - \frac{1}{2}\delta \ln \rho \tag{2.77}$$

$$\delta \ln V_P = \frac{\delta C + 4\delta A}{2C + 8A} - \frac{1}{2}\delta \ln \rho \tag{2.78}$$

$$\delta \ln \xi = \delta \ln N - \delta \ln L \tag{2.79}$$

$$\delta \ln \phi = \delta \ln C - \delta \ln A \tag{2.80}$$

$$\delta \ln \eta = \delta \ln F - \frac{\delta A - 2\delta L}{A - 2L}. \tag{2.81}$$

The sensitivity kernels for the desired parameterization will be linear combinations of the kernels described in (2.48)-(2.52). For convenience, we will drop the subscripts pertaining to the spherical harmonic expansion coefficients, and describe the kernel conversion in more general terms. Since we are no longer assuming a spherical harmonic expansion, we will refer to the general kernel for a relative shift in a model parameter (i.e. K_A would be the kernel describing the frequency shift due to a relative perturbation, $\delta \ln A$). Because an equivalent model perturbation should produce the same shift in mode frequency for any parameterization, we substitute equations (2.77)-(2.81) into

$$K_A \delta \ln A + K_C \delta \ln C + K_L \delta \ln L + K_N \delta \ln N + K_F \delta \ln F + K_\rho^{(1)} \delta \ln \rho \tag{2.82}$$
$$= K_{V_S} \delta \ln V_S + K_{V_P} \delta \ln V_P + K_\xi \delta \ln \xi + K_\phi \delta \ln \phi + K_\eta \delta \ln \eta + K_\rho^{(2)} \delta \ln \rho$$

where $K_\rho^{(1)}$ refers to the density kernel for the parameterization as in *Li and Romanowicz,* [1996], and $K_\rho^{(2)}$ is the kernel for the new parameterization, which will be different due to the inclusion of density sensitivity inside the velocity terms. Solving for the new kernels, we get

$$K_{V_S} = 2(K_L + K_N - \frac{2L}{A - 2L}K_F) \tag{2.83}$$

$$K_{V_P} = 2(K_A + K_C + \frac{A}{A - 2L}K_F) \tag{2.84}$$

$$K_\xi = \frac{1}{2L + N}(2LK_N - NK_L + \frac{2LN}{A - 2L}K_F) \tag{2.85}$$

$$K_\phi = \frac{1}{C + 4A}(4AK_C - CK_A - \frac{AC}{A - 2L}K_F) \tag{2.86}$$

$$K_\eta = K_F \tag{2.87}$$

$$K_\rho^{(2)} = K_\rho^{(1)} + K_A + K_C + K_L + K_N + K_F \tag{2.88}$$

We now have the kernels necessary to use *NACT* waveform modelling to invert for radially anisotropic structure.

2.5 Other perturbations to the SNREI seismogram

In sections 2.2 and 2.3, we discussed the perturbations to the SNREI seismogram resulting from 3D perturbations of the elastic coefficients. Another important effect on the observed seismic waveforms is anelasticity. The Earth does not behave as a purely elastic medium. Energy in seismic oscillations of the Earth dissipates over time through such mechanisms as internal friction, and we see this as an exponential decay of the oscillations of the normal modes over time. If we model the Earth as a linear viscoelastic solid, we can use the correspondence principle [*Fung*, 1965] to perturb the real elastic moduli with a small complex value.

For example, we consider an isotropic, spherically symmetric model of anelasticity, which introduces a complex perturbation to the bulk and shear moduli, $\kappa(r)$ and $\mu(r)$,

$$\delta\kappa = i\frac{\kappa(r)}{Q_\kappa(r)} \tag{2.89}$$

$$\delta\mu = i\frac{\mu(r)}{Q_\mu(r)}, \tag{2.90}$$

where Q_κ and Q_μ are referred to as the bulk and shear quality factors.

If a mode $\mathbf{u}_j$ satisfies (2.13) and has time-dependence of the form $\exp(i\omega_j t)$, it must also satisfy the homogenous case ($\mathbf{f} = 0$), so

$$\mathcal{H}(\mathbf{u}_j) = -\omega_j^2 \rho \mathbf{u}_j. \tag{2.91}$$

Multiplying by $\mathbf{u}_j^*$ and integrating over the volume gives us

$$\int_V \mathbf{u}_j^* \mathcal{H}(\mathbf{u}_j)dV = -\omega_j^2 \int_V \rho\, \mathbf{u}_j^* \mathbf{u}_j dV. \tag{2.92}$$

If we now consider anelasticity, the perturbations (2.89) and (2.90) cause a perturbation to $\mathcal{H}$ and the mode $\mathbf{u}_j$, and (2.92) becomes

$$\int_V (\mathbf{u}_j^* + \delta\mathbf{u}_j^*)(\mathcal{H} + \delta\mathcal{H})(\mathbf{u}_j + \delta\mathbf{u}_j)dV = -(\omega_j + \delta\omega_j)^2 \int_V \rho\,(\mathbf{u}_j^* + \delta\mathbf{u}_j^*)(\mathbf{u}_j + \delta\mathbf{u}_j)dV. \tag{2.93}$$

To first order in small perturbations, this is

$$\int_V \mathbf{u}_j^* \mathcal{H}(\mathbf{u}_j)dV + \int_V \delta\mathbf{u}_j^* \mathcal{H}(\mathbf{u}_j)dV + \int_V \mathbf{u}_j^* \delta\mathcal{H}(\mathbf{u}_j)dV + \int_V \mathbf{u}_j^* \mathcal{H}(\delta\mathbf{u}_j)dV \tag{2.94}$$

$$= -\omega_j^2 \int_V \rho\, \mathbf{u}_j^* \mathbf{u}_j dV - \delta\omega_j^2 \int_V \rho\, \mathbf{u}_j^* \mathbf{u}_j dV - \omega_j^2 \int_V \rho\, \delta\mathbf{u}_j^* \mathbf{u}_j dV - \omega_j^2 \int_V \rho\, \mathbf{u}_j^* \delta\mathbf{u}_j dV,$$

where $\delta\omega_j^2 = 2\omega_j\delta\omega_j$.

The first terms on the right and left side of (2.94) cancel by (2.92), so

$$-\delta\omega_j^2 \int_V \rho\,\mathbf{u}_j^*\mathbf{u}_j dV = \int_V \mathbf{u}_j^*\delta\mathcal{H}(\mathbf{u}_j)dV \tag{2.95}$$
$$+ \int_V \delta\mathbf{u}_j^* \left[\mathcal{H}(\mathbf{u}_j) + \omega_j^2\rho\,\mathbf{u}_j\right] dV + \int_V \left[\mathbf{u}_j^*\mathcal{H}(\delta\mathbf{u}_j) + \omega_j^2\rho\,\mathbf{u}_j^*\delta\mathbf{u}_j\right] dV.$$

The bracketed portion of the second term on the right-hand side of (2.95) is zero by (2.91), and because $\mathcal{H}$ is a self-adjoint operator [*Dahlen and Tromp*, 1998],

$$\int_V \mathbf{u}_j^*\mathcal{H}(\delta\mathbf{u}_j)dV = \int_V \delta\mathbf{u}_j\mathcal{H}(\mathbf{u}_j^*)dV, \tag{2.96}$$

and the last term in (2.95) also disappears, leaving us with

$$-\delta\omega_j^2 \int_V \rho\,\mathbf{u}_j^*\mathbf{u}_j dV = \int_V \mathbf{u}_j^*\delta\mathcal{H}(\mathbf{u}_j)dV. \tag{2.97}$$

This can be evaluated by

$$\delta\omega_j^2 = \int_0^a \left[K_l\delta\kappa + M_l\delta\mu\right] r^2 dr, \tag{2.98}$$

where K_l and M_l are the kernels defined in *Woodhouse*, [1980], for the case $l = l'$ and $l'' = 0$. Note that this is equivalent to the frequency shift from (2.36), but due to the spherical symmetry of the perturbations, we only need to consider self-coupling, degree 0 terms. Because these are real kernels, and the perturbations are imaginary, the effect of anelasticity is to include an imaginary perturbation to the eigenfrequency, $\omega_j = \omega_j + i\alpha_j$, where α_j is a function of the radial structure of Q_κ and Q_μ and the radial sensitivity kernels of the mode. As expected, when this is substituted into the time dependence of the mode, $\mathbf{u}_j$, it leads to an exponential decaying oscillation of the form $\exp((i\omega_j - \alpha_j)t)$.

In the modelling of chapters 3 and 4, we use this approach to include a 1D attentuation model. Although the attenuation structure of the Earth unquestionably includes 3D heterogeneity, this correction is adequate for our work because the primary effect of Q structure is a perturbation to the amplitude of the seismogram, while the velocity modelling approach we use chiefly models the phase and not the amplitude of the seismogram [*Gung and Romanowicz,* 2004].

Another factor which can affect the amplitude of observed seismograms is the focussing and defocussing due to 3D velocity heterogeneity. Because the *NACT* approach developed in section 2.3 is only sensitive to structure along the great circle path between source and receiver, we do not model this focussing effect. If we extend the asymptotic approximations to second order in $1/l$, these effects can be considered using the derivatives of structure perpendicular to the great circle path [*Romanowicz,* 1987]. This, however, becomes a more expensive computation, and because we are chiefly interested in the phase of the seismogram for our velocity modelling, we also neglect this effect.

2.6 Finite difference waveform modelling

The normal mode-based approaches have many advantages when dealing with the inversion of a large global set of seismic waveforms. Though there are many approximations, we obtain analytic expressions for the partial derivatives of seismograms as a function of perturbations of model parameters. This enables us to use an iterative least-squares inversion approach [*Tarantola and Valette,* 1982] to improve our structural model.

However, for the application of waveform modelling in chapter 5, we wish to calculate waveforms on a regional scale using a model with much larger 3D variations. Although

the frequency range of interest (periods of 20 to 50 seconds) is similar, *NACT* seismograms are clearly not adequate for the task. Model perturbations are quite large for a perturbation theory approach, and the close distances and short wavelength structure both violate assumptions inherent in the approach. We do not, however, require the partial derivatives with respect to model parameters for the source studies in chapter 5, so a different numerical approach is acceptable.

We choose to use a finite-difference code (E3D) [*Larsen and Schulz*, 1995] to accurately synthesize seismic waveforms propagating through a complex regional velocity structure. A finite-difference approach utilizes a discrete sampling both spatially and temporally, and evaluates derivatives that arise from the equations of motion numerically by comparing neighboring grid points and time samples (e.g. *Moczo et al.*, [2000]).

For example, neglecting boundary tractions, we can express the equations governing motion using tensor notation as

$$\rho \frac{\partial^2}{\partial t^2} u_i = \tau_{ij,j} + f_i, \tag{2.99}$$

where, if we use a Cartesian coordinate system, u_i is the component of displacement in the x, y or z direction, $\tau_{ij,j}$ represents the derivative of the ijth component of the stress tensor with respect to j, and f_i is the ith component of the body force per unit volume.

Furthermore, we can define the components of the stress tensor using Hooke's law,

$$\tau_{ij} = c_{ijkl} e_{kl}, \tag{2.100}$$

where c_{ijkl} is the fourth-order stiffness tensor, and e_{kl} is the strain tensor, $e_{ij} \equiv \frac{1}{2}(u_{i,j} + u_{j,i})$. If the medium is purely elastic and isotropic, we can define the six

independent components of the stress tensor as functions of the Lamé moduli [*Aki and Richards*, 2002],

$$\tau_{xx} = (\lambda + 2\mu)\frac{\partial}{\partial x}u_x + \lambda\frac{\partial}{\partial y}u_y + \lambda\frac{\partial}{\partial z}u_z \tag{2.101}$$

$$\tau_{yy} = \lambda\frac{\partial}{\partial x}u_x + (\lambda + 2\mu)\frac{\partial}{\partial y}u_y + \lambda\frac{\partial}{\partial z}u_z \tag{2.102}$$

$$\tau_{zz} = \lambda\frac{\partial}{\partial x}u_x + \lambda\frac{\partial}{\partial y}u_y + (\lambda + 2\mu)\frac{\partial}{\partial z}u_z \tag{2.103}$$

$$\tau_{xy} = \mu(\frac{\partial}{\partial y}u_x + \frac{\partial}{\partial x}u_y) \tag{2.104}$$

$$\tau_{xz} = \mu(\frac{\partial}{\partial z}u_x + \frac{\partial}{\partial x}u_z) \tag{2.105}$$

$$\tau_{yz} = \mu(\frac{\partial}{\partial z}u_y + \frac{\partial}{\partial y}u_z), \tag{2.106}$$

where λ and μ describe the elastic properties of the material at each gridpoint.

If we specify an initial model with λ, μ, and ρ at each gridpoint, and assume initial quiescence, we have 9 quantities (the 3 components of displacement in (2.99) and the 6 independent elements of the stress tensor in (2.101)-(2.106)) that we can evaluate at each grid point and time step using finite differences to approximate the derivatives.

The particular approach we use [*Larsen and Schulz*, 1995] has a staggered grid, meaning that the elements of the stress tensor and the elastic constants are defined halfway between grid points where the displacement field is calculated. This is advantageous, as the elements of the stress tensor are determined by the spatial derivatives of the displacement, and likewise the displacement depends on the spatial derivatives of the stress tensor. The scheme is fourth order in space (meaning the spatial derivatives are evaluated by considering the values of the two nearest neighbors in each spatial direction, as well as the next closest two neighbors), and second-order in time. For a specific realization of this scheme, see the appendix of *Moczo et al.*, [2000].

This approach can give a very good approximation of the seismic wavefield if the solution is stable, and the grid sampling per seismic wavelength is sufficient to avoid numerical grid dispersion, which will artificially decrease the velocity for shorter wavelength seismic waves [*Moczo et al.*, 2000]. The solution will be stable provided the time step, Δt, meets the stability requirement,

$$\Delta t \leq \frac{6}{7\sqrt{3}} \frac{h}{v_{max}}, \tag{2.107}$$

where h is the grid spacing and v_{max} is the maximum velocity in the model. To avoid grid dispersion, we choose to sample approximately 10 grid points per minimum wavelength of interest, which is determined by the minimum velocity in the model divided by the maximum frequency of interest, although most seismological studies have shown that 5-6 grid points per wavelength is likely sufficient to avoid grid dispersion (e.g. [*Levander*, 1988; *Graves*, 1993; *Moczo et al.*, 2000]). Since the computational cost increases linearly with $(\Delta t)^{-1}$ and the number of grid points, the cost increases very rapidly as we increase the region of interest, increase the spatial resolution (halving the grid spacing leads to a factor of 8 increase in the number of grid points and thus computation time), or try to look at higher frequency data. For the regional long-period waveform problem in chapter 5, however, the approach is capable of accurately modelling the seismic wavefield in a very complex velocity model.

Chapter 3

Inferences on flow at the base of Earth's mantle based on seismic anisotropy

This chapter has been published in *Science* [*Panning and Romanowicz,* 2004a] under the title 'Inferences on flow at the base of the Earth's mantle based on seismic anisotropy,' and also includes supplementary online material published at the magazine's website (sections 3.3-3.7).

Summary

We apply global waveform tomography to model radial anisotropy in the whole mantle. We find that in the last few hundred kilometers near the core mantle boundary, horizontally polarized S wave velocities (V_{SH}) are, on average, faster ($\approx 1\%$) than vertically polarized S velocities (V_{SV}), suggesting a large scale predominance of horizontal shear. This confirms that the D″ region at the base of the mantle is also a

mechanical boundary layer for mantle convection. A notable exception to this average signature can be found at the base of the two broad low velocity regions under the Pacific Ocean and under Africa, often referred to as "superplumes", where the anisotropic pattern indicates the onset of vertical flow.

3.1 Introduction

The core-mantle boundary (CMB) represents a thermal and a chemical boundary between the solid silicate mantle and the liquid iron outer core. The corresponding boundary layer on the mantle side, often referred to as D″, is thus the site of complex dynamic processes that may involve thermal and chemical heterogeneity at various scales [*Lay et el.,* 1998a]. Additionally, it has been suggested that this layer functions as a mechanical boundary layer for the convection of the overlying mantle, leading to intense deformation. Such deformation processes can lead to detectable seismic anisotropy, either through the alignment of anisotropic crystals in the strain field or through the fine layering of materials with contrasting elastic properties [*Karato,* 1998a; *Kendall and Silver,* 1996].

The presence of anisotropy in D″ has been established in several regions, including under the central Pacific ocean, northeastern Asia, Alaska and central America, from the observation of seismic waves diffracting (Sdiff) or reflecting (ScS) at the core mantle boundary [*Kendall and Silver,* 1996; *Vinnik et al.,* 1989; *Lay et el.,* 1998b; *Russell et al.,* 1999; *Thomas and Kendall,* 2002; *Fouch et al.,* 2001]. The limited areas of sampling, however, have made interpretation of these observations difficult. A more global picture of long-wavelength anisotropic D″ structure would clearly aid interpretation both in terms of dynamic flow modeling as well as mineral physics.

With this in mind, we have adapted a global waveform tomography approach [*Li*

and Romanowicz, 1995; *Mégnin and Romanowicz,* 2000] to develop a 3D model of radial anisotropy in the whole mantle using a large dataset of three-component time-domain waveforms of both surface and body waves (dataset described in more detail in sec. 3.3). The model is parameterized in terms of isotropic V_S and the anisotropic ξ parameter ($\xi = V_{SH}^2/V_{SV}^2$), which is directly related to radial anisotropy in S-wave velocity (see sec. 4.2.1). With our dataset, and our broadband sensitivity kernels [*Li and Romanowicz,* 1995] which allow us to utilize both reflected and diffracted waves in D″ (Fig. 3.1), we have enough coverage to invert for radially anisotropic structure in the whole mantle, as shown by resolution tests (see sec. 3.5).

3.2   Results and Discussion

Our final model includes anisotropic S-wave velocity structure throughout the mantle. Two regions of strong "degree zero" radial anisotropy stand out in our model: the uppermost mantle and D″ (Fig. 3.2). In both regions, on average, V_{SH} is faster than V_{SV}. This can be interpreted, at least for the upper mantle, as indicating the presence of strong horizontal shear, consistent with previous work [*Montagner and Tanimoto,* 1991; *Ekström and Dziewonski,* 1998; *Gung et al.,* 2003; *Dziewonski and Anderson,* 1981]. The isotropic part of the model (Fig. 3.3, A and B) is consistent with earlier tomographic models of shear velocity in this depth range [*Mégnin and Romanowicz,* 2000; *Masters et al.,* 1996; *Gu et al.,* 2001], and is characterized by a strong degree 2 component representing a fast ring surrounding two low velocity features (often called superplumes) centered beneath the central Pacific ocean and Africa. The strong degree 0 component in ξ ($\delta \ln(\xi) > 0$) dominates the map in D″ (Fig. 3.3, C and D). The regions that differ most strongly from this average structure correlate well with the locations of the two superplumes, with reduced values of $\delta \ln(\xi)$ under the central Pacific ocean, Africa, and the south Atlantic ocean, including patches with negative

values ($V_{SV} > V_{SH}$). Another two large patches of reduced $\delta\ln(\xi)$ are seen just west of North America and under central Eurasia. These patches also are related to slow isotropic velocities, although these regions of depressed velocities are much smaller than the two superplumes.

Although the finer-scale features of our model may not be significant and observations in regions with high gradients will display some differences due to the long-wavelength parameterization of our model, the long-wavelength anisotropic features imaged in our model generally agree with more localized studies of D″ anisotropy (Fig. 3.3C). Specifically, earlier studies imaged areas with positive $\delta\ln(\xi)$ beneath Central America and Alaska [*Lay et el.,* 1998b; *Fouch et al.,* 2001], as well as northeastern Asia [*Thomas and Kendall,* 2002]. The central Pacific regional results are more variable with some areas showing negative $\delta\ln(\xi)$ [*Kendall and Silver,* 1996; *Lay et el.,* 1998b; *Fouch et al.,* 2001].

The dominant $V_{SH} > V_{SV}$ found as one approaches the CMB suggests that the anisotropy observed in D″ is related to the dominant horizontal flow in a mechanical boundary layer, analogous to the larger signal observed in the uppermost 200 km of the mantle and factored into the construction of the Preliminary Reference Earth Model (PREM) [*Dziewonski and Anderson,* 1981]. As one approaches regions of upwelling, the direction of flow changes and results in a different signature of anisotropy, as manifested in our study under the central Pacific and Africa. Anisotropy in these regions bordering the large scale upwellings may be much more complex and include tilting of the axis of symmetry, which we assume to be vertical in our modeling. This would result in azimuthal anisotropy, which we do not attempt to model here.

Whether the globally observed anisotropy is due to lattice-preferred orientation (LPO) [*Karato,* 1998a; *McNamara et al.,* 2002] or the alignment of materials with differing elastic properties through shape-preferred orientation (SPO) [*Kendall and Silver,* 1996] must await direct measurements of how lowermost mantle materials will develop LPO anisotropy at the corresponding temperature and pressure conditions. Using

theoretical methods, arguments for weak anisotropy in perovskite $((Mg, Fe)SiO_3)$ and strong positive ξ in periclase (MgO) [*Karato,* 1998a] as well as for negative ξ in both perovskite and periclase [*Stixrude,* 1998] have been advanced. Some studies have shown that high strain in subducting slabs approaching the core-mantle boundary might be able to sustain conditions necessary for producing LPO structure across broad regions of D″ [*McNamara et al.,* 2002]. This model also shows that while the major axes of the strain ellipses are horizontal under the downgoing slabs, the material can be rotated to vertical as it approaches upwellings, possibly explaining the observed change in anisotropy below the superplumes in our model. Different SPO hypotheses have been advanced as well, mostly relating to horizontal layering or inclusion of various shaped pockets of contrasting material. Candidates for the differing elastic properties include reaction products from core-mantle interaction [*Knittle and Jeanloz,* 1991], and melted former basalt in a slab graveyard [*Kendall and Silver,* 1996; *Lay et el.,* 1998b]. In general, these SPO models lead to positive ξ, although if there is tilting of the pockets of differing material under deformation, considerable azimuthal variation in velocities could be observed [*Karato,* 1998a].

Whatever the cause, our results clearly show that the dynamics of D″ correspond with what would be expected in a boundary layer dominated by horizontal flow, and emphasize the unique character of the two superplume regions, for which we bring additional evidence of large scale upwelling. While measurements of deformation at the pressures and temperatures corresponding to the CMB region are not yet available, our results suggest that similar relationships between anisotropic signature and flow prevail in the uppermost and lowermost mantle.

3.3 Dataset and Sensitivity Kernels

Non-linear asymptotic coupling theory [*Li and Romanowicz,* 1995], allows us to compute sensitivity kernels for both diffracted and reflected phases at the core-mantle boundary (Fig. 3.1). Both sets of kernels shown are for phases recorded on the transverse component. The sensitivity of the mostly horizontally traveling Sdiff is predominantly V_{SH}, while the vertically traveling ScS is primarily sensitive to V_{SV} structure.

The dataset for this modelling consists of wavepackets of coherent energy selected in the time-domain. There were 32,217 wavepackets with body wave energy (642,837 data points at a minimum period of 32 seconds), and 83,398 surface wave packets (4,000,194 data points at a minimum period of 60 seconds). Wavepackets were selected from broadband IRIS Global Seismic Network [*Smith,* 1986] and GEOSCOPE network [*Romanowicz et al.,* 1984] data using an automated selection algorithm (see Appendix A) and subsequently checked by hand. Wavepackets were defined based on standard travel-time curves, and the algorithm compared data with PREM synthetics for a number of criteria, including maximum amplitude, correlation, and root-mean-squared difference between observed and synthetics. Because we are using a perturbation-based approach, such selection criteria are necessary to avoid traces strongly influenced by unmodeled source effects and/or near-receiver structure.

3.4 Scaling Relations

The scaling relations discussed in the Notes section of the main text were derived from laboratory data for upper mantle materials and pressure/temperature conditions. Because we are applying these relations to the whole mantle to limit the model

parameters in our inversion, including the lower mantle where we have no laboratory data, it is important to know what effect this has on the final model. In order to assess this, we performed a lower degree inversion (degree 8), where we allowed all three anisotropic parameters (ξ, ϕ, and η) to vary independently. V_P and ρ were still assumed to scale with V_S, leaving 4 parameters in the inversion rather than 2. Figure 3.4 shows the correlation for $\delta \ln \xi$ between the 4 parameter inversion and the 2 parameter inversion. For the bulk of the mantle, the correlation is greater than 0.8, indicating that the scaling assumption has little effect on the patterns obtained for ξ structure. The correlation computed across spherical harmonic coeficients is somewhat lower for depths less than 100 km, as well as for the depth range roughly between 600 and 700 km, indicating that there might be some tradeoffs in these depth ranges that should be considered in future modeling. Examination of the resolution matrix indicated that ξ was the best-resolved of the three anisotropic parameters, and off-diagonal elements were small.

3.5   Resolution Tests

For resolution matrix tests for the two-parameter inversion, we first used a random input model with equal strength in degrees 0 through 16. We compared the output model from the resolution matrix testing with the input model in terms of RMS amplitude variation and correlation as a function of degree (Fig. 3.5). The correlation between input and output models showed very little variation as function of damping, but the amplitude ratios varied more strongly as a function of damping. In particular, the decreasing amplitude with increasing spherical harmonic degree (decreasing structural wavelength) was very sensitive to the magnitude of horizontal smoothing used. The smoothing in the final model was chosen so that RMS amplitudes for wavelengths with lower correlation between input and output models were kept below 50%

Num.	Denom.	All data	Surface waves	Body waves	D″ sensitive
A	B	1.0447 (99%)	1.0615 (99%)	1.0202 (99%)	1.0085 (90%)
A	C	1.0464 (99%)	1.0615 (99%)	1.0243 (99%)	1.0183 (99%)
A	D	1.0526 (99%)	1.0655 (99%)	1.0334 (99%)	1.0227 (99%)
A	E	1.0604 (99%)	1.0697 (99%)	1.0464 (99%)	1.0345 (99%)
B	C	1.0017 (75%)	1.0000 (n/a)	1.0040 (75%)	1.0098 (95%)
B	D	1.0075 (99%)	1.0038 (90%)	1.0129 (99%)	1.0141 (99%)
B	E	1.0150 (99%)	1.0077 (99%)	1.0257 (99%)	1.0258 (99%)
C	D	1.0058 (99%)	1.0038 (90%)	1.0088 (95%)	1.0043 (75%)
C	E	1.0133 (99%)	1.0077 (99%)	1.0216 (99%)	1.0159 (99%)
D	E	1.0074 (99%)	1.0039 (90%)	1.0126 (99%)	1.0116 (95%)

Table 3.1: Table of F values and significance (in parentheses) for comparison of models with varying depth ranges of anisotropy. F ratios are formed by taking the estimated data variance of the numerator model (Num. column) and dividing it by the variance estimated by the denominator model (Denom. column). A value of 1.0 indicates no improvement in fit, while values greater than 1.0 indicate better fit by the denominator model. Significance is determined by comparing to a set of critical values determined by the degrees of freedom of the two models [*Menke,* 1989]. Model A contains no anisotropic perturbations from PREM. Model B allows anisotropic structure above 300 km depth. Model C allows anisotropic structure above 300 km depth and in D″ (lowermost 500 km of the mantle). Model D adds in all anisotropic structure above 1000 km depth, and Model E is the full anisotropic model. F ratios are calculated separately for the fit to the full dataset, surface waves, body waves, and the subset of body wavepackets with sensitivity in D″. See text for explanation.

of the input amplitude, to minimize the amount of spurious structure obtained. We also chose to limit our inversion for ξ to degree 8 because the tests showed we were unable to resolve structure at shorter wavelengths for the bulk of the mantle. In order to look at the geographical dependence of the model resolution, we performed a "checkerboard" test where the input model is a degree 6 spherical harmonic pattern (Fig. 3.6). The recovered model indicates we are able to obtain the correct pattern in most of the D″ region with slightly reduced amplitude, with the best resolution in the northeast Pacific ocean, although the resolution is not as good in portions of the southern hemisphere.

3.6 Statistical Significance

We also performed tests to determine the statistical significance of the improvement in fit to the data for the model with anisotropic structure in D″, as compared to a model obtained using an isotropic parameterization.

In general, models with more parameters will always show an improvement in fit, but we can assess the statistical significance of this improvement using an F-test [*Menke,* 1989]. To estimate the number of independent data points, we resampled the waveforms to two points per minimum wavelength in the passband (16 s sampling interval for body waves, and 30 s for surface waves), which minimizes correlation due to the bandpassing of the data. Additionally, we accounted for redundancy of paths using the redundancy index g_{ij} [*Li and Romanowicz,* 1996], which assigns a weighting factor for wavepackets with similar phases and source-receiver paths. The degrees of freedom for each model is then determined by the difference between the estimated number of independent data points minus the number of model parameters. Using the values thus obtained for the degrees of freedom of the models, we compared several models, with or without anisotropy in different depth ranges (Table 3.5). Model B only allows anisotropic structure in the uppermost 300 km (a region with well-established radial anisotropy), while Model C also allows anisotropic structure in the lowermost 500 km of the mantle. Significance values shown in Table 3.5 are then determined by comparing to critical F values for which we can reject the hypothesis that the variance estimates of the two models are equivalent at a certain probability or p-value. For example, when we say the value is significant at the 95% confidence level, this means that the F value is greater than the critical value for which there is a 5% chance that the two variance estimates are equivalent (a p-value of 0.05). Although the F value comparing these two models for the whole dataset is only significant at the 75% confidence level (with a p-value of 0.23), this is mainly due to the fact that the majority of the dataset has no sensitivity to the D″ region. Most important here is the fact that adding anisotropy in D″ is significant at the 95% confidence (p-value

of 0.047) for the subset of body wave data sensitive to D″, which make up only 16% of the whole dataset.

On the other hand, surface waves, which make up 72.7% of the independent data points in our dataset, have no sensitivity to D″, and see most of their improvement in fit from the strong anisotropic model in the uppermost 300 km (comparison of models A and B).

We also performed bootstrap and jackknife estimations of the standard error of the final model [*Efron and Tibishirani,* 1993]. For the jackknife test, we divided the dataset into 12 subsets and inverted all combinations of 10 of these subsets to obtain 66 different estimations of the model, and then used the jackknife standard error formula to obtain an estimate of the error map for our full inversion (Fig. 3.7). The bootstrap estimation is a similar approach, but in this case we generate many "bootstrap samples" of the dataset by assuming each of the 12 subsets has equal probability of observation. Then we generated, in this case, 300 samples of the dataset by randomly selecting 12 subsets with replacement from the original 12 subsets (i.e. one possible sample would be $[S_1, S_2, ..., S_{12}]$, while another would be $[S_1, S_1, ..., S_1]$). These 300 samples were inverted for models, and then we used the bootstrap standard error formula to generate an error map. The bootstrap error map is nearly identical to the jackknife map (correlation greater than 0.99), but the amplitude of errors estimated is greater by a factor of approximately 3. This is likely an overestimate of the error, as we used the data weighting calculated for the whole dataset for each bootstrap sample, which includes weighting for redundancies of similar source-receiver paths which would be incorrect for many bootstrap samples. Regardless, the bootstrap error map can be viewed as an upper bound estimate, while the jackknife is likely a lower bound on the error, as the inverted datasets in this approach are quite similar to the final dataset.

3.7   Depth Distribution of ξ Structure in D$''$

Resolution tests indicate that there may be some smearing of structure down to the CMB from overlying signal (Fig. 3.8). This could cause some doubt about the degree 0 profile shown in Figure 3.2, which increases monotonically from about 2600 km depth to the CMB. To test whether the data required this structure, we performed an inversion where the bottommost spline of the ξ model was constrained to zero, effectively forcing the structure to go to pure isotropy at the CMB. The degree zero profile for the lowermost mantle in this model is shown in Figure 3.9. When comparing the full model to the constrained model, the improvement in fit was not significant at the 75% confidence level. Comparison of these models implies that the data require the large degree zero signature in D$''$, but we cannot determine whether the amplitude of structure is peaked at the CMB or slightly higher up within D$''$.
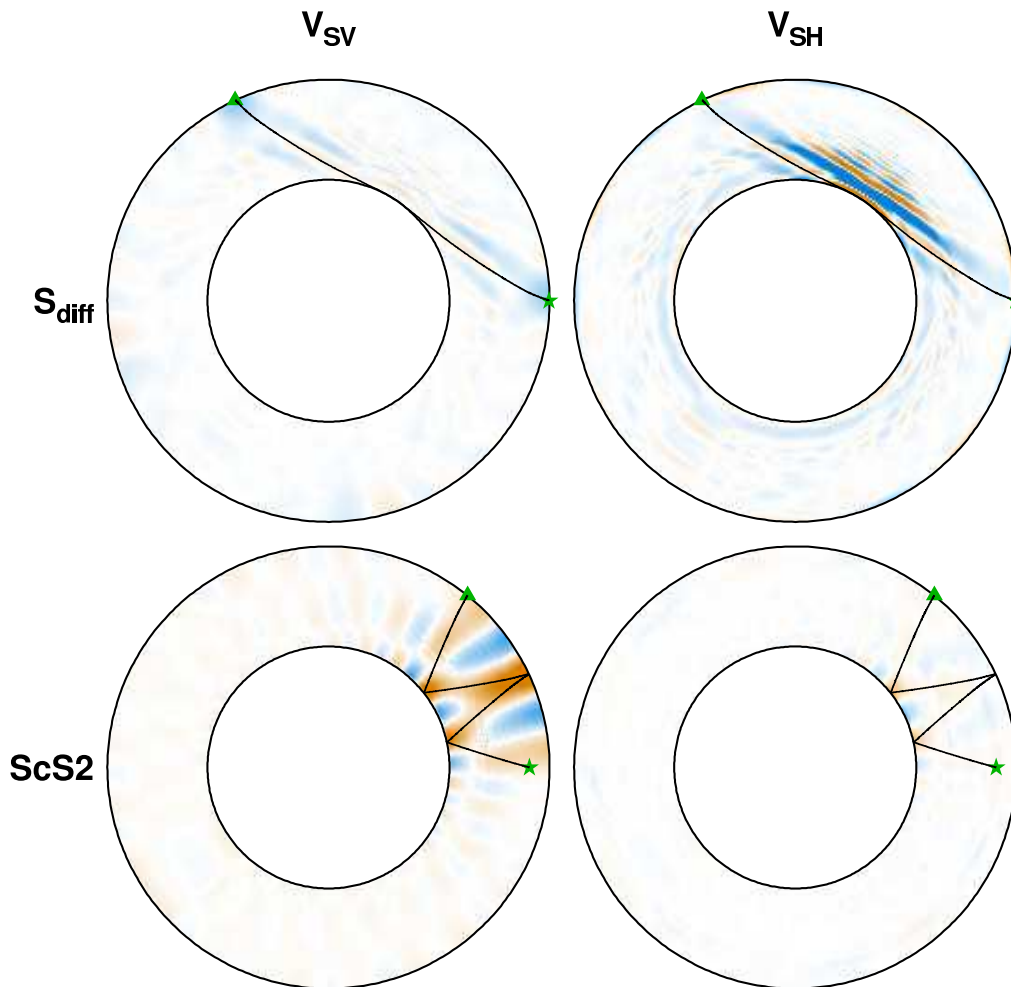
Figure 3.1: NACT sensitivity kernels for an S phase diffracted at the CMB (top row) and multiply-reflected (bottom row) for V_{SV} (left column) and V_{SH} (right column). All kernels are calculated for waveforms recorded on the transverse component. The slight sensitivity far away from the ray theoretical ray path is due to the truncation in the normal mode coupling summation. Note that ScS2 is primarily sensitive to V_{SV}, whereas Sdiff is primarily sensitive to V_{SH}. Combining both types of data (as well as other phases) allows us to investigate radial anisotropy.
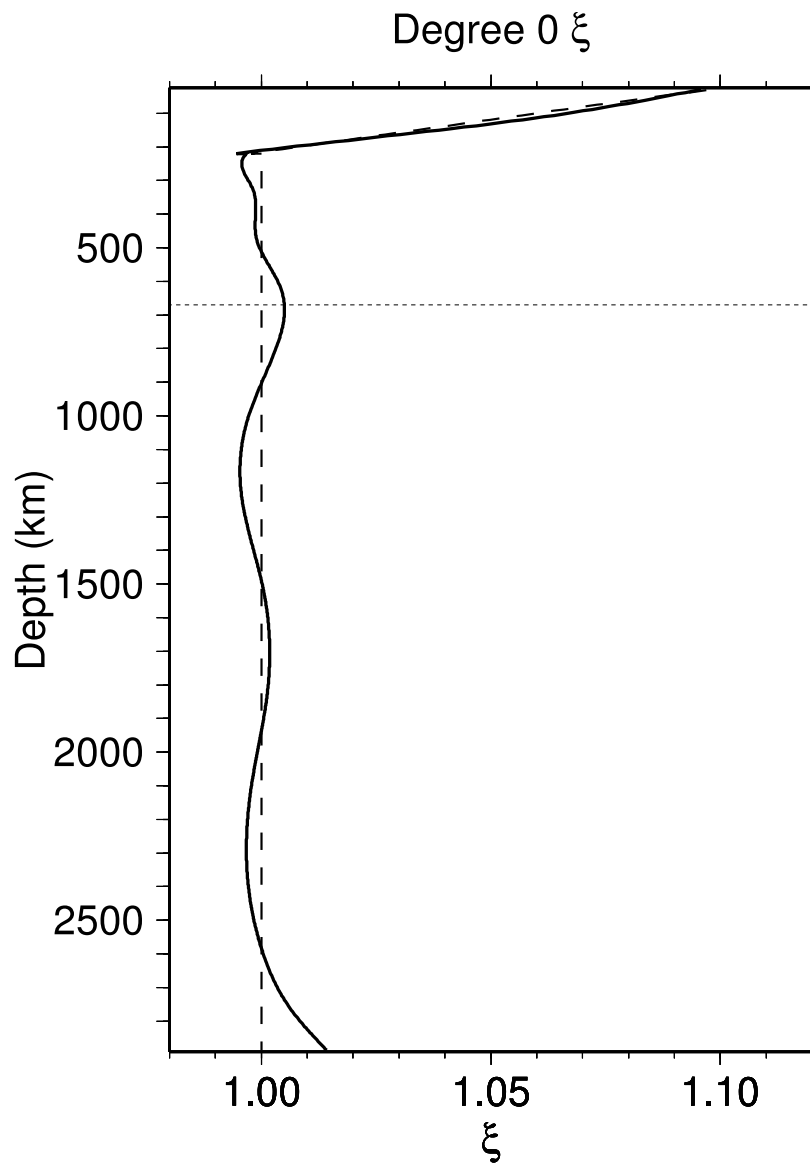
Figure 3.2: Degree 0 model for ξ as a function of depth. The values for PREM [*Dziewonski and Anderson,* 1981] are shown by the dotted line. Note the strong increase at the base of the mantle, similar but smaller in amplitude to that seen in the uppermost mantle. Significance of other oscillations is discussed in Chapter 4.
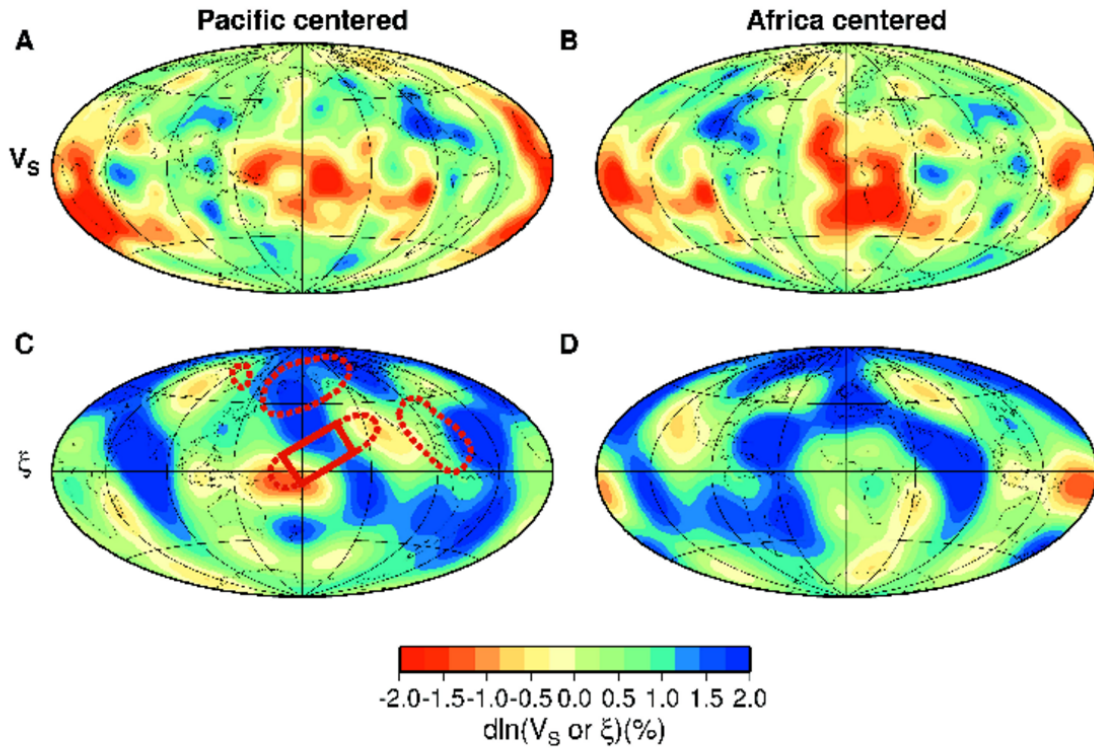
Figure 3.3: Distribution of $\delta \ln V_S$ (A and B) and $\delta \ln \xi$ (C and D) at a depth of 2800 km. Maps are shown centered under the Pacific (A and C) and Africa (B and D). Also shown in C are the regions of D'' sampled by previous regional studies. Dotted areas indicate observations of $V_{SH} > V_{SV}$, while the box in the central Pacific denotes a region with highly variable observations including $V_{SV} > V_{SH}$ (adapted from [*Lay et el.,* 1998b]). The shift of the zone of $\delta \ln \xi > 0$ to the east of central America in our model may be a result of the long-wavelength parameterization in our model. However, recent studies have documented that D'' in central America is the site of strong lateral gradients of structure [*Wysession et al.,* 2001], so this transition may be real.
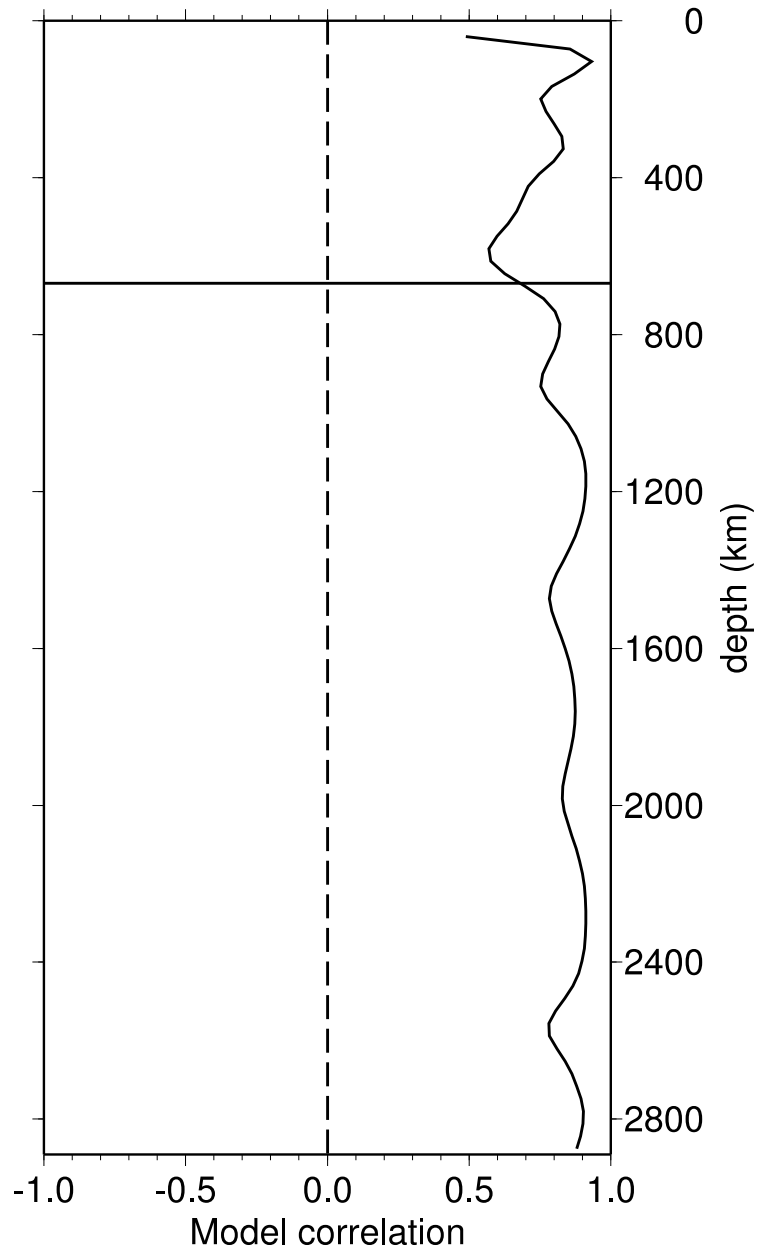
Figure 3.4: Correlation of the ξ models for the (V_S,ξ) and (V_S,ξ,ϕ,η) inversions as a function of depth. Correlation is close to 0.8 or better throughout most of the mantle with the exception of the uppermost 100 km and the interval between 600 and 700 km depth.
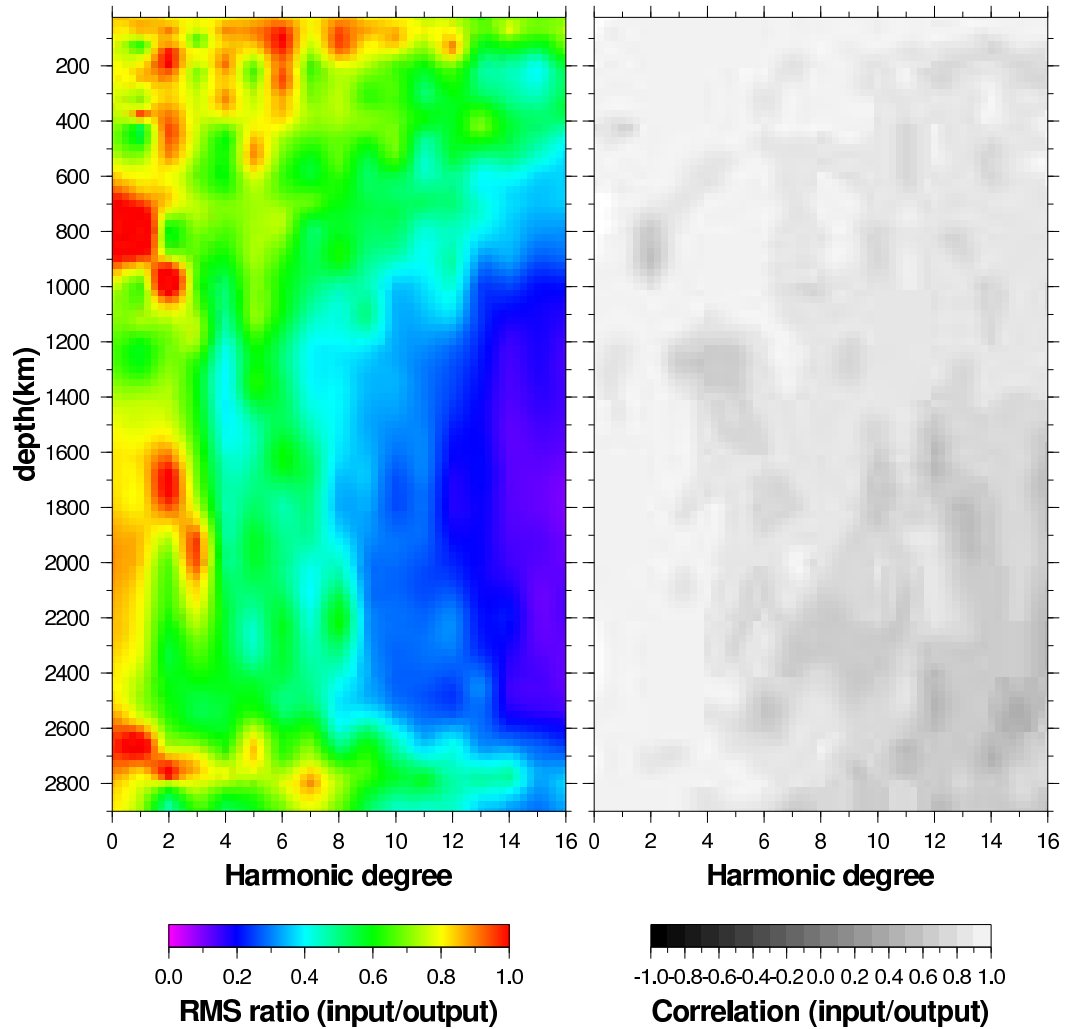
Figure 3.5: Comparison of input and output models for a resolution matrix test using the damping scheme of the real data inversion and a random input model with equal signal strength for spherical harmonic degrees 0 through 16. The RMS amplitude ratio of the output model to the input model (left) and the correlation of the two models (right) is shown as function of depth and the spherical harmonic degree of the structure.

A

Input -0.5/0.5 %

B

Output -0.5/0.4 %

0

dln(ξ)(%)
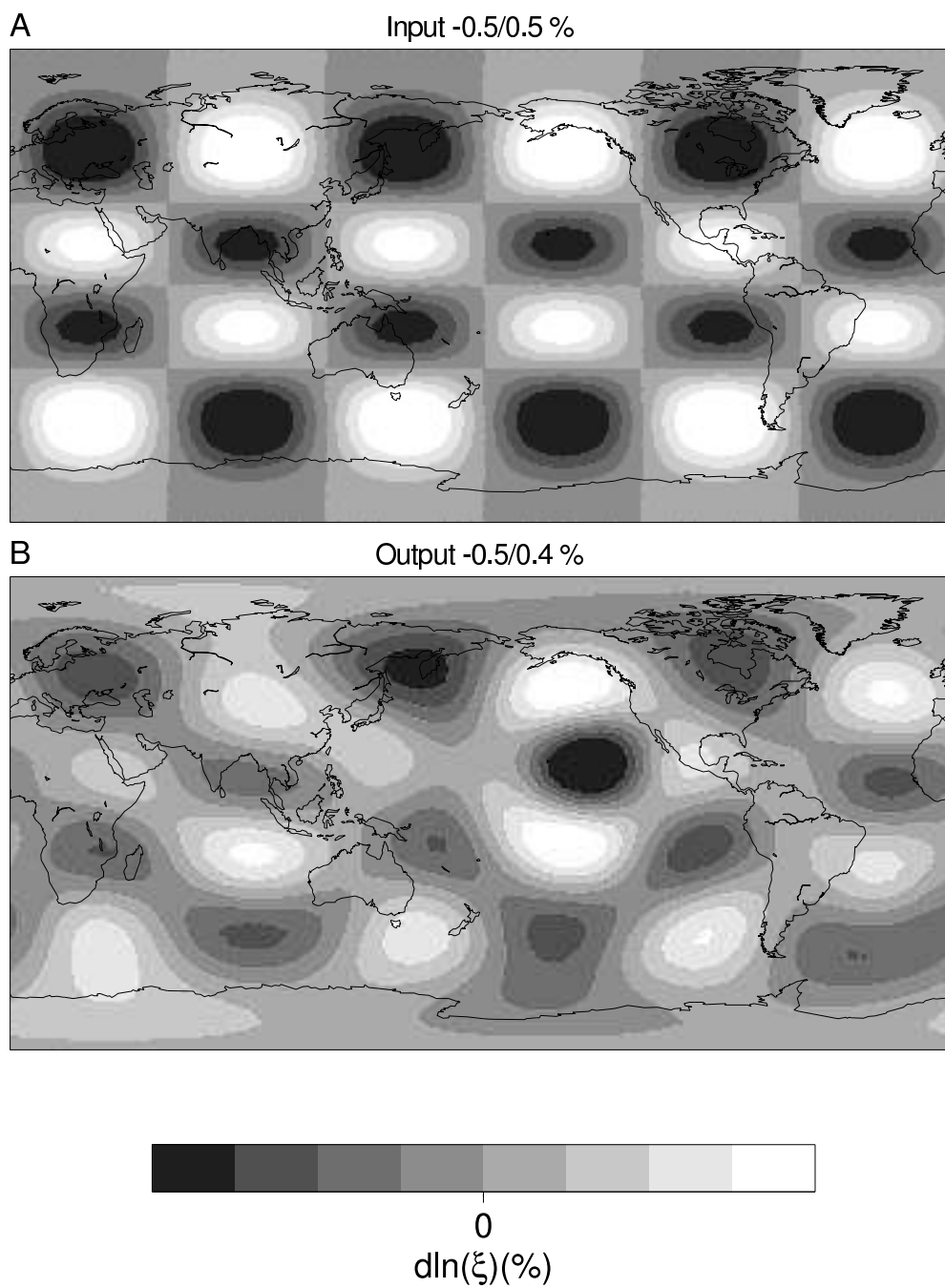
Figure 3.6: Degree 6 checkerboard resolution test. Input (A) and output (B) models using the resolution matrix calculated for the final inversion scheme.
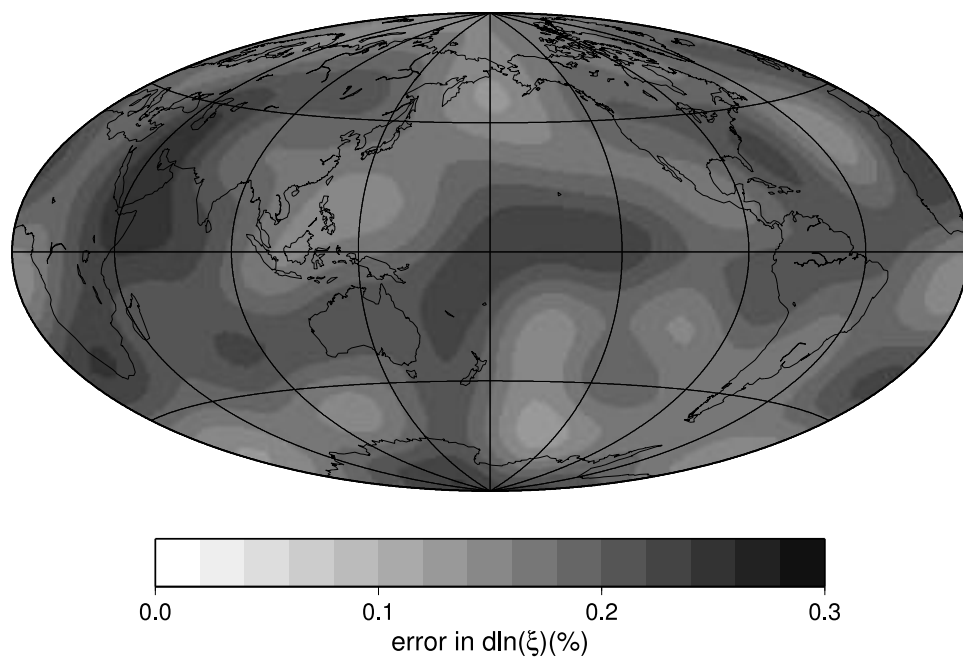
Figure 3.7: Jackknife error map at 2800 km depth. Units are dimensionless perturbation relative to the reference model, the same as in maps of ξ structure.
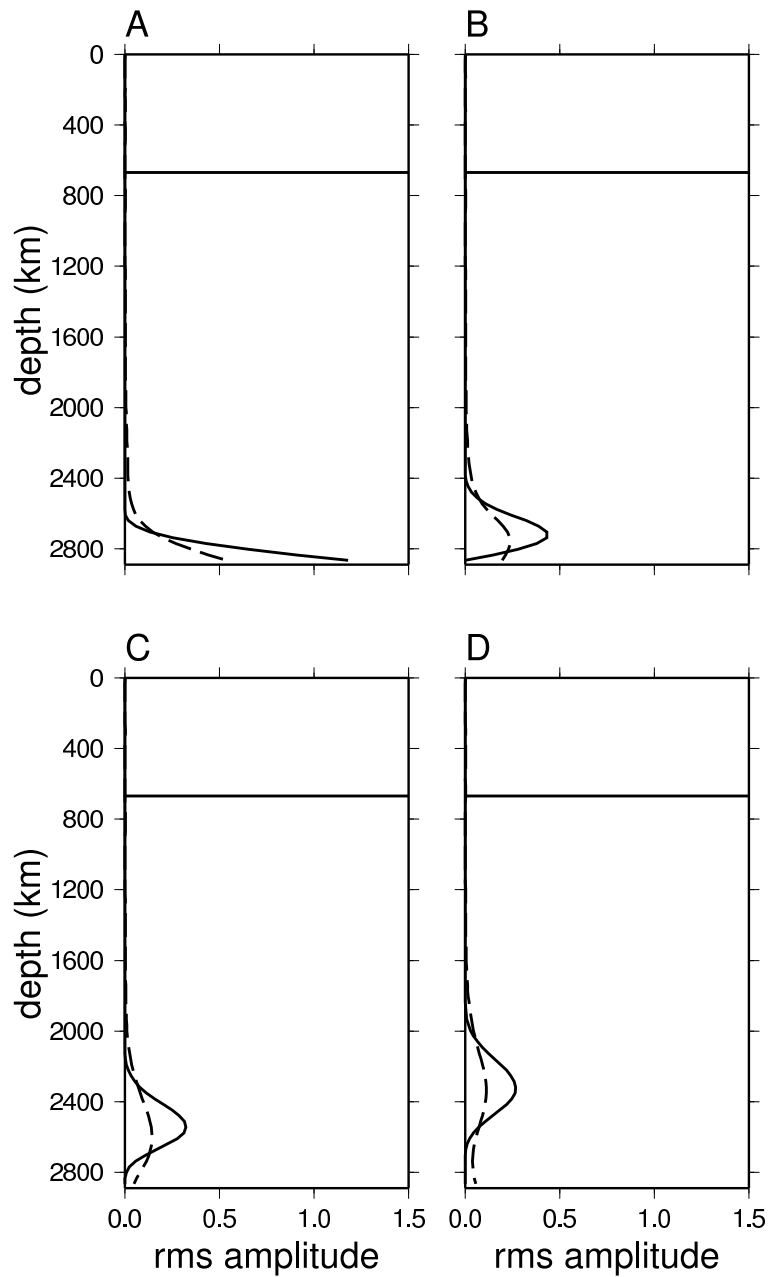
Figure 3.8: Depth resolution figure comparing input model (solid) and output model (dashed) for a resolution matrix test with input splines centered at depths of 2891 km (A), 2771 km (B), 2596 km (C), and 2371 km (D). There is some smearing with depth as well as a reduction in amplitude, although this reduction is less pronounced near the CMB.
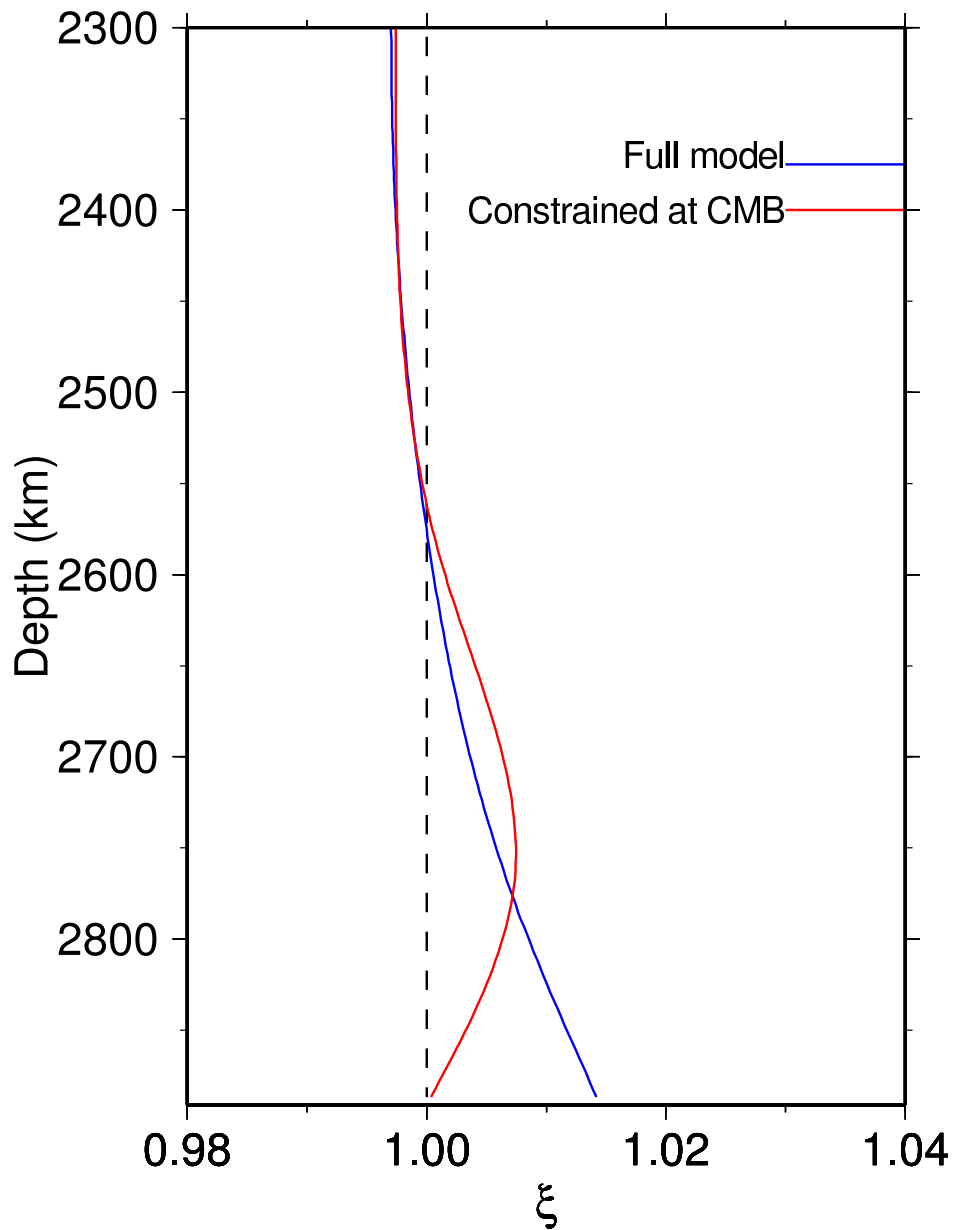
Figure 3.9: Comparison of the degree 0 signal in the full model (solid) and the model constrained to zero at the core-mantle boundary (dashed) in the lowermost 600 km of the mantle. While the strongest signal in the constrained model is at about 2750 km depth, the strong, positive degree 0 signature is still contained in the lowermost 300 km of the model.

Chapter 4

A three dimensional radially anisotropic model of shear velocity in the whole mantle

This chapter will be submitted for publication in *Geophysical Journal International* [*Panning and Romanowicz*, 2004b] under the title 'A three dimensional radially anisotropic model of shear velocity in the whole mantle.'

Summary

We present a degree 16 3D radially anisotropic model (SAW16B16-AN) of the whole mantle obtained using a large three component surface and body waveform dataset and an iterative inversion for structure and source parameters based on Nonlinear Asymptotic Coupling Theory (NACT) [*Li and Romanowicz*, 1995]. The model shows

a link between mantle flow and anisotropy in a variety of depth ranges. In the uppermost mantle, we confirm observations of regions with $V_{SH} > V_{SV}$ starting at $\sim$80 km under oceanic regions and $\sim$250 km under old continental lithosphere, suggesting horizontal flow beneath the lithosphere [*Gung et al.,* 2003]. We also observe a $V_{SV} > V_{SH}$ signature at $\sim$200-300 km depth beneath major ridge systems with amplitude correlated with spreading rate. In the transition zone (400-700 km depth), regions of subducted slab material are associated with $V_{SV} > V_{SH}$, while the ridge signal decreases except under the East Pacific Rise. While the mid-mantle has lower amplitude anisotropy ($<$1%), we also confirm the observation of strong radially symmetric $V_{SH} > V_{SV}$ in the lowermost 300 km [*Panning and Romanowicz,* 2004a]. The 3D deviations from this degree 0 signature are associated with the transition to the large-scale low-velocity superplumes under the central Pacific and Africa, suggesting that $V_{SH} > V_{SV}$ is generated in the predominant horizontal flow of a mechanical boundary layer, with a change in signature related to transition to upwelling at the superplumes. We also solve for source perturbations in an interative procedure. Source perturbations are generally small compared to published Harvard CMT solutions, but improve the fit to the data. The sources in the circum-Pacific subduction zones show small but systematic shifts in location.

4.1   Introduction

The 3D seismic velocity structure of the Earth's mantle represents a snapshot of its current thermal and chemical state. As tomographic models of the isotropic seismic velocity converge in their main features [*Masters et al.,* 2000; *Gu et al.,* 2001; *Grand,* 1997; *Mégnin and Romanowicz,* 2000; *Ritsema and van Heijst,* 2000], geodynamicists use them to infer the density structure, and thus the buoyancy contrasts which drive mantle convection [*Hager,* 1984; *Ricard and Vigny,* 1989; *Woodward et al.,* 1993;

Daradich et al., 2003]. This process, however, is complicated by the difficulty of separating thermal and chemical contrasts, and the lack of direct sensitivity of seismic velocities to the density contrasts which drive the convection.

In many regions of the mantle, analyzing the anisotropy of seismic velocities can give us another type of constraint on mantle dynamics. Nearly all the constituent minerals of the mantle have strongly anisotropic elastic properties on the microscopic scale. Random orientations of these crystals, though, tend to cancel out this anisotropy on the macroscopic scale observable by seismic waves. In general, to produce observable seismic anisotropy, deformation processes need to either align the individual crystals (lattice preferred orientation or LPO) (e.g. *Karato*, [1998a]), or cause alignment of pockets or layers of materials with strongly contrasting elastic properties (shape preferred orientation or SPO) [*Kendall and Silver,* 1996]. While in the relatively cold regions of the lithosphere these anisotropic signatures can remain frozen in over geologic time-scales [*Silver,* 1996], observed anisotropy at greater depths likely requires dynamic support [*Vinnik et al.,* 1992]. Thus, the anisotropy observed at sublithospheric depths is most likely a function of the current mantle strain field, and these observations, coupled with mineral physics observations and predictions of the relationship between strain and anisotropy of mantle materials at the proper pressure and temperature conditions, can help us map out mantle flow.

Some of the earliest work on large-scale patterns of anisotropy focussed on the uppermost mantle. Studies showed significant P velocity anisotropy from body wave refraction studies [*Hess,* 1964], as well as S anisotropy from incompatibility between Love and Rayleigh wave dispersion characteristics (e.g. *McEvilly*, [1964]). These observations were supported and extended globally by the inclusion of 1D radial anisotropic structure in the uppermost 220 km of the global reference model PREM [*Dziewonski and Anderson,* 1981], based on normal mode observations. More recently, much upper mantle work has focussed on the observation of shear-wave splitting, particularly as observed in SKS phases. This approach allows for the detection and modelling of azimuthal anisotropy on fine lateral scales, but there is little depth resolution and there

are tradeoffs between the strength of anisotropy and the thickness of the anisotropic layer. These tradeoffs make it very difficult, for example, to distinguish between models with anisotropy frozen in the lithosphere [*Silver,* 1996] or dynamically generated in the deforming mantle at greater depths [*Vinnik et al.,* 1992]. Shear-wave splitting analysis has also been applied to a variety of phases to look at anisotropy to deeper depths in subduction zones [*Fouch and Fischer,* 1996]. Many other studies have observed anisotropy in several geographic regions in the lowermost mantle using phases such as ScS and S$_{\text{diff}}$ (e.g. [*Lay and Helmberger,* 1983; *Kendall and Silver,* 1996; *Matzel et al.,* 1997; *Garnero and Lay,* 1997; *Pulliam and Sen,* 1998; *Lay et el.,* 1998b; *Russell et al.,* 1999]). With observations of anisotropy in many geographical regions and at a variety of depths in the mantle, a global picture of the 3D variation of anisotropy, such as that obtained by tomographic approaches, is desirable.

There has been increasing refinement of global 3D tomographic models of both P and S velocity over the last ten years, using a variety of datasets, including absolute travel times, relative travel times measured by cross-correlation, surface wave phase velocities, free oscillations, and complete body and surface waveforms. While most of these models assume isotropic velocities, a few global anisotropic models have also been developed. Best resolved is upper mantle radial and azimuthal anisotropy using fundamental mode surface waves [*Tanimoto and Anderson,* 1985; *Nataf et al.,* 1986; *Montagner and Tanimoto,* 1991; *Ekström and Dziewonski,* 1998; *Beghein and Trampert,* 2004] and more recently with the inclusion of overtones [*Gung et al.,* 2003] as well as some recent attempts at tomographically mapping transition zone radial [*Beghein and Trampert,* 2003] and azimuthal [*Trampert and van Heijst,* 2002] S anisotropy, radial S anisotropy in D″ [*Panning and Romanowicz,* 2004a] and finally P velocity anisotropy in the whole mantle [*Boschi and Dziewonski,* 2000].

In our earlier work, we have developed a complete waveform inversion technique which we used to focus on anisotropic structure in the upper mantle [*Gung et al.,* 2003] and the core-mantle boundary region [*Panning and Romanowicz,* 2004a]. Here we extend this modelling approach in order to map anisotropy throughout the mantle,

and explore the uncertainties and implications of the model.

4.2 Modelling approach

4.2.1 Parameterization

While an isotropic elastic model requires only two independent elastic moduli (e.g. the bulk and shear moduli), a general anisotropic elastic medium is defined by 21 independent elements of the fourth-order elastic stiffness tensor. Attempting to resolve all of these elements independently throughout the mantle is not a reasonable approach, as the data are not capable of resolving so many parameters independently, and physical interpretation of such complicated structure would be far from straightforward. For this reason, many assumptions of material symmetry can be made to reduce the number of unknowns.

A common assumption is that the material has hexagonal symmetry, which means that the elastic properties are symmetric about an axis [*Babuska and Cara*, 1991]. This type of symmetry can be used to approximate, for example, macroscopic samples of deformed olivine (the dominant mineral of the upper mantle) [*Kawasaki and Konno*, 1984]. If the symmetry axis is arbitrarily oriented, this type of material can lead to observations of radial anisotropy (with a vertical symmetry axis), as well as azimuthal anisotropy, where velocities are dependent on the horizontal azimuth of propagation. However, with sufficient azimuthal coverage, the azimuthal variations will be averaged out, and we can instead focus only on the remaining terms related to a radially anisotropic model.

This reduces the number of independent elastic coefficients to 5. These have been traditionally defined by the Love coefficients: A, C, F, L, and N [*Love,* 1927]. These

coefficients can be related to observable seismic velocities:

$$A = \rho V_{PH}^2 \tag{4.1}$$

$$C = \rho V_{PV}^2 \tag{4.2}$$

$$L = \rho V_{SV}^2 \tag{4.3}$$

$$N = \rho V_{SH}^2 \tag{4.4}$$

$$F = \frac{\eta}{(A - 2L)}, \tag{4.5}$$

where ρ is density, V_{PH} and V_{PV} are the velocities of horizontally and vertically polarized P waves, V_{SH} and V_{SV} are the velocities of horizontally and vertically polarized S waves propagating horizontally, and η is a parameter related to the velocities at angles other than horizontal and vertical. Our dataset of long period waveforms is primarily sensitive to V_{SH} and V_{SV}, so we use empirical scaling parameters [*Montagner and Anderson,* 1989] to further reduce the number of unknowns to 2. Because the partial derivatives with respect to the other anisotropic parameters are small, the particular choice of scaling is not critical.

Although earlier models were developed in terms of V_{SH} and V_{SV} [*Gung et al.,* 2003], we choose to parameterize equivalently in terms of Voight average isotropic S and P velocity [*Babuska and Cara,* 1991], and three anisotropic parameters, ξ, ϕ, and η,

$$V_S^2 = \frac{2V_{SV}^2 + V_{SH}^2}{3} \tag{4.6}$$

$$V_P^2 = \frac{V_{PV}^2 + 4V_{PH}^2}{5} \tag{4.7}$$

$$\xi = \frac{V_{SH}^2}{V_{SV}^2} \tag{4.8}$$

$$\phi = \frac{V_{PV}^2}{V_{PH}^2} \tag{4.9}$$

$$\eta = \frac{F}{(A - 2L)}. \tag{4.10}$$

We invert for V_S and ξ, and scale V_P and density to V_S, and ϕ and η to ξ. This parameterization change is made so as to invert directly for the sense and amplitude of radial anisotropy in S velocity, the quantity of interest. Because damping in the inversion process leads to some degree of uncertainty in the amplitudes and anisotropy is related to the difference between V_{SH} and V_{SV}, inverting for these quantities and then calculating ξ could potentially lead to considerable uncertainty in the amplitude and even the sign of the resolved anisotropy.

The model is parameterized horizontally in terms of spherical harmonics to degree and order 16, which provides a nominal resolution of features on the order of 1000 km. In depth, the model is paramaterized in 16 cubic splines as in *Mégnin and Romanowicz,* [2000]. These splines are distributed irregularly in depth, reflecting the irregular distribution of dataset sensitivity with depth, with dense coverage in the uppermost mantle due to the strong sensitivity of surface waves, and also in the core-mantle boundary region, where reflected and diffracted phases have increased sensitivity.

4.2.2   Wave propagation theory and dataset

Our approach to tomographic inversion utilizes a dataset of three component long period time-domain ground acceleration seismic waveforms. These waveforms are modelled using non-linear asymptotic coupling theory (NACT) [*Li and Romanowicz,* 1995]. NACT is a normal-mode based perturbation approach, which computes coupling between modes both along and across dispersion branches. The asymptotic calculation of this coupling allows us to calculate two dimensional sensitivity kernels along the great circle path between source and receiver. These kernels show both the ray character of phases as well as the sensitivity away from the ray-theoretical paths due to the effect of finite-frequency data (Fig. 4.1).

In this study, we neglect off-plane focusing effects in the amplitudes, which we feel is reasonable since we reject data that exhibit strong amplitude anomalies, and, most importantly, our algorithm is primarily designed to fit the phase of the waveforms, which is much less affected by off-path effects than the amplitude. We also neglect the effects of azimuthal anisotropy, working from the premise that good azimuthal coverage of our data allows us to retrieve the azimuthally-independent anisotropic signal. There is ample evidence for azimuthal anisotropy in the earth's mantle, and our efforts should be viewed as representing only the first step towards a complete view of global mantle anisotropy.

Expressions for the coupled mode sensitivity kernels used in this approach have been developed for models parameterized in terms of the elastic coefficients A, C, F, L, and N [*Li and Romanowicz,* 1996]. The change to the radial anisotropy parameterization described above is accomplished with simple linear combinations of these kernels (see section 2.4). Although for fundamental mode surface waves sensitivity is dominated by V_{SH} for transverse component data and by V_{SV} for radial and vertical components, kernels for body waves and overtone surface waves show a much more complex sensitivity along the great-circle path (Fig. 4.1).

With this approach we are able to use a group velocity windowing scheme [*Li and Tanimoto*, 1993] to efficiently synthesize acceleration wavepackets and calculate partial derivatives with respect to model parameters. Dividing the time-domain waveforms into wavepackets allows a weighting scheme to avoid having larger amplitude phases dominate the inversion. For example, separating fundamental and overtone surface wavepackets allows us to increase the weight of the overtones, increasing sensitivity in the transition zone, while increasing the weight of smaller amplitude phases such as Sdiff and multiple ScS relative to large amplitude upper mantle phases such as SS increases our lowermost mantle sensitivity. The final dataset consists of 3 component surface and body wave packets from 1191 events (Table 4.1). The wavepackets were gathered using an automated picking algorithm (Appendix A).

To analyze the coverage of our dataset, we calculated the sensitivity kernels for every wavepacket in our dataset. For each wavepacket, we then calculated a root mean squared average over the time dependent sensitivity kernels and applied the weighting values used in our inversion, which account for waveform amplitude, noise and path redundancy. We then took the values for each great circle path kernel and summed them up in a global grid with blocks 5º by 5º and approximately 200 km in depth. The geographic coverage and depth dependence of sensitivity were then plotted normalized by surface area of each cell (accounting for the smaller cells near the poles) (Fig. 4.2A-F). Although this system is less intuitive than determining coverage using ray theory and determining ray density in a given cell, it is more applicable to our inversion, because the finite frequency data have sensitivity outside of the infinitesimal ray path and the sensitivity varies along the ray. In order to compare with a ray density approach, given our weighting system, a direct hit (i.e. a ray passing through the center of a cell) contributes $\sim 1 \times 10^{-10}$ to 5×10^{-10} (units are s^{-1}, as the kernels represent the modal frequency shift due to a relative perturbation of a model parameter). Phases with ray theoretical paths near a cell, however, can also contribute to the total sensitivity in that cell. The total for each depth range was also summed (Fig. 4.2G). Fundamental and overtone surface wave sensitivity is very strong in the upper mantle, and sensitivity generally decreases with depth, but note the increase in sensitivity in the lowermost 500 km due to the inclusion of phases such as S_{diff} and multiple ScS. The overall sensitivity to ξ is much lower than the sensitivity to isotropic velocity, but resolution tests indicate we can resolve anisotropic structure in most depth ranges of the mantle (see section 4.4.1).

The inversion of the dataset is done using an iterative least-squares approach [*Tarantola and Valette,* 1982]. This approach includes *a priori* data and model covariance matrices which we can use to apply a data weighting scheme [*Li and Romanowicz,* 1996], as well as constraints on the model norm, and radial and horizontal smoothness. Inversion iterations for anisotropic velocity structure were performed using the source parameters estimated by the Harvard CMT (Centroid Moment Tensor) project [*Dziewonski and Woodhouse,* 1983]. The reference model for our inversions is PREM

[*Dziewonski and Anderson,* 1981]. Because the starting model is important in non-linear iterative inversions, we started from the anisotropic model SAW16AN developed in Gung *et al.,* [2003] to describe the upper mantle. Although this is not a whole mantle model, it was shown to provide a good fit to the surface wave and overtone dataset, as well as to the body wave dataset not sensitive to the core-mantle boundary region. The lower mantle of the starting model is the same as that of SAW24B16 [*Mégnin and Romanowicz,* 2000], which is a model derived from transverse component only data. After the model reaches convergence (typically in three iterations), we iteratively invert for perturbed source parameters (location, origin time and moment tensor elements) for events with sufficient data [*Li and Romanowicz,* 1996]. Holding these parameters fixed, we recalculated the data fit for all wavepackets, adjusted the packet weighting, and then inverted for structural parameters again. The model converged in two iterations to the final model.

While the method remains much less computationally intensive than numerical approaches, the large number of wavepackets gathered (Table 4.1) can still require heavy computational resources. However, the calculation of the partial derivative matrix, which is the most computationally intensive step, can be very efficiently and naturally parallelized. The partial derivative matrices (multiplied by their respective transpose matrices and the a priori data covariance matrix) for each event can be calculated independently with minimal redundancy, and then combined linearly. Using this approach on a 16 node cluster of dual-processor machines enables us to perform model iterations in a few days, which allows us to ensure convergence as well as analyze subsets of the data to obtain estimates of the statistical error of our models.

Table 4.1: Summary of wavepackets used in inversion

Wavepacket type	Component	Min. period (s)	wavepackets	data points
Body	Z	32	12,469	274,927
Body	L	32	9672	207,283
Body	T	32	15,076	160,627
Surface	Z	60	36,100	2,101,379
Surface	L	60	16,373	984,183
Surface	T	60	21,101	802,913
Surface	T	80	9824	111,719
	Total		120,615	4,643,031

For component column, Z refers to vertical, L to longitudinal (along the great circle path between source and receiver), and T to transverse (perpendicular to L). The maximum period for each wavepacket is determined by event magnitude and ranges from 220s to 1 hour. The 80s T surface waves represent the surface wave dataset of *Li and Romanowicz*, [1996]

4.3 Model results

4.3.1 Isotropic velocity model

The isotropic portion of the model (Fig. 4.3) is quite similar to previous S velocity tomography models. Figure 4.4 shows the correlation as a function of depth with several recent tomographic models [*Ekström and Dziewonski,* 1998; *Gu et al.,* 2001; *Ritsema and van Heijst,* 2000; *Masters et al.,* 2000; *Mégnin and Romanowicz,* 2000]. The correlations in this figure were calculated by expanding each of the models in spherical harmonics up to degree 24 at the depths of the knots of the radial splines in the parameterization of SAW16B16-AN. The correlation is then calculated over the set of spherical harmonics coefficients up to degree and order 16. The correlation is quite good with all models in the uppermost 200 km, but the models diverge somewhat in the transition zone, and more strongly in the mid-mantle range between 800 and 2000 km depth where amplitudes are low, and are closer in agreement in the lowermost mantle. The correlation is, not surprisingly, strongest with SAW24B16

[*Mégnin and Romanowicz,* 2000], which was the starting model in the lower mantle, as well as being derived from some common transverse component data. SB4L18 [*Masters et al.,* 2000] diverges most strongly in the upper mantle, but is actually the best-correlated in the lower mantle, while the two Harvard models, S362D1 [*Gu et al.,* 2001] and the isotropic portion of S20A [*Ekström and Dziewonski,* 1998], are the most divergent models in the lowermost mantle. A similar pattern of correlation as a function of depth is seen when any of the other models are compared to the whole set of models, placing the isotropic portion of this model well within the scatter of previously published tomographic models.

The common features of S tomographic models are present in the isotropic velocity model. The uppermost 200 km is dominated by tectonic features, with fast continents and slower oceans that show an age-dependent increase in velocity away from the slow velocities near ridges. Regions of active tectonic processes are, in general, slower, such as western North America, the major circum-Pacific subduction zones, and the East African rifting. In the transition zone depth range, the most prominent features are the fast velocities of subducted slabs, while the slow ridges are no longer present. Mid-mantle velocity anomalies are low in amplitude, and more white in spectrum. Finally, in the lowermost 500 km, the amplitudes of heterogeneity increase again, and become dominated by a degree 2 pattern with rings of higher velocities surrounding two lower velocity regions under the central Pacific and Africa, commonly referred to as superplumes.

The first-order control on the fit to the data is the isotropic portion of the model, and this structure is therefore quite stable, whether anisotropy is included in the model or not. Just the isotropic portion of SAW16B16-AN leads to a variance reduction of 49.7%, while adding anisotropy improves the variance reduction to 55.7%. While this improvement in fit is certainly significant above the 99% confidence level according to an F-test criteria given the large number of degrees of freedom of our modelling [*Menke,* 1989], the isotropic model is obviously the more important control. To demonstrate the stability of the isotropic structure, we performed an inversion it-

eration starting from the isotropic portion of the final model, without allowing any anisotropy, aside from that of the reference model. The resulting isotropic structure is nearly visually indistinguishable, with correlation ranging between 0.92 to above 0.99 as a function of depth with an average of 0.97.

4.3.2   Upper mantle anisotropy

The ξ structure above 400 km (Fig. 4.5A,C,E) is similar to that of Gung *et al.*, [2003], (hereafter referred to as GPR03) with an average correlation coefficient of 0.72 across this depth range. However, there are some notable differences in the structure when they are compared in detail (Fig. 4.5). The positive $\delta \ln \xi$ signature under oceans observed previously [*Montagner and Tanimoto,* 1991; *Ekström and Dziewonski,* 1998] continues to greater depths. Although the signature under continental roots discussed in GPR03 still remains in this model, it is slightly lower amplitude and somewhat obscured by the oceanic signature at depth. Despite the differences, the implication of $V_{SH} > V_{SV}$ anisotropy generated in the asthenosphere at different depths beneath the oceanic and continental lithosphere remains.

The differences between this model and the GPR03 model can be explained by the differing vertical resolutions of the two datasets. Although the much greater number of body waves in the current modelling greatly improves coverage in the transition zone and lower mantle, it does apparently introduce some vertical smearing in the uppermost mantle. Additionally, the damping scheme chosen for this model was designed to obtain a radially smooth model. This was not a primary consideration in GPR03, and so a somewhat rough model of V_{SH} and V_{SV} was obtained, with even more pronounced radial roughness when the model is converted to V_S and ξ (Fig. 4.6).

In the new model, a negative $\delta \ln \xi$ signature is apparent associated with the ridges between 200 and 300 km depth. For the fast-spreading ridges of the Pacific and Indian Oceans in particular, there appears to be a strong correlation between the amplitude

of the negative $\delta \ln \xi$ signature and the spreading rate of the ridge. To quantify this relationship, we defined a series of ridge segments approximately 7.5° in length for all major mid-ocean ridges (Fig. 4.7). For each segment we compared the value of $\delta \ln \xi$ with the spreading rate. Spreading rates were calculated by taking the component of relative velocity perpendicular to each ridge segment as calculated using NUVEL-1 [*DeMets et al.*, 1990] evaluated at the midpoint of each segment. For quantitative comparison purposes, we used all segments with spreading rates greater than 5 cm/yr (displayed in blue and green in Fig. 4.7), all of which are located in the eastern and southern Pacific and southern Indian Oceans. The spreading rates compared with $\delta \ln \xi$ values at 200 and 250 km depth are shown in Fig. 4.8. Most values are negative, although there are a few positive values for spreading rates less than 7.5 cm/yr. If we perform a linear regression on the correlation of the $\delta \ln \xi$ values at 200 and 250 km depth compared with the spreading rates, we fit the data with R^2 values (which is a measure of goodness-of-fit which ranges from 0 to 1, with 1 meaning a perfect fit) of 0.26 and 0.3, respectively. Given the number of segments used in the regression, both of these values represent a significant relationship between $\delta \ln \xi$ and spreading rate at or above the 99% confidence level according to an F-test. The p-values, which indicate the probability that the misfit of the linear regression is equivalent to a line with a slope of zero, are 0.005 and 0.002 for 200 and 250 km respectively. However, it appears that the segments nearest the subduction zones at the northern end of the East Pacific Rise, and the spreading segment between the Cocos and Nazca plates west of South America have anomalously low values of $\delta \ln \xi$, perhaps explained by interaction with the vertical flow of the nearby subduction zone. When these 4 segments (shown in blue in Fig. 4.7) are excluded from the regression analysis, the best-fit slopes become more strongly negative, and the R^2 values increase to 0.51 and 0.59 for 200 and 250 km depth, respectively. This represents a significant relationsip above the 99.99% confidence level, with p-values less than 0.0001. This significant correlation between the variation of surface spreading rates along several ridge systems and amplitude of anisotropy at depth strongly supports development of $V_{SV} > V_{SH}$ due to vertical flow beneath fast-spreading mid-ocean ridges, although in some slower spreading regions, there remains the $V_{SH} > V_{SV}$ common away from the ridges under oceanic regions

due to horizontal deformation.

4.3.3 Transition zone anisotropy

While anisotropy at transition zone depth ranges (400-700 km) is not included in global models such as PREM [*Dziewonski and Anderson,* 1981], several studies have indicated the possible presence of anisotropy in this depth range [*Montagner and Kennett,* 1996; *Fouch and Fischer,* 1996; *Trampert and van Heijst,* 2002; *Beghein and Trampert,* 2003]. While the amplitudes of anisotropy observed in our model are lower than those in the uppermost mantle (Fig. 4.9), there is a clear signature present in this depth range.

The most prominent feature of the model in this depth range (Fig. 4.10) is the association of negative ξ perturbation ($V_{SV} > V_{SH}$) with subduction zones. Below 400 km depth, there is a clear correlation of negative ξ perturbations both with the high isotropic velocities usually associated with slabs, as well as the predicted locations of slabs from a geodynamic model based on reconstructed subduction history over the last 180 million years [*Lithgow-Bertelloni and Richards,* 1998] (Fig. 4.11). This signature fades rapidly below the 670 discontinuity, even though some isotropic velocity anomalies continue. These observations suggest that quasi-vertical flow in the subduction zones leads to observed anisotropy, perhaps through a mechanism related to alignment of spinel crystals or through alignment of pockets of strongly contrasting garnetetite derived from oceanic crust [*Karato,* 1998b].

The ridge signal of negative ξ anomalies, which is prominent in the uppermost 300 km of the model, vanishes under most ridges, with the exception of the East Pacific Rise, where it appears to continue to approximately 500 km depth although the isotropic anomaly does not extend to such depths. The lack of a similar $V_{SV} > V_{SH}$ signature as in the subduction zones under most mid-ocean ridges suggests that these are more shallow features, as seen in isotropic velocity [*Montagner and Ritsema,* 2001] and

attenuation models [*Romanowicz and Gung,* 2002].

Fouch and Fischer, [1996] also observed anisotropy in the transition zone depth range from shear wave splitting measurements of local S and teleseismic SKS associated with some (but not all) subduction zones in the Northwest Pacific. Specifically there was evidence for splitting extending to at least 480 km and perhaps through the transition zone into the uppermost lower mantle under the Southern Kuril arc (Sakhalin Island), as well as possibly beneath western Honshu in Japan. The anisotropy was constrained to shallower depths beneath the Izu-Bonin trench to the south, where our model also shows no negative ξ perturbation. As these were splitting measurements, they only measured azimuthal anisotropy in a horizontal plane, so the sense of anisotropy cannot be directly compared. The directions, however, ranged from roughly trench parallel to 35° from parallel, which is not consistent with the trench perpendicular azimuth which might be expected from a simple model of quasi-vertical flow coupled to the downgoing slab, as suggested by our radial anisotropic model. Likely the motion would have to be a combination of downward flow coupled to the slab and some trench parallel or sub-parallel shear, although the trench parallel component observed in splitting measurements, which have little depth resolution, may be primarily in the uppermost 200 km [*Hall et al.,* 2000].

Comparing this model with other previous models of transition zone anisotropy is, however, problematic. *Montagner and Kennett*, [1996], using normal mode data and a variety of 1D starting velocity models to invert for 1D anisotropy and attenuation structure, observed a radially symmetric signal of positive ξ perturbations above the 670 changing to negative perturbations below the 670. The degree 0 (radially symmetric) portion of our ξ model (Fig. 4.12) does not match this pattern. We observe little degree 0 term immediately above the 670, with a positive bump in the top of the lower mantle. However, this signature in the *Montagner and Kennett*, [1996] model showed some dependence on the starting model used as well as a reduction in amplitude when they also inverted for the isotropic velocity parameters, suggesting there could be a tradeoff with the depth and isotropic velocity contrast across the

670. Additionally, the depth range of this degree 0 signature relative to the 670 discontinuity is possibly not well constrained in our model. For example, if we fix ϕ to that of *Boschi and Dziewonski*, [2000] and scale η to ϕ (see section 4.4.3), or if we constrain the lower mantle to isotropy (as discussed in 4.3.4), the positive degree 0 signature shifts above the 670 discontinuity.

While the earlier work on low-degree azimuthal anisotropy in the transition zone by *Trampert and van Heijst*, [2002] is not directly comparable, we note that general amplitude levels of $\sim 2\%$ are compatible between these studies. *Beghein and Trampert*, [2003] also look at radial anisotropy in the transition zone, although due to their guided model space sampling approach, they do not present a single preferred structural model. Instead they choose to look at the distribution of likely models grouped into tectonically-defined regions, making a direct comparison difficult. In general, they see little to no ξ signature in the transition zone when averaged over these larger regions, with the exception of young oceanic regions under or near ridges, where they see a preference for models with $V_{SH} > V_{SV}$ (note the difference in sign convention for ξ in their work compared with ours). While this is inconsistent with the ridge signature seen in our model under the East Pacific Rise, such a signature is seen under other ridge segments, although low in amplitude. It is possible that the inconsistency due to greater depth extent of the anomaly under the EPR could be explained by the vertical smearing discussed in 4.3.2. The strong subduction signature of $V_{SV} > V_{SH}$ of our model is absent in the models of *Beghein and Trampert*, [2003] in the analysis of regions under older oceanic plates and tectonically active regions under continents, although of course these are averages over larger regions than just the subduction zones. Although the reasons for differences in the modelling results are not obvious, their modelling only includes fundamental and overtone surface waves. The addition of body waves in our dataset greatly improves the sampling, particularly in subduction regions.

4.3.4 Mid-mantle anisotropy

The amplitude of anisotropic structure in the model in the bulk of the lower mantle is lower than that of both the lowermost mantle and the upper mantle. Mineral physics and seismology both suggest that the bulk of the lower mantle is nearly isotropic [*Meade et al.,* 1995]. *Meade et al.* noted that the amount of shear-wave splitting observed above a subduction zone was nearly the same for direct waves, SKS waves, and ScS waves, ruling out large regions of azimuthal anisotropy in the bulk of the lower mantle below the downgoing slab. Although the radial anisotropy measured in this study does not produce shear wave splitting, it is unlikely that large regions of radial anisotropy would exist in this depth range without accompanying azimuthal anisotropy. LPO mechanisms do not, in general, produce such a structure. Although purely horizontally aligned layers or inclusions with no tilt can produce radial anisotropy without significant azimuthal anisotropy, generating such a structure in the mid-mantle, where mass transfer is likely to be primarily vertical, is also doubtful.

Given this evidence that even relatively small anisotropy is unlikely in this region, we need to ask whether our modelling requires anisotropic structure in this depth range, and whether its inclusion has any effect on the structure in other depth ranges. To test this, we performed inversions starting from the isotropic portion of the velocity model used for inversion for source parameters, using the Harvard CMT sources and original data weighting to avoid bias towards our final post-source inversion model. We performed test inversions from this isotropic model where anisotropic structure was allowed in all depth ranges, as well as tests with it constrained to be isotropic in two depth ranges describing the mid-mantle, namely from 670 to 2400 km depth and between 1200 and 2400 km depth (Table 4.2 and Fig. 4.13). For the latter model (model D), there was negligible effect on the recovered structure in other depth ranges, and the change in fit to the data when comparing models was very small (Table 4.2). There was no change in the fit to the surface waveforms, and allowing anisotropy in this depth range only improved the data fit for the body waveforms by 0.26%. When the constraint of isotropy is extended up to 670 km depth, there is some tradeoff with

Table 4.2: Correlation of ξ for constrained models to fully anisotropic model and change in fit to data

Depth range	Model				
	A	B	C	D	E
25-200	0.985	0.997	0.999	0.999	-
200-700	-	0.932	0.934	0.999	-
700-1200	-	-	-	0.999	-
1200-2400	-	-	-	-	-
2400 - 2891	-	-	0.970	0.989	-
Data	Change in data fit (%)				
Body	-2.52	-1.41	-1.11	-0.26	-8.69
Surface	-0.58	-0.34	-0.33	0.0	-9.42
Total	-1.35	-0.77	-0.64	-0.10	-9.13

Correlation for various depth ranges of constrained models compared with model with anisotropy allowed in whole mantle. Model letters are the same as in Fig. 4.13 with constrained depth regions marked as "-". Model E is the isotropic starting model for all the test models. Although the correlation curves in Fig. 4.13 show non-zero values at borders of constrained regions as an artefact of the spline parameterization, those values are not reported here. Changes in fit are the ratio of estimated data variance for each model for the body wave, surface wave, and full dataset relative to the data variance estimated for the fully anisotropic inversion.

structure in the lower portion of the upper mantle transition zone, with correlation to the fully anisotropic model dropping to 0.89 averaged over the transition zone. The primary difference in the anisotropic structure of the lower portion of the transition zone is in the degree 0 term, as the transition zone correlation is 0.97 compared to the fully anisotropic model when the degree 0 terms are neglected. The degree 0 positive $\delta \ln \xi$ immediately below the transition zone (Fig. 4.12) is shifted upward when the anisotropy is constrained to zero below 670 km. The change in fit to the data is also slightly more pronounced when this constraint is applied, with the fully anisotropic model showing a 0.5% better fit to the overall data set, and a 0.9% better fit to just the body waveforms.

4.3.5   Core-mantle boundary region anisotropy

The final model in the lowermost mantle (Fig. 4.14) is similar in low degrees to the model of anisotropic structure for the core-mantle boundary (CMB) region developed in *Panning and Romanowicz*, [2004], hereafter referred to as PR04, which was constrained to degree 8 for lower-mantle ξ (Fig. 4.15). As in that model, the degree 0 term is prominent (fig. 10), and corresponds to a positive ξ anomaly ($V_{SH} > V_{SV}$) on the order of 1% averaged throughout the depth range. The large-scale pattern is also similar (correlation coefficient of 0.74 averaged over the bottom 300 km), although there are notable differences beneath Antarctica and Africa, where the coverage is poorest (Fig. 4.2).

Although the model parameterization is the same in PR04, and the dataset is similar, the inversions leading to the two models differ primarily in two respects. The PR04 model was a single iteration model using Harvard CMT solutions, while multiple iterations were performed for the model discussed in this paper, as well as inversion for source parameters for most events. Even more importantly, the scaling of V_P and ρ to V_S and η and ϕ to ξ in the PR04 model was not correctly applied in the inversion code, with V_P and ρ scaling coefficients mistakenly interchanged with η

and ϕ coefficients. Despite the considerable difference in scaling used, including a change of sign, the results are markedly similar. This suggests that the scaling used does not have a strong influence on the anisotropic structure in this depth region, except where the coverage is poorest, as might be expected given the low sensitivity of our dataset to ϕ and η structure, compared with ξ. To test this conclusion, we also performed inversions where no scaling is assumed and where the ϕ structure is derived from the anisotropic P model of *Boschi and Dziewonski*, [2000] (with η scaled to ϕ) (section 4.4.3). All 3 models are quite similar in the CMB region (Fig. 4.16A-C), with differences primarily under Antarctica and Africa. Due to the dataset having very little sensitivity to ϕ and η, it appears that the scaling assumptions only have a significant effect in regions of the model with the poorest coverage.

Previous studies have also shown that CMB topography can exhibit tradeoffs with anisotropic structure [*Boschi and Dziewonski,* 2000]. Although that study contained numerous reflected and transmitted P phases, and so could attempt to model CMB topography, at least in areas with sufficient coverage, our S dataset is dominated by reflected and diffracted phases, and so is not as well suited for definitive modelling of the boundary structure. Therefore, we inverted the dataset not including source inversions and chose a damping scheme that obtained amplitudes of topography compatible with previous work [*Morelli and Dziewonski*, 1987; *Boschi and Dziewonski,* 2000] in order to determine what kind of tradeoffs might be present (Fig. 4.16D). We did not, however, include this topography in our final model. The degree 0 term was not influenced by the inclusion of CMB topography, but there is some change in the relative amplitudes of the lateral anisotropic stucture imaged in our model, with a slight decrease in the amplitude of the anomalous regions in the central and eastern Pacific, and an increase in the amplitude of the anomaly under Africa, as well as strong increases in the anomalies under central Asia and Antarctica.

In PR04, it was noted that the two broad regions that most deviated from the average degree 0 signature corresponded to the superplume regions of low isotropic velocity, although there were also regions of reduced ξ west of North America and under cen-

tral Asia. In this improved model, although the pattern is very similar to PR04, it is apparent that the regions of negative and reduced ξ are clearly offset from the centers of the superplumes as defined by the isotropic velocity structure. Qualitatively, these regions appear to be more associated with the transitions from high to low velocities at the boundaries of the superplumes, particularly around the Pacific superplume, where the model is most consistent with previous work, and coverage is best. In the current model, the anisotropic signature of the African superplume is much less well-defined. As discussed above, the structure of this region appears to be sensitive to the assumed scaling relationships as well as CMB topography, and so conclusions about the anisotropic structure in this region are problematic. However, the preferred model does include a reduction in the positive $\delta \ln \xi$ signature under eastern Africa, corresponding to the region of highest gradient between fast and slow isotropic velocities.

Although these observations do not uniquely constrain the mineral physics or dynamics of the lowermost mantle, they remain suggestive of a model where considerable anisotropy is generated in the primarily horizontal flow at the mechanical boundary layer under downgoing slabs, either through a mechanism of LPO [*McNamara et al.,* 2002; *Iitaka et al.,* 2004; *Tsuchiya et al.,* 2004] or SPO [*Kendall and Silver,* 1996]. In fact, recent theoretical and experimental studies have demonstrated the possible stability of post-perovskite phase of $MgSiO_3$ in the lowermost 300 km of the mantle [*Iitaka et al.,* 2004; *Tsuchiya et al.,* 2004]. These studies show this phase to have a greater single crystal elastic anisotropy at lowermost mantle pressures than the perovskite thought to make up the bulk of the lower mantle, at least for 0K theoretical work [*Iitaka et al.,* 2004]. Although neither the alignment behavior nor the temperature dependence of anisotropy for this material are known, the theoretical studies suggest a difference in V_{SH} and V_{SV} of a few percent approximately 200-300 km above the CMB is possible based on the 0K results [*Tsuchiya et al.,* 2004]. As the material approaches regions of large-scale upwelling, however, this signature changes, and we see a reduction in observed anisotropy, with some negative $\delta \ln \xi$ regions observed in the central and eastern Pacific. These signature changes do not align with the center

of the superplume regions, but appear to be strongest near the edges as the structure transitions from high to low velocity. There are a number of possible mechanisms for this, including rotation of the anisotropic material [*McNamara et al.*, 2002], inclusions of vertically oriented melt pockets, or perhaps a lesser presence of the post-perovskite phase, due to the higher temperatures and the positive Clapeyron slope of the phase transition from the perovskite phase [*Iitaka et al.*, 2004; *Tsuchiya et al.*, 2004].

4.3.6   Source parameters

For the initial iterations of the inversion, the published Harvard CMT solutions were used. However, these solutions were derived using a longer period dataset and an isotropic shear velocity model. To improve the fit to the data, we choose to invert for the 10 source parameters (latitude, longitude, and depth of the centroid, plus origin time and the 6 independent moment tensor elements), and use these revised solutions to further refine the structural model.

To avoid unrealistic solutions, we first constrained the explosive component of the moment tensor to 0 (as in the original Harvard CMT solutions used), reducing the number of unknowns by one. Because the source inversion is non-linear, we performed 3 iterations for each event. Of the 1191 events in our dataset, 1108 (93%) had sufficient data for a stable inversion which showed convergence. Before using these data for further structural inversions, we compared the resulting solutions to the original Harvard solutions. To compare the changes in mechanism, we use the moment tensor difference function [*Pasyanos et al.*, 1996],

$$\mu = \sqrt{\frac{\sum_{i=1}^{3} \sum_{j=1}^{3} (M_{ij}^{(1)'} - M_{ij}^{(2)'})^2}{8}}$$

where $M_{ij}' = M_{ij}/M_0$ and M_0 is the scalar seismic moment. This function varies between 0 and 1, with 0 representing identical mechanisms, and 1 representing a double-couple with exactly the opposite sense of motion. For values of $\mu < 0.25$,

the mechanisms are essentially the same, while for $\mu > 0.5$, the mechanisms are significantly different. Only 4 of the inverted mechanisms had values of $\mu > 0.25$ and none had $\mu > 0.5$, indicating that the differences are small, as would be expected given the fact that the Harvard solutions were already good fits to the data.

However, there was a systematic bias in inverted M_0, with an average decrease in the final value of M_0 by 16% (or a decrease in M_W of 0.05) (Fig. 4.17). This bias is similar to the shift of 0.075 magnitude units when comparing regional estimates of M_W calculated by spectral and time-domain approaches [*Pasyanos et al.*, 1996]. It is also comparable to the 0.1 unit downward shift seen by *Dziewonski and Woodhouse*, [1983] between the best fit relationship of M_W calculated from Harvard CMT solutions to M_S and the theoretical relationship between M_W and M_S [*Kanamori*, 1977]. In both cases above, the recovered moment is likely decreased in order to minimize misfit due to poor fits in phase relative to a method that does not require phase matching, such as spectral estimation of M_W or the determination of M_S. Because our dataset of body waveforms and surface waveforms with cutoff periods of 32 and 60 seconds respectively is higher frequency than that used by the Harvard CMT methodology (45 and 135 seconds), the bias due to difficulty in matching phase is even more pronounced.

Because the lower seismic moments recovered using the above method were likely biased, we performed the source inversion again, with the seismic moment fixed to that of the Harvard CMT solution, reducing the total number of unknowns per event to 8. Given this more constrained inversion, a smaller number of events converged with sufficient improvement in fit to the data (964 events or 80.9% of the events). Of these events only 2 had values of μ slightly greater than 0.25 (with values of 0.26 and 0.27), showing the changes in mechanism to once again be small when the scalar moment is fixed.

Location changes are also, in general, quite small. Depth shifts average less than 4 km, with no significant bias deeper or shallower. Horizontal location shifts average

0.015º with no single shift greater than 0.1º. When the vector shifts are summed in 5º by 5º cells, areas associated with active subduction zones around the Pacific show some constructive stacking (Fig. 4.18), suggesting systematic, albeit small, source relocation due to the improved structural model. When the shifts in Figure 4.18 are normalized by the number of events in each cell, the subduction zone shifts are significantly reduced, as those cells have the highest event density, but the stacking in those cells is still significant. To demonstrate this significance, we can look at two quantities. The average azimuthal deviation, Θ, can be defined as

$$\Theta = \frac{1}{N} \sum_{i=1}^{N} |\theta_i - \theta_0|,$$

where N is the number of events in a cell, θ_i is the azimuth of the relocation of a single event, and θ_0 is the azimuth of the vector sum of all event relocations in the cell. We also define the stacking efficiency,

$$E = \frac{|\mathbf{V}|}{\sum_{i=1}^{N} |\mathbf{v}_i|},$$

where $|\mathbf{V}|$ is the magnitude of the vector sum of the cell's event relocations, and $|\mathbf{v}_i|$ is the magnitude of each event's relocation vector. For relocations that are all identical in direction $\Theta = 0º$ and $E = 1.0$, while for a set of relocations that is sufficiently large and entirely random in magnitude and azimuth, we would expect $\Theta = 90º$ and $E = 0.0$. For the 14 cells with a vector-summed location shift with a magnitude greater than 0.1º, the average value of Θ, weighted by number of events in the cell, was 4.6º, and the average value of E was 0.58. In order to demonstrate that this degree of stacking is systematic, we performed the vector sum on 100,000 realizations of the event relocations in these 14 cells given the same magnitude of offsets, but random azimuths (i.e. no systematic offsets). The mean value of Θ was 90.2º. 99.9% of the random realizations had $\Theta > 71.4º$. The mean value of E was 0.31, and 99.9% had $E < 0.44$. We can say with a high level of confidence that the source inversions with the improved velocity model are systematic, though small.

4.4 Model resolution and error

4.4.1 Resolution matrix tests

A common way of analyzing the resolution of a model from a least-squares inversion is to utilize the resolution matrix. Using this approach, it is possible to get an idea of the model resolution given the dataset's sensitivity, and the *a priori* damping scheme applied. It does not, however, assess uncertainties resulting from the theoretical approximations in the partial derivative calculation, or due to errors in the data aside from the effect of the *a priori* data covariance matrix applied as a weighting factor to the data points in the inversion.

Given these limitations, this approach allows us to perform the standard 'checkerboard' tests to obtain an estimate of the geographical resolution of the model parameters. The isotropic velocity model is well-resolved through degree 16. Figure 4.19 shows the output model for an input degree 16 pattern (Fig. 4.19A) at a variety of depths both with (Fig. 4.19C) and without (Fig. 4.19B) anisotropy in the input model. The pattern is well captured, although there is some reduction in amplitude. The resolution for ξ is, not surprisingly, not as good (Fig. 4.20). The highest degree structure is not resolved at all, except in the shallowest depth ranges. For the lowermost mantle, the input checkerboard model shown in Fig. 4.20A only includes degree 4 structure. The pattern of structures up to approximately degree 10 is also recovered (not shown), but the amplitudes are reduced strongly. In some depth ranges, there also appears to be some amount of tradeoff with unmodelled isotropic velocity structure, as shown in Figure 4.20C, in which the input model also contains isotropic structure equivalent to the input model shown in Figure 4.19A. This effect is most noticeable in the lower transition zone and uppermost lower mantle, as well as to a lesser extent in the southern hemisphere in the lowermost mantle.

We also tested the depth resolution of the modelling. We used an input model of

random ξ structure with a white spectrum through degree 16, and compared the input and output amplitude as a function of depth (Fig. 4.21). For each depth range, there is some amount of smearing. Notably, a small percentage of mid-mantle structure is mapped into the transition zone (Fig. 4.21D-F). This is probably not a large concern, as anisotropic structure in the mid-mantle is expected to be negligible, but it is important to be aware of it when interpreting transition zone structure. Structure in either of the lowest two splines (Fig. 4.21G,H) maps into a similar pattern with a peak at the CMB. This confirms the poor resolution of the depth distribution of anisotropy in the lowermost mantle discussed in PR04.

4.4.2 Bootstrap and jackknife error estimates

Formal errors are difficult to calculate for model parameters in a damped least-squares inversion. One way to estimate the model errors, given our inversion process is through a bootstrap approach [*Efron and Tibishirani,* 1993]. The bootstrap is a general statistical approach to calculating the standard error of the value of any estimator, θ. In our case, θ is the set of partial derivative and matrix calculations leading from the dataset of seismic waveforms to our model. The bootstrap standard error is calculated by applying the estimator to a sufficiently large set of random samples of the data, and analyzing the standard deviation of the models estimated from each sample. Although, our dataset has millions of points (Table 4.1), we simplify this approach by considering 12 subsets of the data formed by separating the data by the month of the event, and considering those as our sample population. A bootstrap sample is then any set of 12 subsets selected from that population with replacement. For any set of n observations, there are n^n bootstrap samples, although many of these are exchangeable (i.e. $x_1, x_2, ...x_n$ is the same as $x_2, x_1, ...x_n$). Even taking into account that exchangeability, there are more than 1,300,000 possible bootstrap samples of our 12 subsets, which is far too many to reasonably calculate, but the bootstrap approach will in general converge relatively quickly. We choose to make 300 bootstrap resamples, and then generate maps of the estimated errors (Fig. 4.22).

A similar approach which is somewhat less computationally intensive is the delete-d jackknife error estimation. In this approach, the model is calculated for a series of n datasets which leave out d observations at a time, and the standard error is calculated as

$$\hat{se}_{jack} = \sqrt{\frac{n-d}{d \cdot C(n,d)} \sum (\theta_{(i)} - \bar{\theta})},$$

where $C(n,d)$ is combinatorial notation indicating the number of subsets of size d from a population of n chosen without replacement, the sum is over the $C(n,d)$ possible jackknife samples of the dataset, $\theta_{(i)}$ is the estimator value for the ith jackknife sample, and $\bar{\theta} = \sum \theta_{(i)}/(C(n,d))$. This is basically the standard deviation of the models multiplied by an inflation factor roughly equal to n for $d = 1$ and smaller values for $d > 1$, where the datasets are less similar to the original dataset. If we use the same 12 subsets as above, only 12 models need to be calculated for $d = 1$, or 66 for $d = 2$.

All three estimates of the error in the maps are virtually identical, with a correlation above 0.99 at all depth ranges, and amplitudes within a few percent. Therefore we only show the error maps from the bootstrap approach. The consistency of the three estimates is a cross-check that we performed enough bootstrap resamples. The error estimate for isotropic V_S is consistently low throughout the mantle, with a small increase in the lowermost mantle (compare error amplitude in Fig. 4.22K with model amplitude in Fig. 4.9). In pattern, the error in this lowermost depth ranges appears to mirror the coverage in Figure 4.2, with slightly larger error estimates in the southern hemisphere particularly under Africa and the eastern Pacific. The ξ errors are larger in the upper mantle, but similar to the errors in V_S in the lower mantle. The pattern is different, though, with the largest error in the upper mantle being roughly correlated with strong gradients in structure. In the lower mantle, the regions of greatest error are associated with the greater complexity of structure near the Pacific superplume, as well as in the regions of poorer coverage under Antarctica and the southeastern Pacific.

This approach to error estimation, like the resolution matrix testing, also does not directly treat errors related to the changes in the choice of damping or theoretical assumptions. These error maps show how random errors in the data will map into the observed structure, given the damping and inversion scheme used to develop the model.

4.4.3 Other possible sources of error

Crustal correction and other discontinuities

An important consideration in any study of mantle structure is the corrections for crustal structure. In our modelling, we use a somewhat ad-hoc method to describe the anisotropic crustal structure. For the transverse component data we correct the data for the topography of the seafloor and Moho discontinuities derived from the modelling of transverse component data in the development of SAW24B16 [*Mégnin and Romanowicz,* 2000]. For the vertical and radial component data, we use the discontinuity perturbations of *CRUST 5.1* [*Mooney et al.*, 1998], which were derived using Rayleigh waves, and are thus more appropriate for V_{SV} sensitive data.

To test what kind of effects this simplified approach has on our recovered velocity models, we replaced the separate crustal models with a single one defined by the average of the two, and inverted simultaneously for velocity and perturbations to the seafloor and Moho discontinuities, using the Harvard source mechanisms. Changing the crustal model led to a 9.8% decrease in variance reduction, which was primarily due to the 21% decrease in variance reduction for the fundamental mode surface waves, while the overtone surface waves saw little change in fit, and the body waves saw a 4.7% decrease in variance reduction. The resulting mantle velocity model, however, was similar. The isotropic velocity model was correlated at an average of 0.89 for the whole mantle, with a minimum of 0.77 occuring in the transition zone at $\sim$500 km (Fig. 4.23A). The changes in ξ were slightly larger, with an average correlation of 0.80

across the depth range, with more significant decreases in correlation around 1600, 2000 and 2500 km depth dropping as low as 0.4 in the vicinity of 1600 km depth. These depths, however, correspond to changes from positive to negative degree 0 ξ anomalies, which are slightly offset with the more simplified crustal model. When the degree 0 terms are neglected, the correlation is above 0.8 throughout the mantle, with the exception of a small decrease between 1200 and 1800 km depth.

The 670 discontinuity and the core-mantle boundary also are likely to have topography. We performed an inversion where these discontinuities were allowed to vary in order to assess tradeoffs with the velocity structure. To avoid strong bias towards a model similar to our final model, we used the Harvard CMT sources, and the starting velocity model is the same as that used for the source inversions, with the data weighting scheme used to develop that model. The isotropic velocity model is stable, with the velocity model including topography correlated with that of the final model (Fig. 4.23B) with a correlation coefficient averaged across the depth range equal to 0.94, and averaging 0.99 when compared to the velocity model obtained before the source inversion.

The anisotropic patterns are also, in general, stable. The model is well correlated with the final model (average correlation coefficient across the whole mantle of 0.88), and most of this difference can be related to the changes in the model after the source inversions, as the model has an average correlation coefficient of 0.98 when compared with the model used for the source inversions, which was also the starting model for the inversion. The 670 topography does not appear to exhibit a very strong influence on the anisotropic structure resolved near the discontinuity, as the correlation exhibits only a small change in that depth range. The larger changes in structure are in the lowermost mantle and near a depth of 1600 km. The mid-mantle structural change appears to be due to the inclusion of the source inversion in the final model leading to a slight shift of the zero crossing of the degree 0 ξ signature, and is not directly related to topography on either discontinuity. The change in the CMB region is discussed in section 4.3.5, and is primarily a change in relative amplitudes of anomalous regions,

while the strong degree 0 signature is unaffected (Fig. 4.16D).

Scaling parameters

The anisotropic scaling parameters used in our modelling were derived for deformation of upper mantle materials above 400 km [*Montagner and Anderson,* 1989]. Obviously, it is reasonable to question the validity of this scaling assumption at greater depths. To test the influence of the assumed scaling parameters on our model, we performed tests with the ϕ model fixed to that of *Boschi and Dziewonski,* [2000]. We then scaled the 3D η structure to this ϕ model. For our first test, we fixed the ϕ and η structures, and then inverted the pre-source inversion dataset for ξ structure starting from a model with no ξ perturbations. We also performed an inversion where the ξ, ϕ, and η structures were simultaneously inverted starting from the ξ model used in the source inversions, and the ϕ and η model described above. We also attempted an inversion for all 3 anisotropic parameters starting from an initially isotropic model, but the very small ϕ and η sensitivities of our dataset led to a very unstable inversion, which we do not consider further here.

In general, the correlation of the ξ models derived in these tests agreed well with the final, preferred ξ model (Fig. 4.24), especially in the lowermost mantle. The strongest deviations occur for the fixed ϕ and η model in the region immediately above and below the 670 discontinuity. The structures of this model look quite different at a depth of 670 km than that of the preferred model (Fig. 4.25). This suggests that this region could exhibit strong tradeoffs with ϕ and η structure, as well as discontinuity structure and potentially unmodeled azimuthal anisotropy. It is also possible that this instability could be related to a distinct change in structure characteristics on either side of the 670 discontinuity (e.g. [*Gu et al.,* 2001]) which is unmodelled in our smooth radial spline parameterization. In any case, interpretation of anisotropy in the lower transition zone and uppermost lower mantle should be undertaken with a degree of caution.

Model Parameterization

For our final model, we chose to parameterize shear velocity anisotropy in terms of the Voight average isotropic velocity and ξ. However, some previous models of anisotropy, particularly in the upper mantle have preferred a parameterization with separate V_{SV} and V_{SH} models [*Ekström and Dziewonski,* 1998; *Gung et al.,* 2003]. This is a natural parameterization choice for models with a large fundamental mode surface wave dataset, as the parameterization directly mirrors the sensitivity of the dataset. However, with a dataset also containing overtone surface waves and body waves to model whole mantle structure, the division of dataset sensitivity is no longer so obvious, and damping considerations favor a model where we invert directly for the anisotropy, so as to not map errors in amplitude of velocity structure into an anisotropic signature. However, we also performed a test inversion where we inverted for V_{SV} and V_{SH} separately, starting from V_{SV} and V_{SH} models converted from our final V_S and ξ models. The damping for this inversion started from the damping used for the isotropic velocity, and was tuned to produce radially smooth V_{SV} and V_{SH} models similar in amplitude as a function of depth. This model was converted back to V_S and ξ for comparison with our preferred model.

The isotropic average of the V_{SV}/V_{SH} model was very consistent with our preferred isotropic model, with an average correlation coefficient of 0.96 as a function of depth, and no depth range having a correlation coefficient of less than 0.91 (Fig. 4.26A).

In the uppermost mantle, the anisotropic portion also showed similar stability with an average correlation coefficient of 0.96 above 400 km. The correlation over the transition zone was a little lower, averaging 0.86 between 400 and 700 km. This difference appears to be mostly in the lower transition zone, and is also partially explained by a shift in the degree 0 term (correlation improves to 0.89 when degree 0 terms are neglected), which appears to be a feature very sensitive to tradeoffs.

The lower mantle anisotropic structure is less well-correlated, particularly in the depth

range from 1200 to 2000 km. There is also a pronounced increase in the amplitude and radial roughness of recovered anisotropy in the lower mantle, when we are not directly damping ξ (Fig. 4.26B). This large amplitude signature in the mid-mantle depth ranges is hard to reconcile with studies showing negligible anisotropy in the bulk of the lower mantle. The lowermost mantle anisotropy derived from the V_{SV}/V_{SH} model has a similar degree 0 profile as the preferred model, but has higher amplitudes of 3D heterogeneity, meaning the regions of $V_{SV} > V_{SH}$ under the central and eastern Pacific are more pronounced. There is also a strong $V_{SV} > V_{SH}$ under southern and northwestern Africa.

These high structural amplitudes throughout the lower mantle seem likely to be an artefact of amplitude errors due to damping. To test this, we produced models where the norm and horizontal smoothing parameters of the V_{SV} and V_{SH} inversions were perturbed by 50% in opposite directions. This produced structural amplitude shifts that varied as a function of depth, but were generally in the range of 10% with no more than 35% from the rms amplitudes of the model discussed above. Two models were produced, one with enhanced V_{SV} amplitude, and decreased V_{SH}, and vice-versa. Correlations of V_{SV} and V_{SH} structure for the two perturbed models compared with the original model were nearly identical, with correlation coefficients between 0.98 and 0.99 averaged over the whole model. When compared with each other, the differences were slightly larger with an average correlation coefficient of 0.94 across the depth range that dipped as low as 0.85 in some regions of the lower mantle. However, when the models were converted to isotropic Vs and ξ, the differences in ξ structure were more pronounced. Comparing the ξ structure derived from the two perturbed models with the original model, the correlations averaged 0.92 over the entire depth range, with some portions of the lower mantle dropping to 0.79, and when the two perturbed models were compared with each other, the correlation dropped to 0.74 averaged over the whole mantle, with some portions at 2400 km depth dropping as low as 0.32.

This difference is most pronounced in higher degree structure above spherical harmonic degree 8, where the correlation drops to 0.85 and 0.89 for the two perturbed

models compared to the original model over the whole depth range, and down to 0.56 for the two models compared to each other, with some lower mantle regions entirely decorrelated, or slightly anti-correlated. Because these differences are so pronounced, the approach of inverting directly for ξ is preferred, which also allows us to directly apply horizontal smoothing which reduces the very uncertain shorter wavelength anisotropic structure.

4.5   Conclusions

While the isotropic velocities of SAW16B16-AN are compatible with previous tomographic models of shear velocity structure and are quite stable regardless of the anisotropic structure, the anisotropic portion of the model can be related to mantle flow patterns in several depth ranges throughout the mantle.

Specifically, a positive $\delta \ln \xi$ signature appears consistent with a region of likely horizontal flow under the lithosphere at different depths for oceans and old continents [*Gung et al.,* 2003]. A negative $\delta \ln \xi$ signature at 200-300 km depth is associated with spreading ridge segments, and the amplitude is significantly correlated with surface spreading rates for fast-spreading segments. There is also negative $\delta \ln \xi$ correlated with subducting slabs in the transition zone, although this depth range appears to be sensitive to tradeoffs with unmodelled anisotropic velocity parameters. Mid-mantle anisotropy is lower in amplitude, and its inclusion does not significantly affect the patterns obtained in other depth ranges. The structure near the CMB is dominated by a degree 0 positive $\delta \ln \xi$, likely due to horizontal flow in a mechanical boundary layer, with deviations associated with transition to the low-velocity superplumes.

Although the current dataset cannot provide us with anisotropic resolution at the same level as global isotropic velocity models, and some tradeoffs with parameters

not modelled here remain, the additional information can help constrain geodynamic models, as well as providing an opportunity to verify and guide the experimental and theoretical findings of mineral physics.
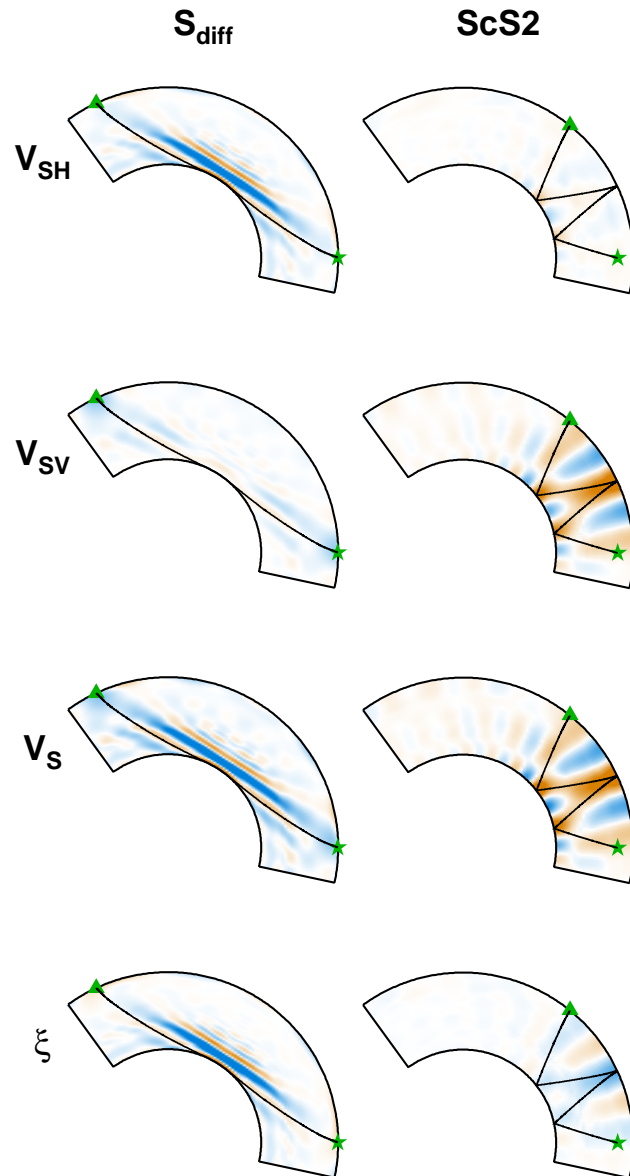
Figure 4.1: Kernels describing sensitivity to V_{SH} (top), V_{SV} (2nd row), isotropic V_S (3rd row), and ξ (bottom row) for the phases S_{diff} (left) and ScS2 (right), all recorded on the transverse component. Blue represents positive values, and red is negative, and the ξ kernels are multiplied by 3 to display on the same scale. The ray path from ray theory is shown as a black line. Note the dominance of V_{SH} sensitivity in the horizontally propagating S_{diff}, and V_{SV} in the vertical ScS2. Likewise, ξ sensitivity is the same sign as V_S for S_{diff}, but the opposite sign for ScS2.
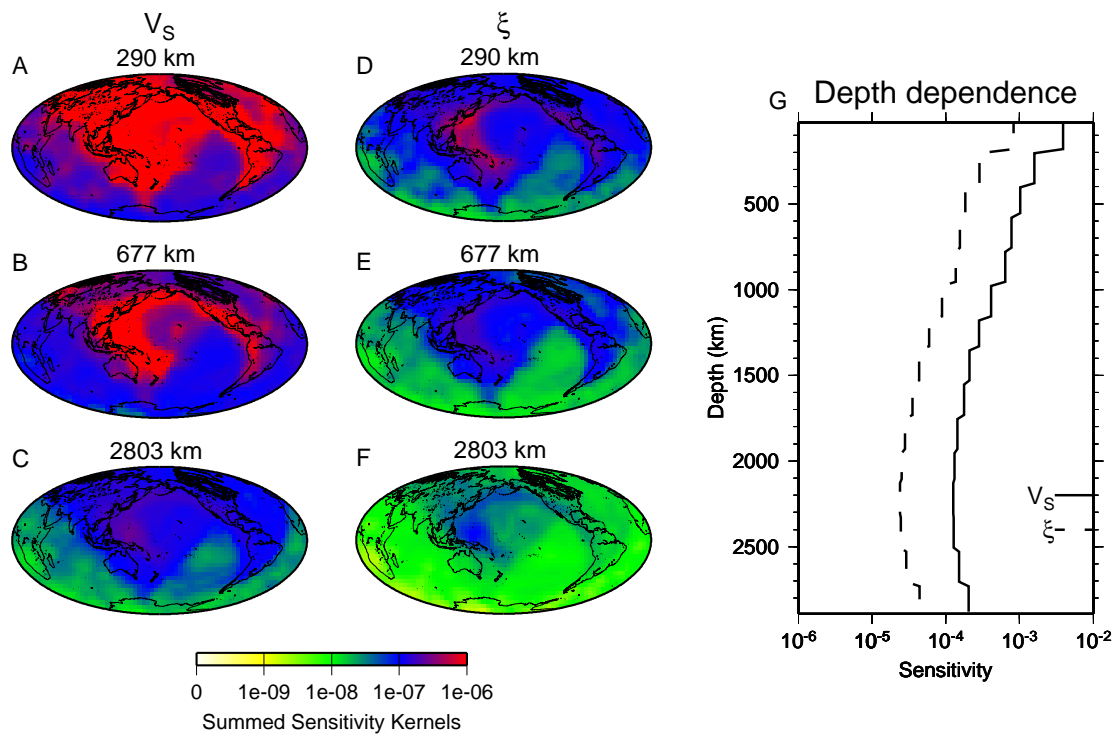
Figure 4.2: Coverage calculated from the summed NACT kernels of the inversion dataset, as discussed in section 4.2.2. The isotropic V_S and ξ coverage is shown for 200 km thick layers in the upper mantle (A,D), lower transition zone (B,E), and lowermost mantle (C,F). The total sensitivity in each 200 km layer is shown as function of depth (G).
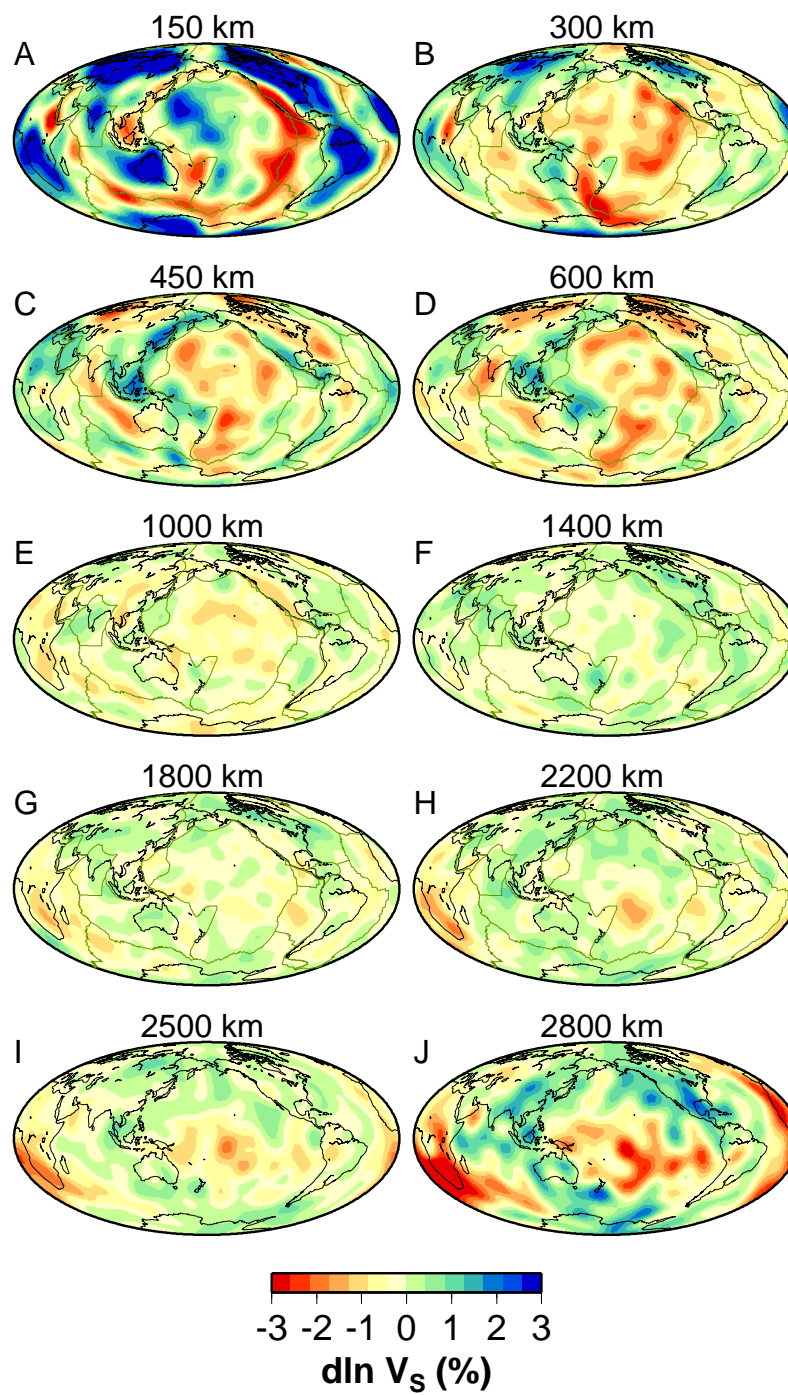
Figure 4.3: Isotropic V_S model at several depths.
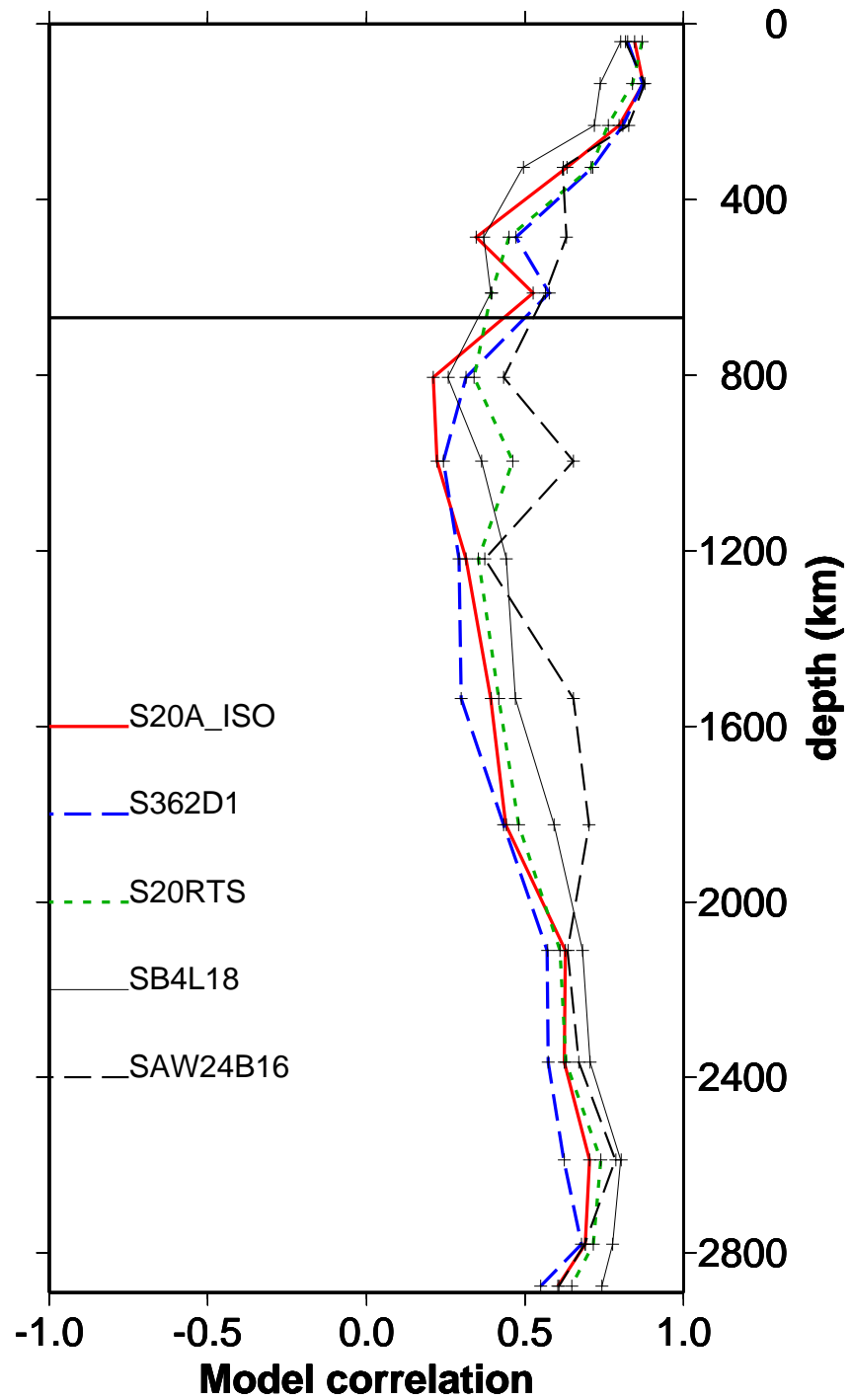
Figure 4.4: Correlation of isotropic velocity model with previously published V_S tomographic models.
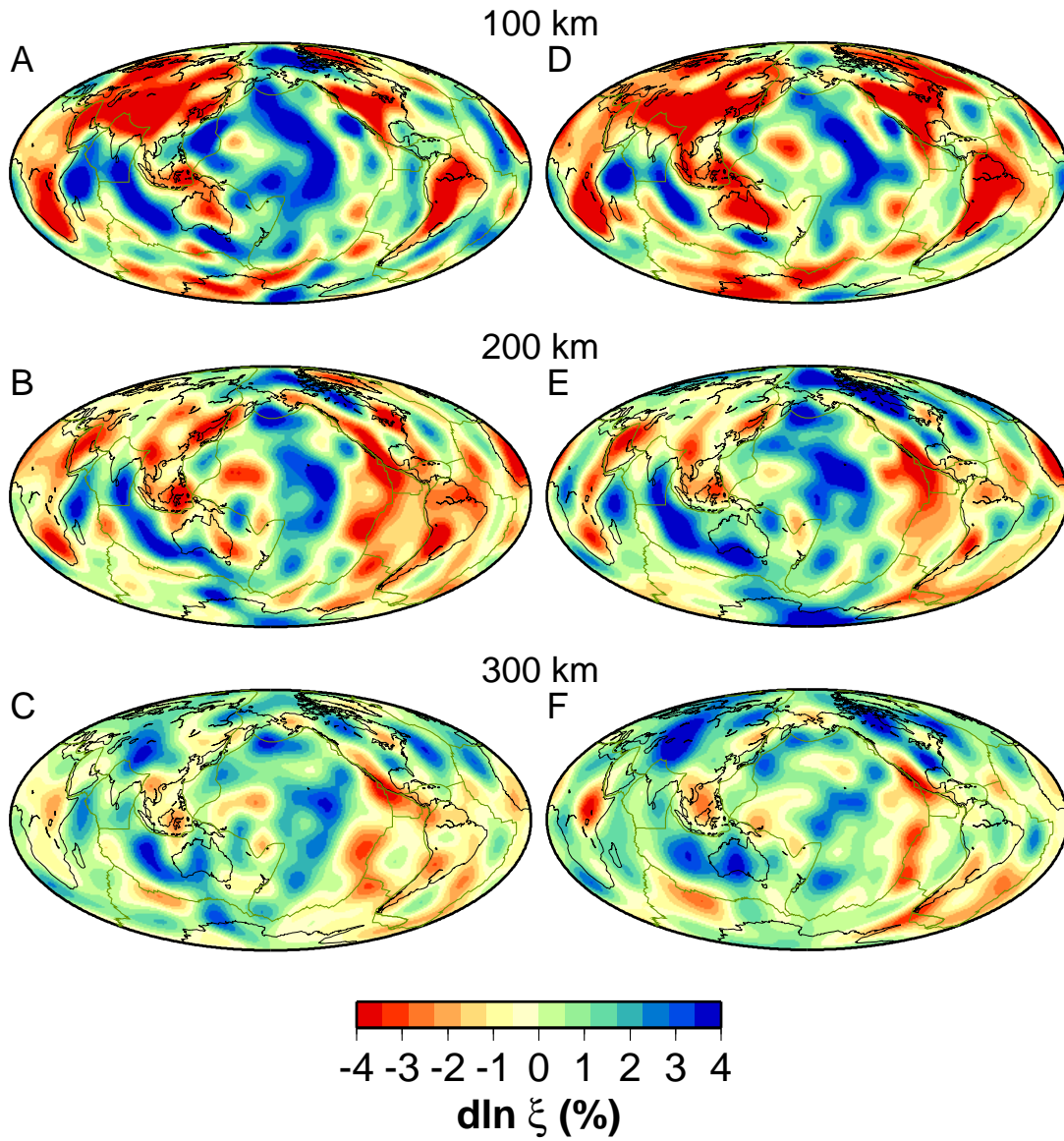
Figure 4.5: Comparison between SAW16B16-AN ξ from this paper (A-C) and the upper mantle ξ calculated from SAW16AN [*Gung et al.,* 2003] (D-F) at depths of 100 (top), 200 (middle), and 300 km (bottom).
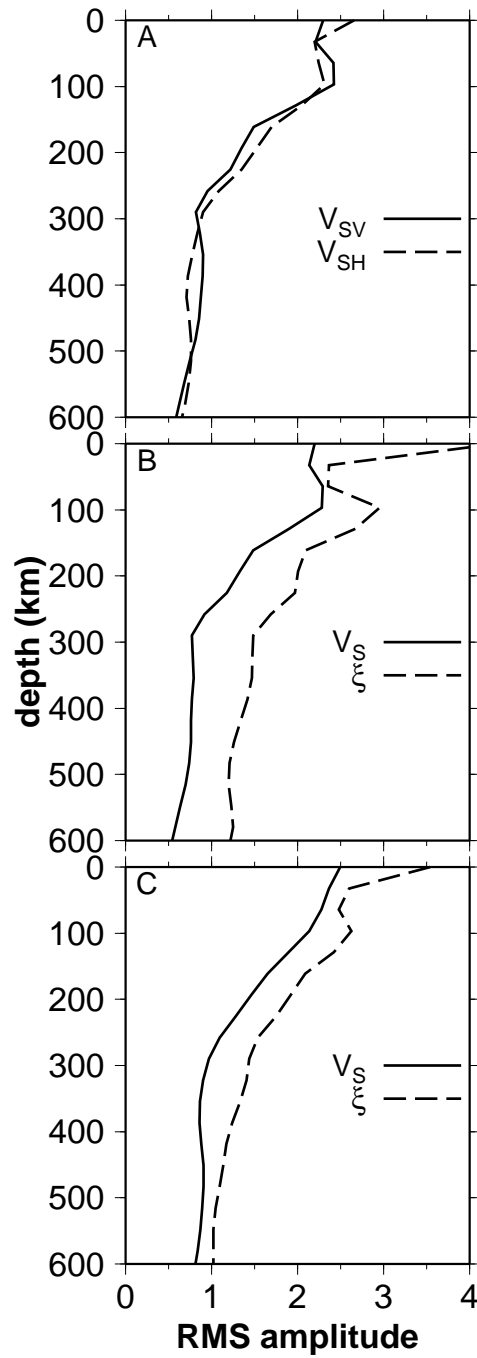
Figure 4.6: Uppermost mantle RMS amplitude profiles for SAW16AN calculated for V_{SV} and V_{SH} (A) and V_S and ξ (B), and for SAW16B16-AN V_S and ξ (C). Note the greater radial roughness of the SAW16AN profiles, particularly in ξ.
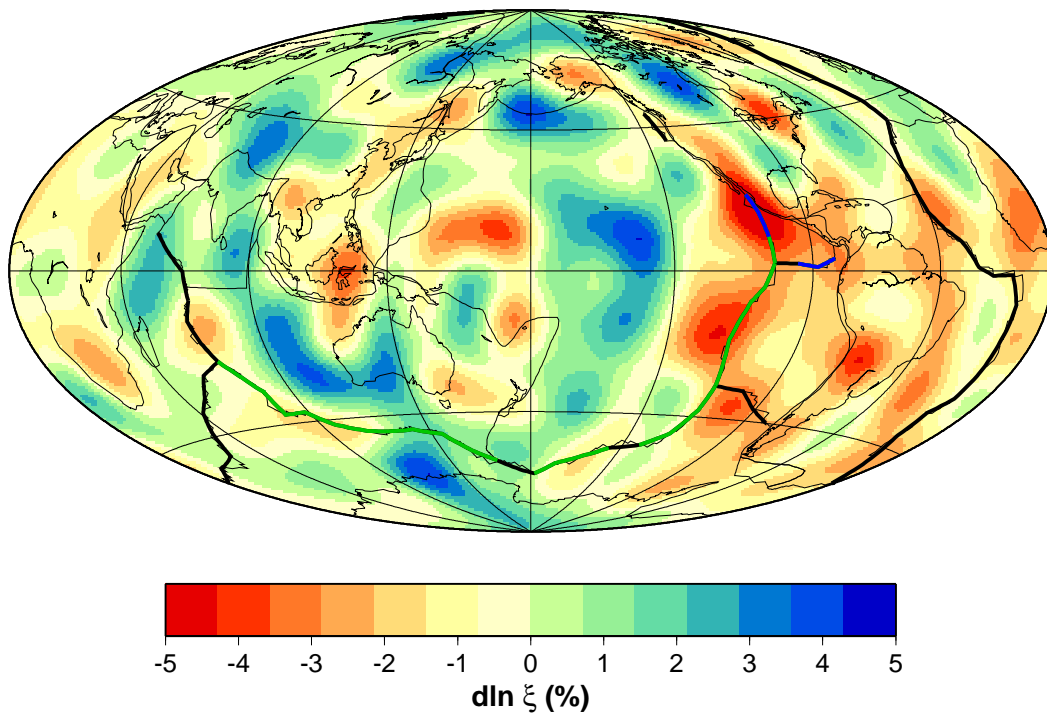
Figure 4.7: Fast-spreading ridge segments used in spreading rate calculations. Segments in blue and green represent all segments with spreading rates faster than 5 cm/yr used in Fig. 4.8. The blue segments on the northern EPR and the Cocos/Nazca boundary are also shown in Fig. 4.8, but are excluded in some regression calculations.
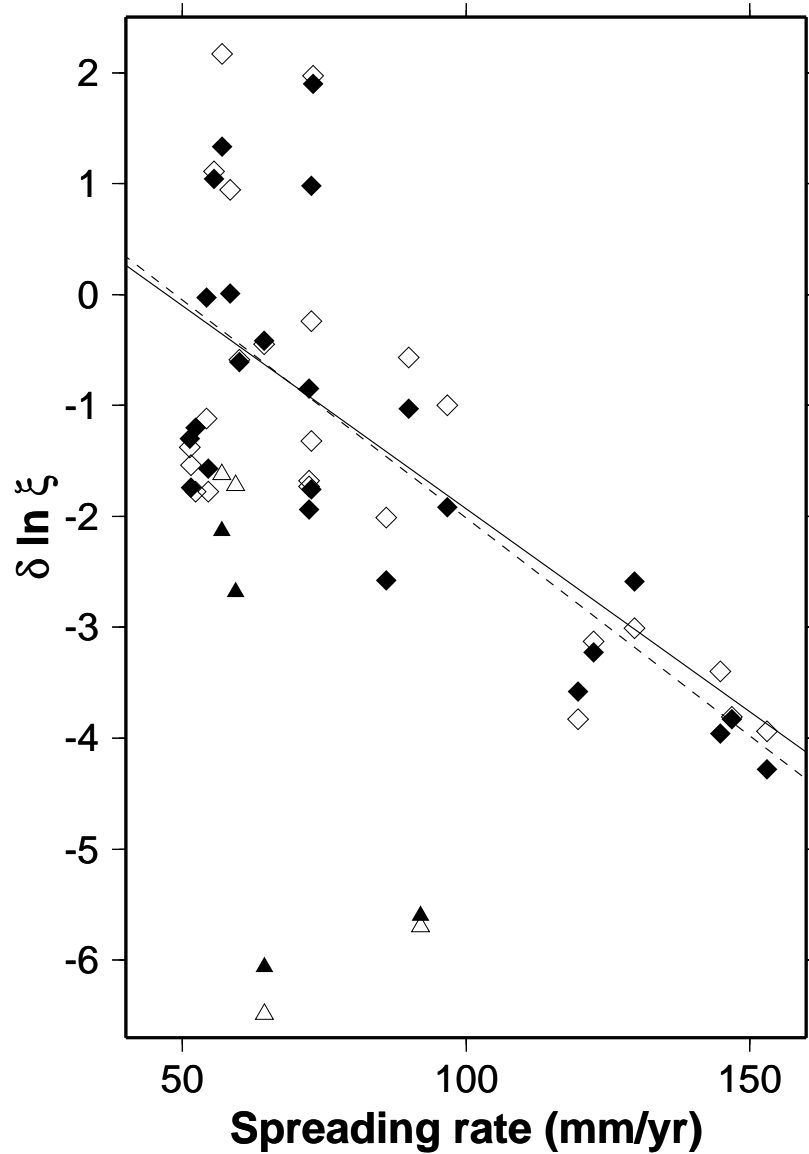
Figure 4.8: Spreading rate vs. model $\delta \ln \xi$ value for the segments shown in Fig. 4.7. Segments used for linear regression are shown with diamonds, while the 4 segments nearest subduction zones not used in the regression (shown in blue on Fig. 4.7) are triangles. Model $\delta \ln \xi$ values are shown at 200 km (open symbols) and 250 km (filled symbols), and the regression lines are shown for the data at 200 km (solid) and 250 km (dashed).
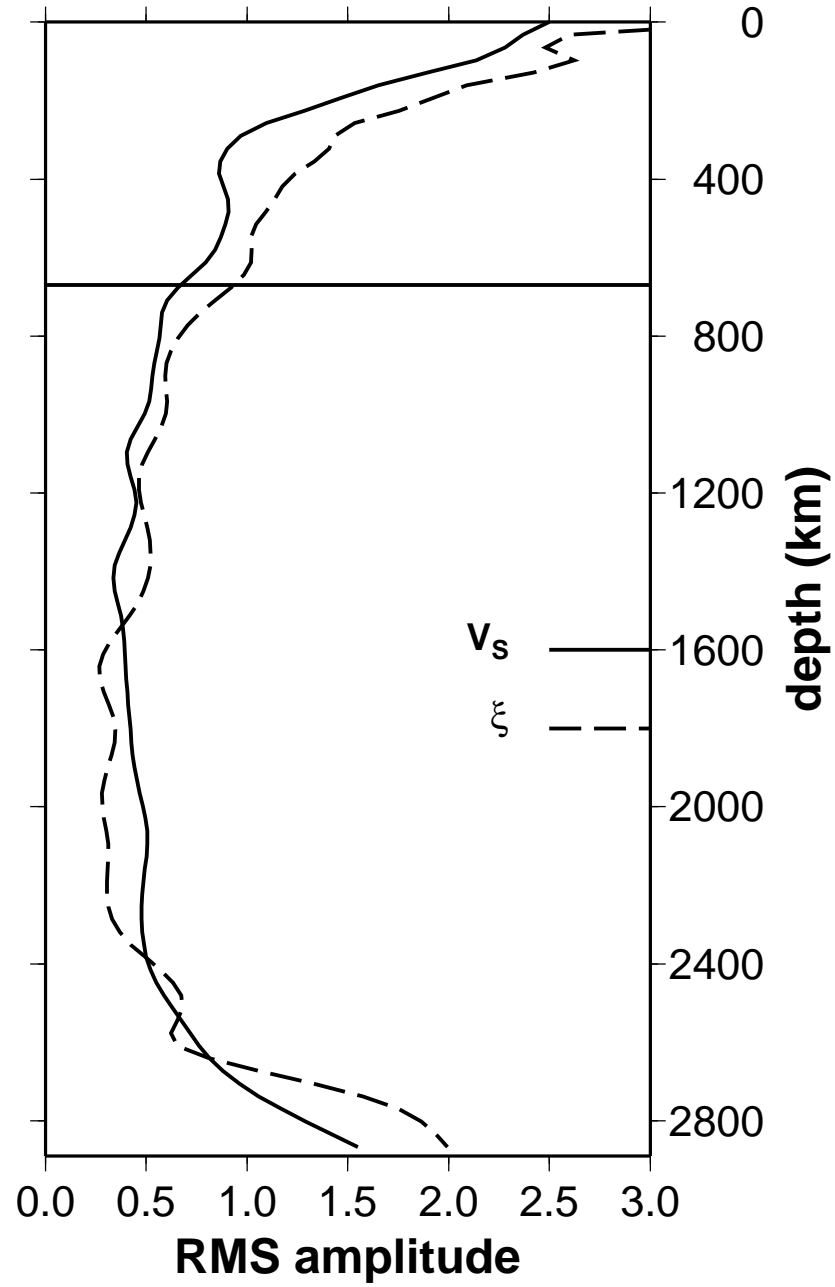
Figure 4.9: RMS amplitudes as a function of depth in SAW16B16-AN for V_S (solid) and ξ (dashed).
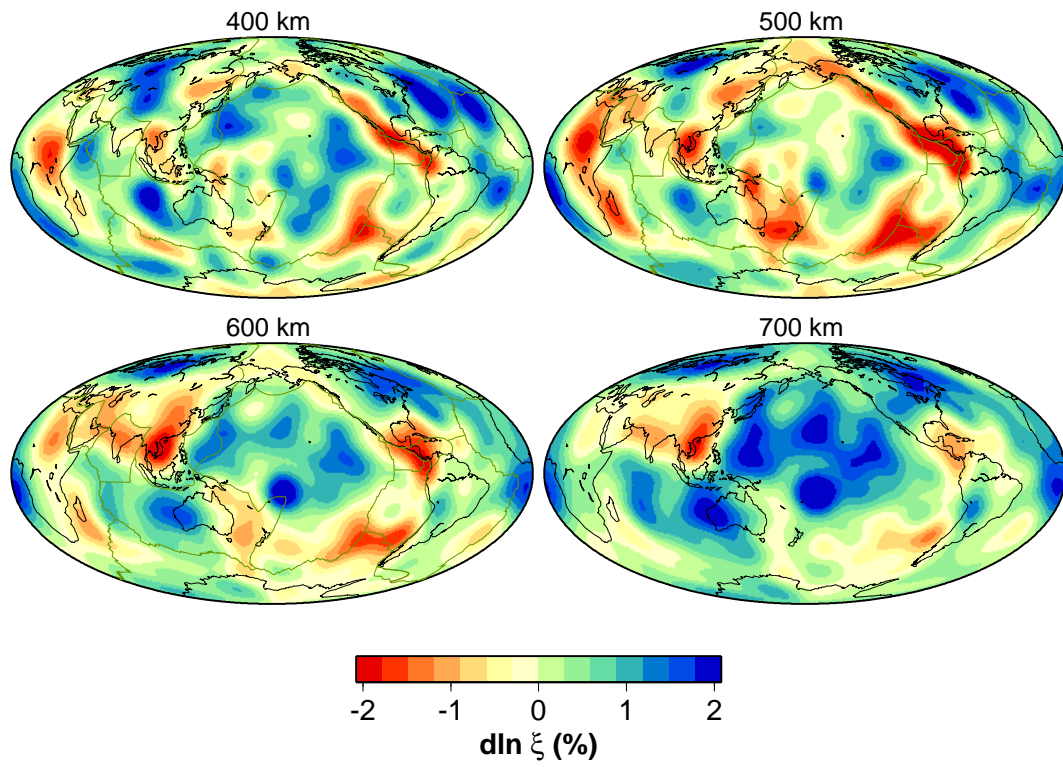
Figure 4.10: $\delta \ln \xi$ slices at 400, 500, 600, and 700 km depths.
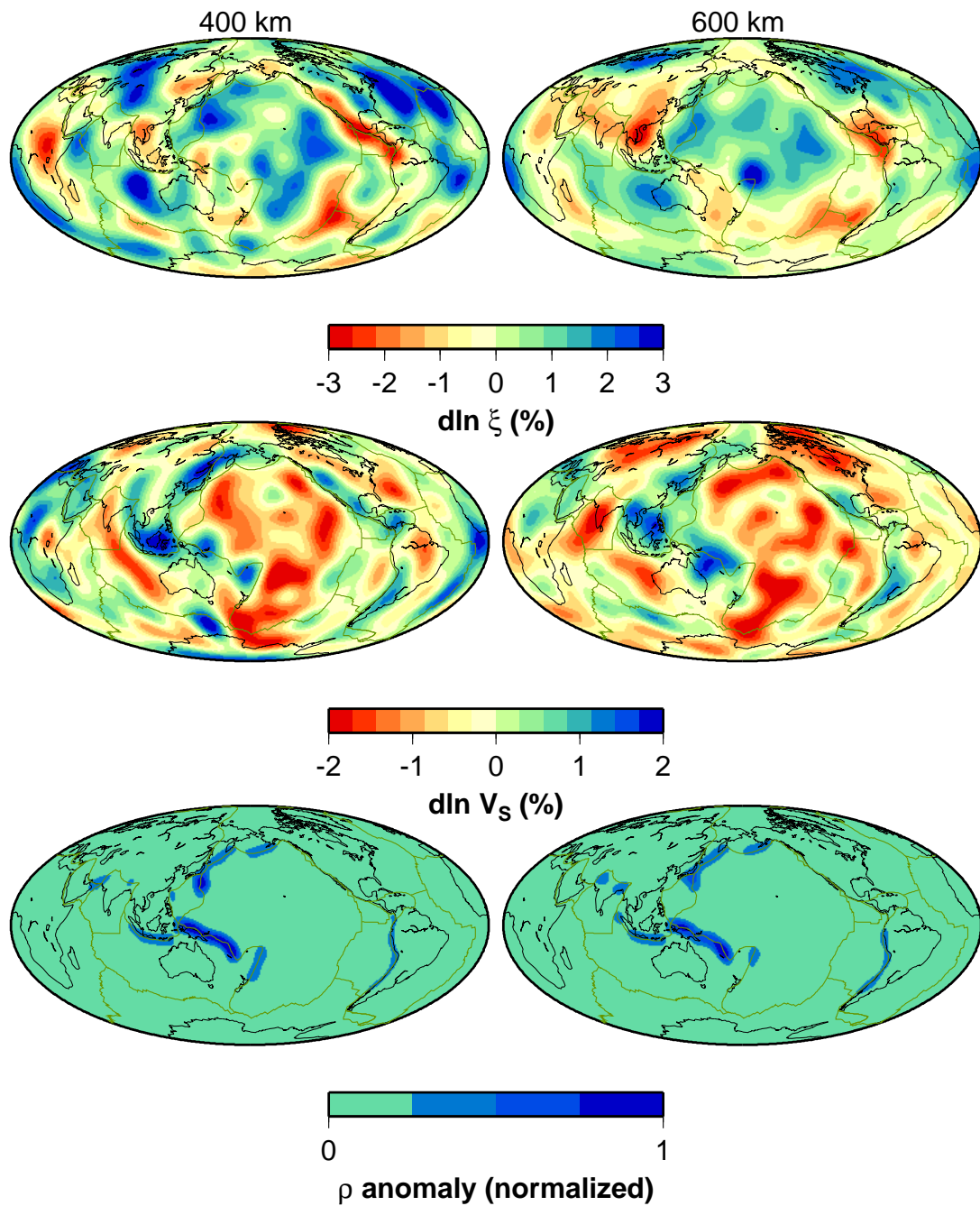
Figure 4.11: ξ (top), V_S (middle) structure at depths of 400 (left) and 600 km (right). The bottom row shows the density anomalies for 145 km thick layers centered at depths of 362.5 km (left) and 652.5 km (right) for the model of *Lithgow-Bertelloni and Richards*, [1998], normalized to the maximum density anomaly in each depth range.
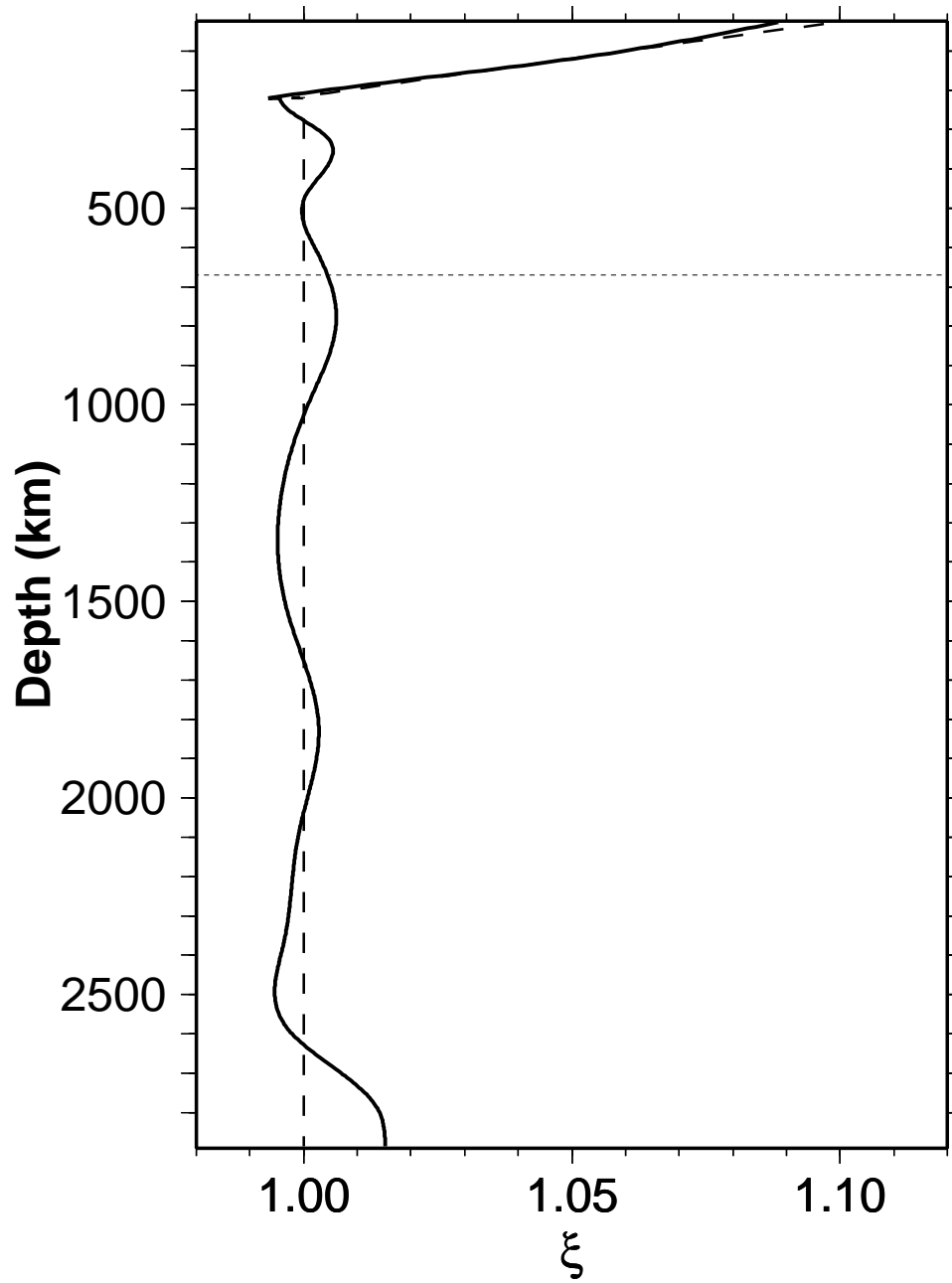
Figure 4.12: Degree 0 (radially symmetric) ξ structure as a function of depth.
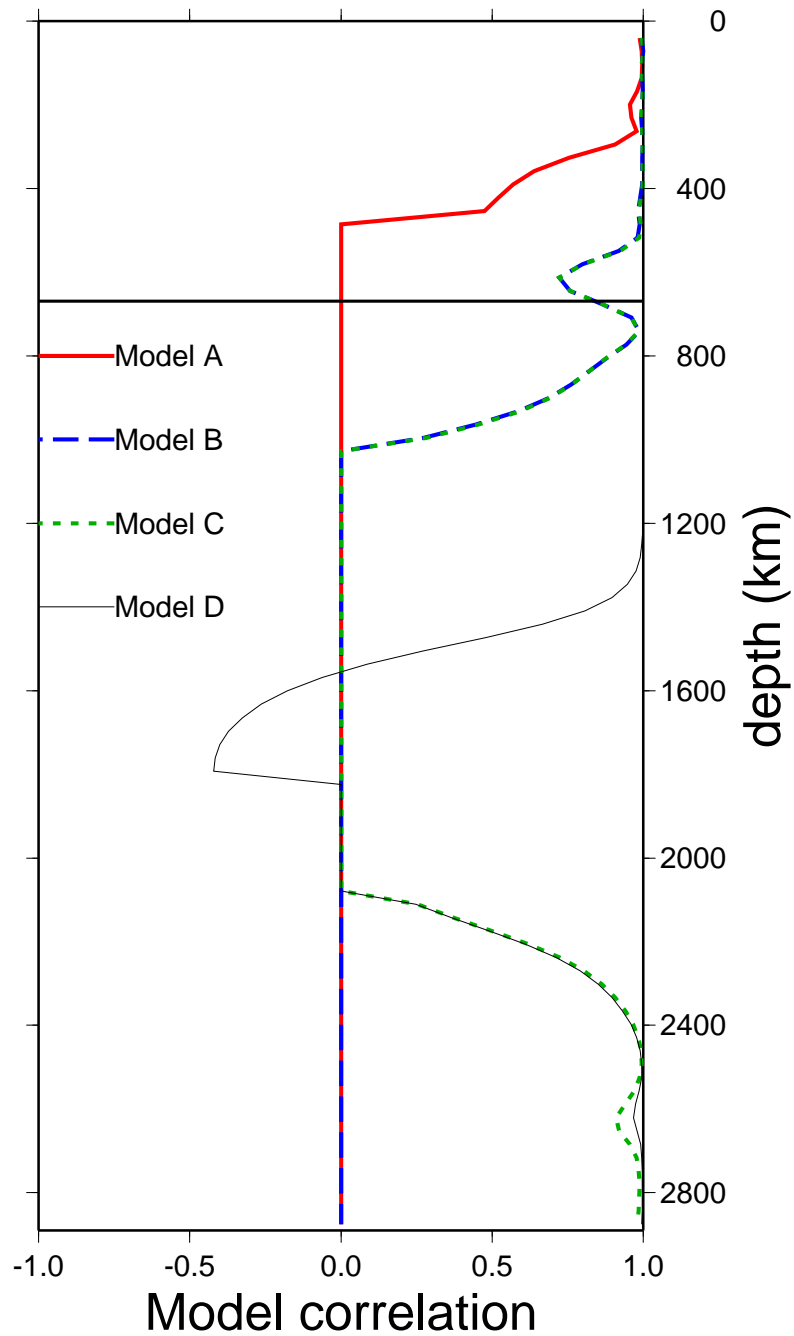
Figure 4.13: Model correlation to fully anisotropic model as a function of depth for models with anisotropy constrained to zero for splines below 200 km (Model A), below 700 km (Model B), between 700 and 2400 km (Model C), and between 1200 and 2400 km (Model D).
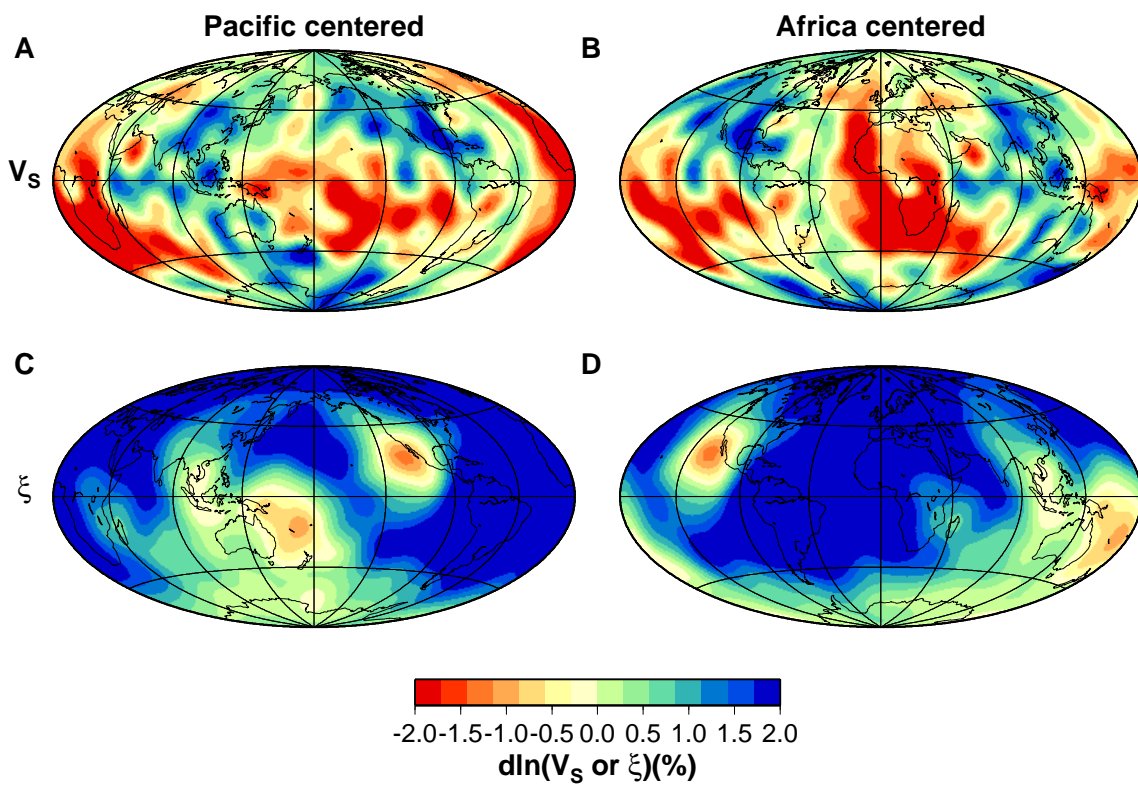
Figure 4.14: V_S (A,B) and ξ structure (C,D) at a depth of 2800 km centered under the central Pacific (A,C) and Africa (B,D)
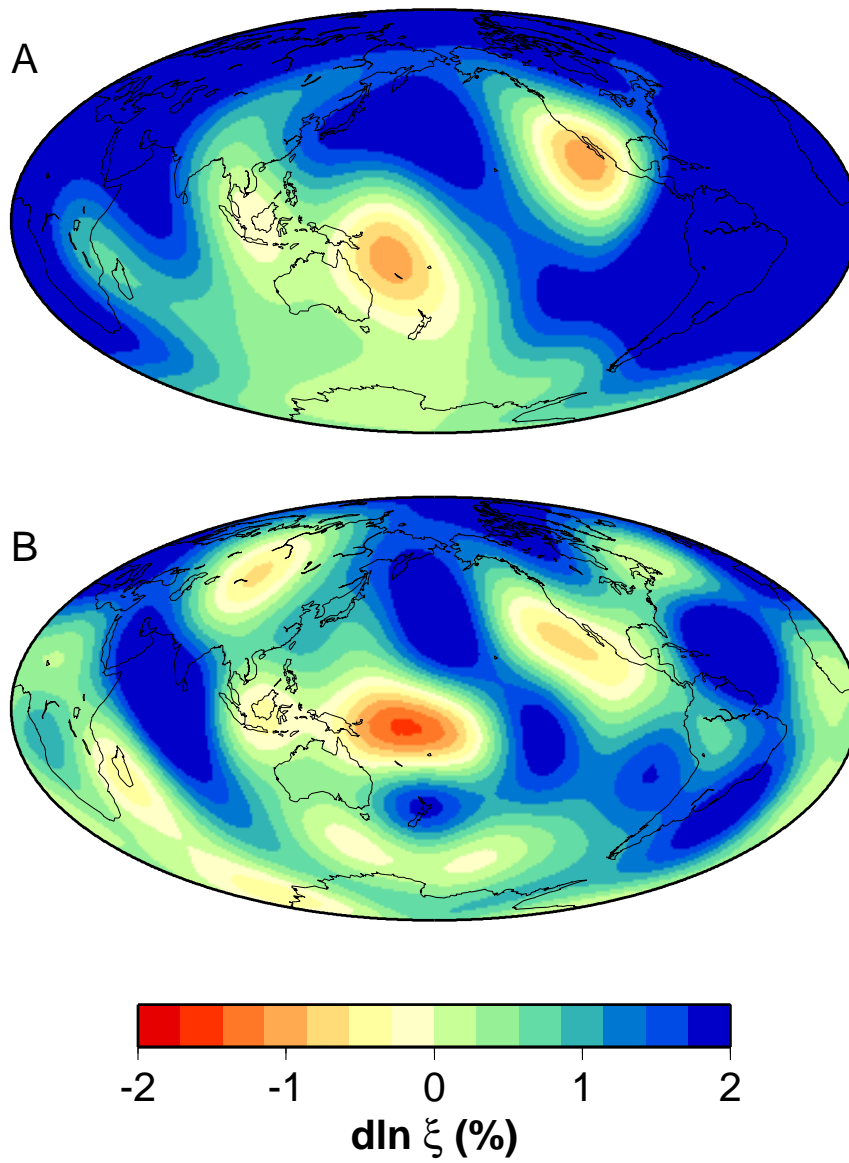
Figure 4.15: Comparison of ξ structure of SAW16B16-AN (A) and the model from *Panning and Romanowicz*, [2004] (B) both truncated at spherical harmonic degree 8.

Figure 4.16: ξ structure at 2800 km with ϕ and η scaled (A), fixed to that of *Boschi and Dziewonski*, [2000] (B) and inverted independently (C). Note the ξ starting model of the model in (C) was the model shown in (A), while the starting ϕ and η models were defined by *Boschi and Dziewonski*, [2000]. The ξ model when topography is allowed on the CMB is also shown (D).
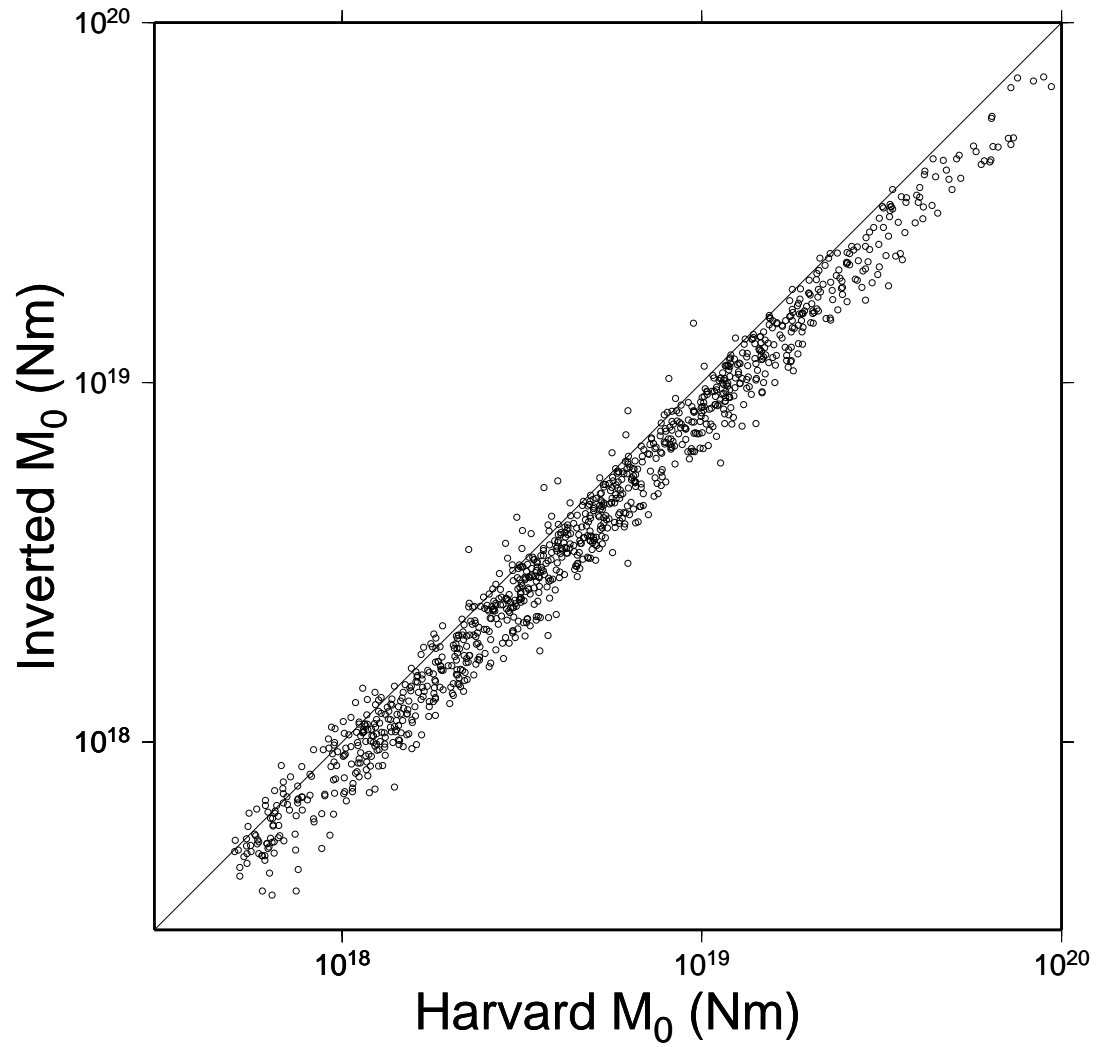
Figure 4.17: Comparison of Harvard CMT scalar seismic moment (M_0) to the M_0 from the source inversions with unconstrained moment. Solid line represents the case of no bias.
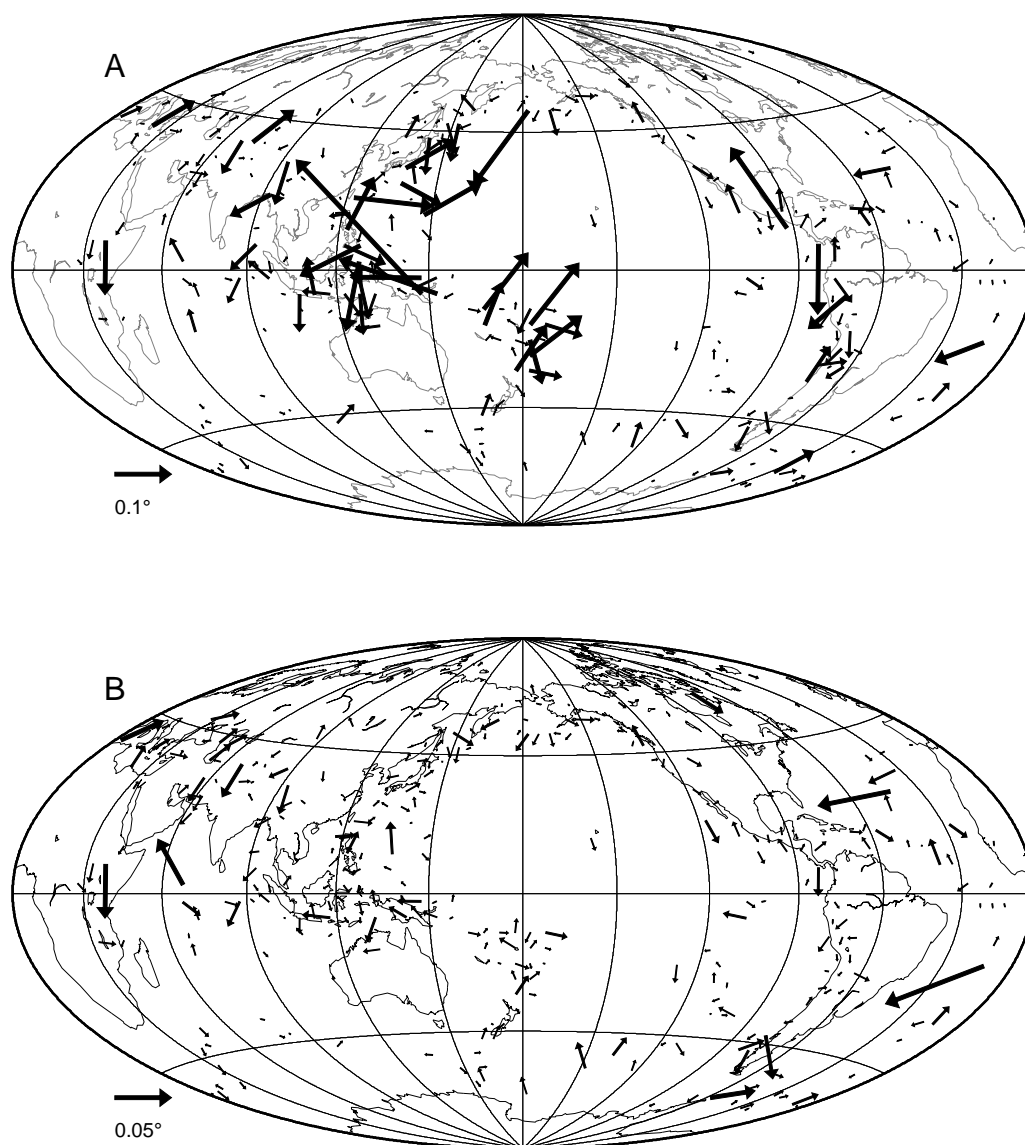
Figure 4.18: Summed vector shifts for all events in 5º by 5º cells (A), and normalized by the number of events in each cell (B). Note the vectors in (B) are at a different scale than (A).
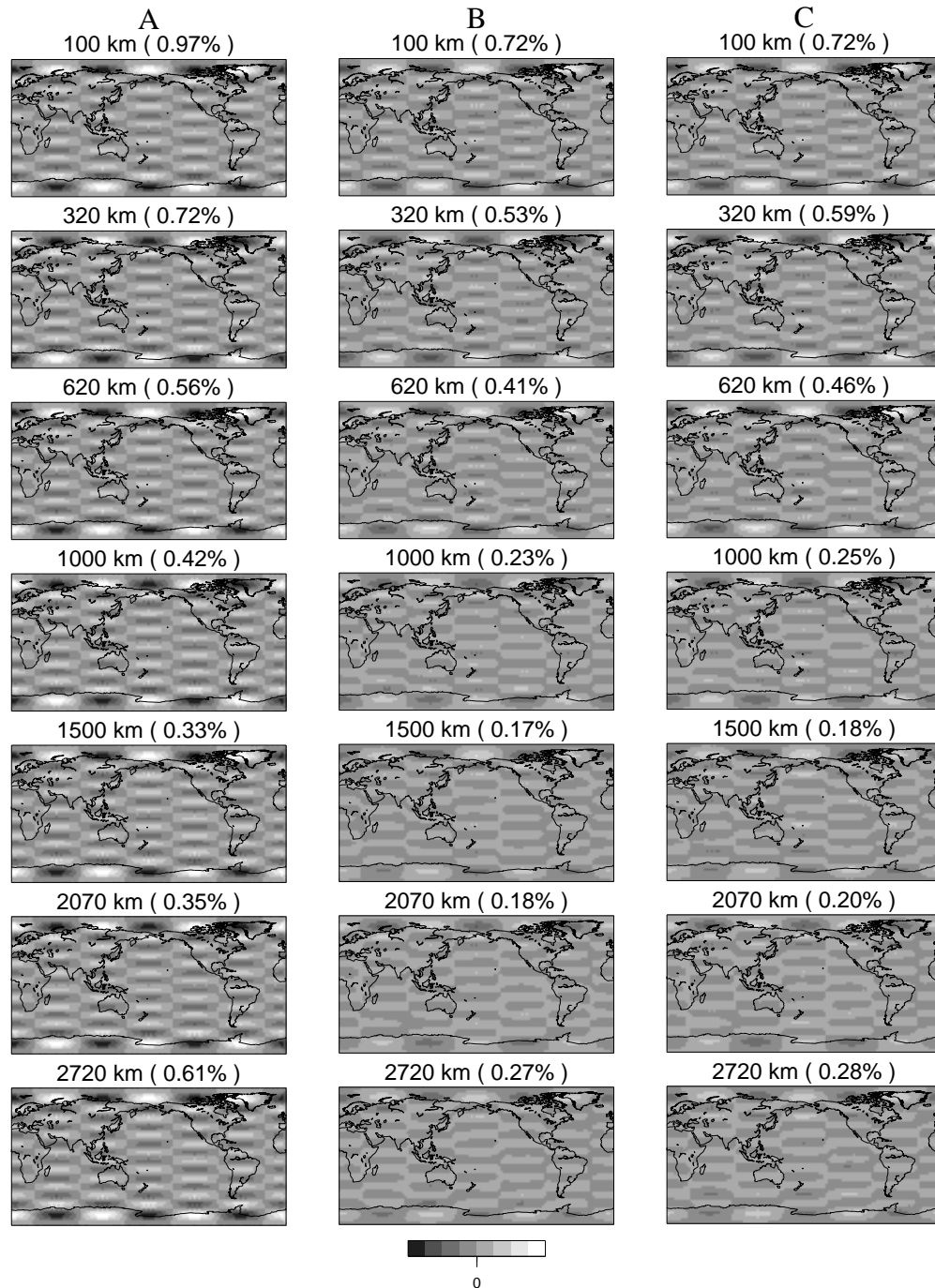
Figure 4.19: Resolution matrix checkerboard test for isotropic V_S structure. The input model (column A) produces the output structure in column B, when no anisotropic structure is included in the input, and the model in column C when anisotropic structure is also present in the input model. Numbers in parentheses are the maximum amplitude for each map. The shading is scaled to the maximum amplitude in column A for each depth.

A
100 km (0.87%)

B
100 km (0.64%)

C
100 km (0.55%)

320 km (0.57%)

320 km (0.30%)

320 km (0.35%)

620 km (0.41%)

620 km (0.15%)

620 km (0.20%)

1000 km (0.31%)

1000 km (0.11%)

1000 km (0.12%)

1500 km (0.19%)

1500 km (0.10%)

1500 km (0.11%)

2070 km (0.20%)

2070 km (0.10%)

2070 km (0.10%)

2720 km (0.35%)

2720 km (0.15%)

2720 km (0.17%)

0
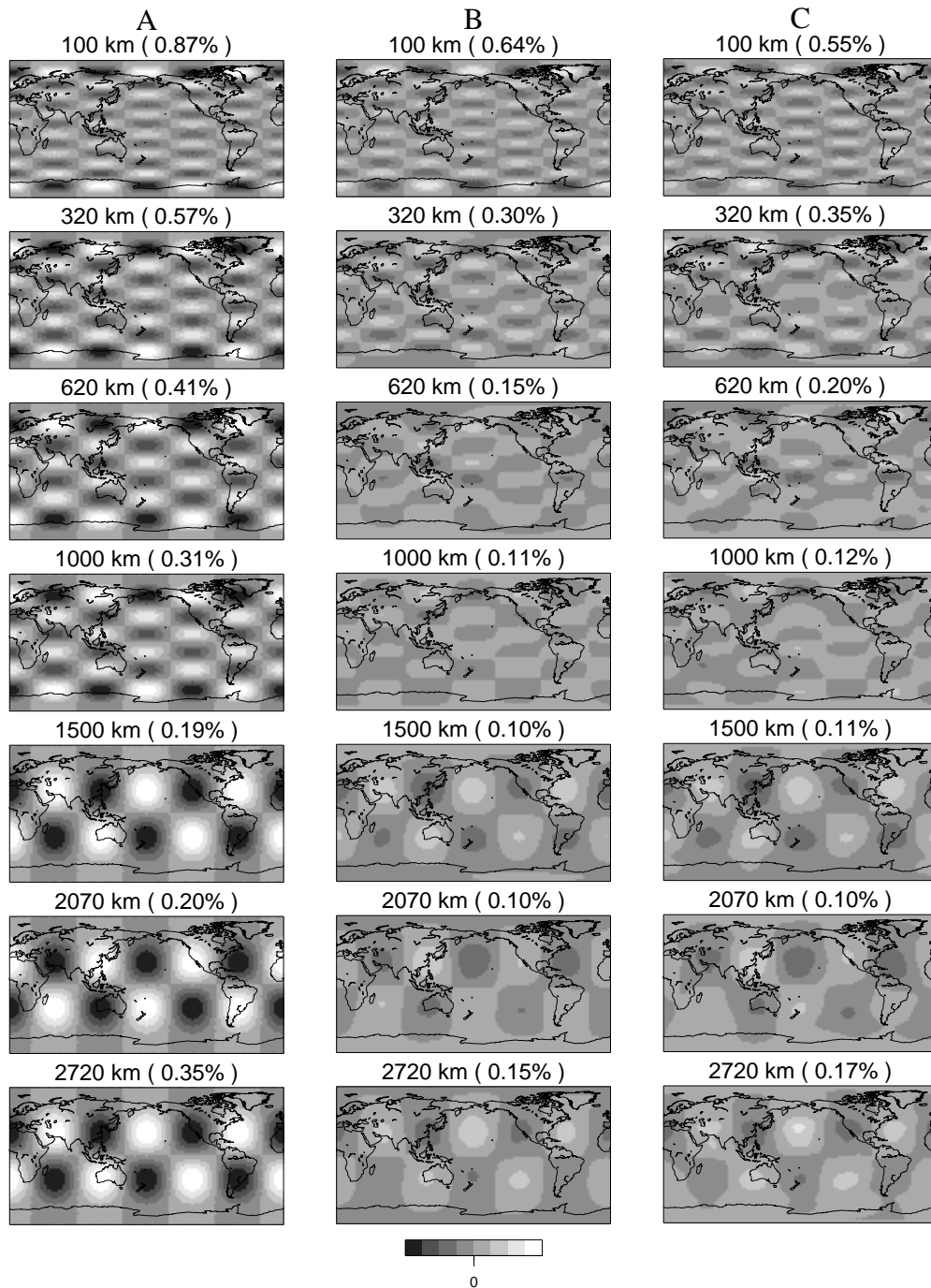
Figure 4.20: Same as figure 4.19 for ξ structure. The input model (column A) does not include isotropic structure for the output in column B, but does for column C.
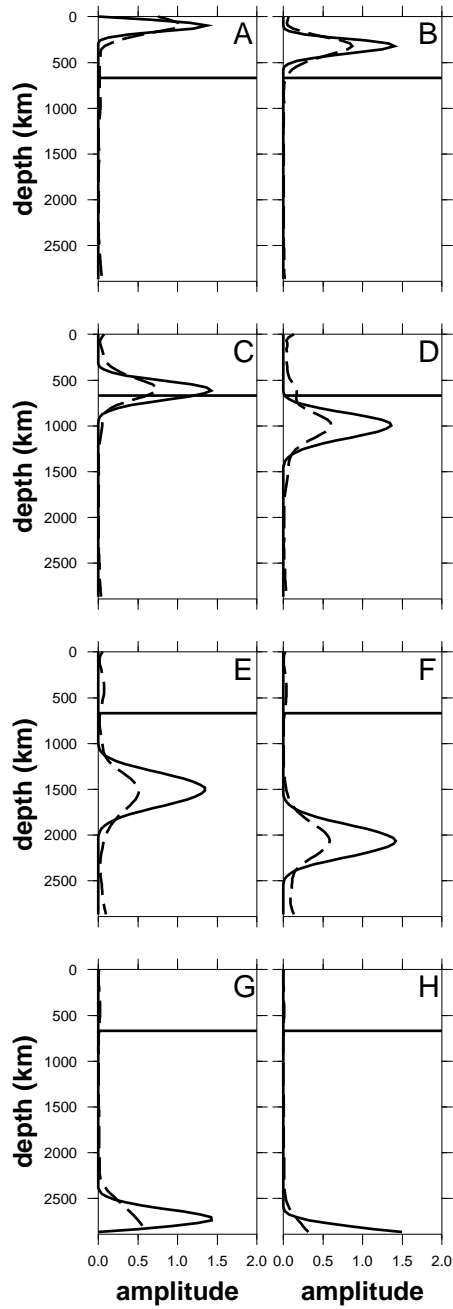
Figure 4.21: Resolution matrix test where input ξ structure is constrained to a single radial spline. Input amplitude (solid line) and output (dashed line) is shown for splines with peak amplitudes at 121 (A), 321 (B), 621 (C), 996 (D), 1521 (E), 2096 (F) and 2771 km depth (G), as well as at the CMB (H).
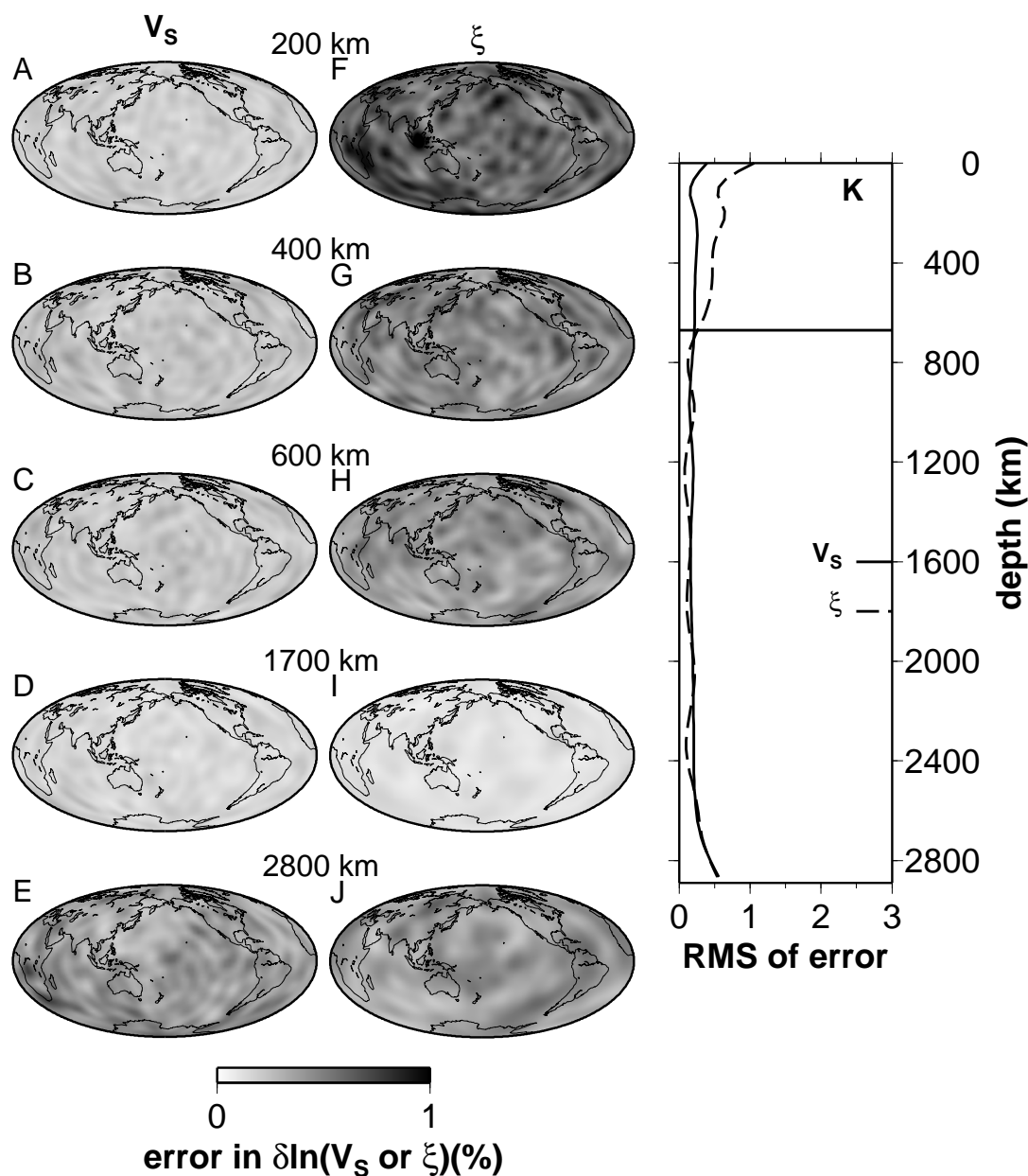
Figure 4.22: Standard error of model values calculated using a bootstrap algorithm at several depths for V_S (A-E) and ξ (F-J). The RMS amplitude of the standard error as a function of depth (K) is also shown for V_S (solid) and ξ (dashed), and can be compared with amplitudes of the model structure shown in Figure 4.9. Note that the errors are quoted in percent perturbation from the reference model, not as percentages of the final model amplitudes.
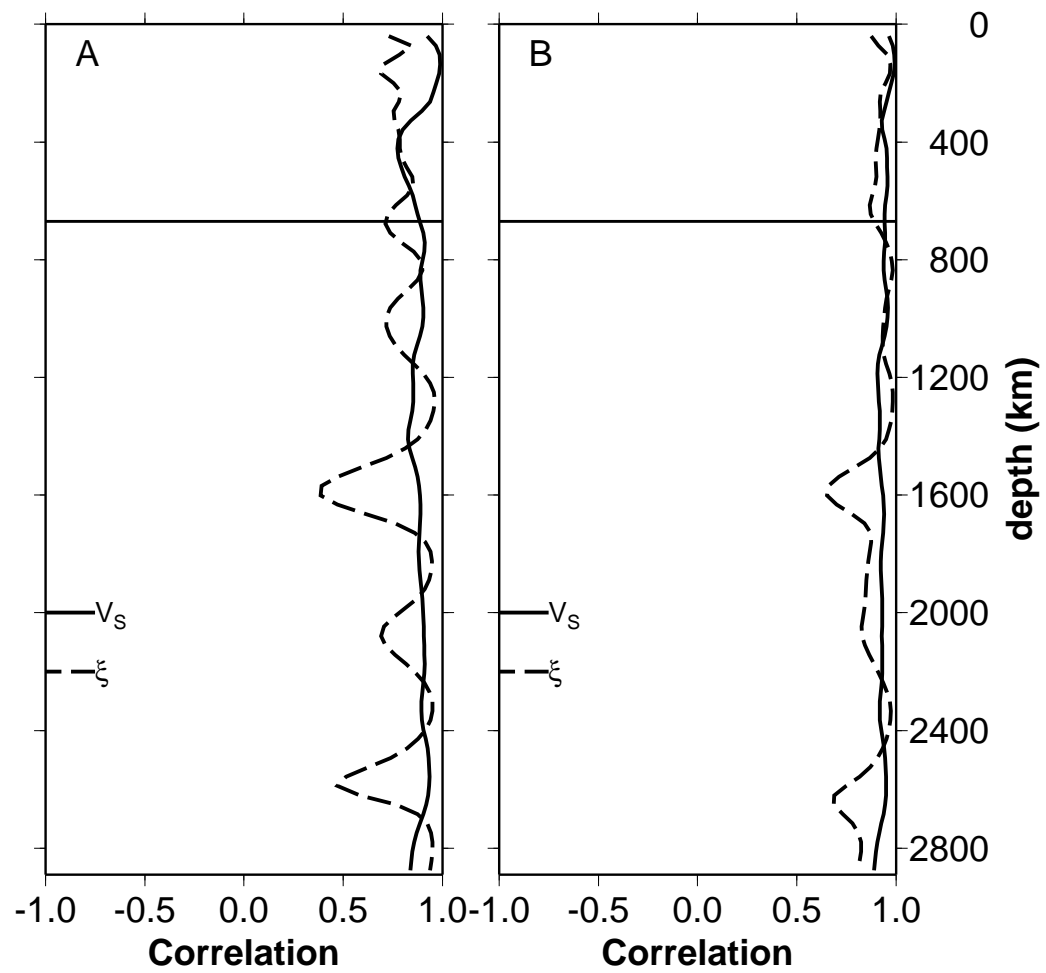
Figure 4.23: Correlation of V_S (solid) and ξ (dashed) of the final model with the model including isotropic crustal perturbations (A) and topography on the 670 discontinuity and core-mantle boundary (B).
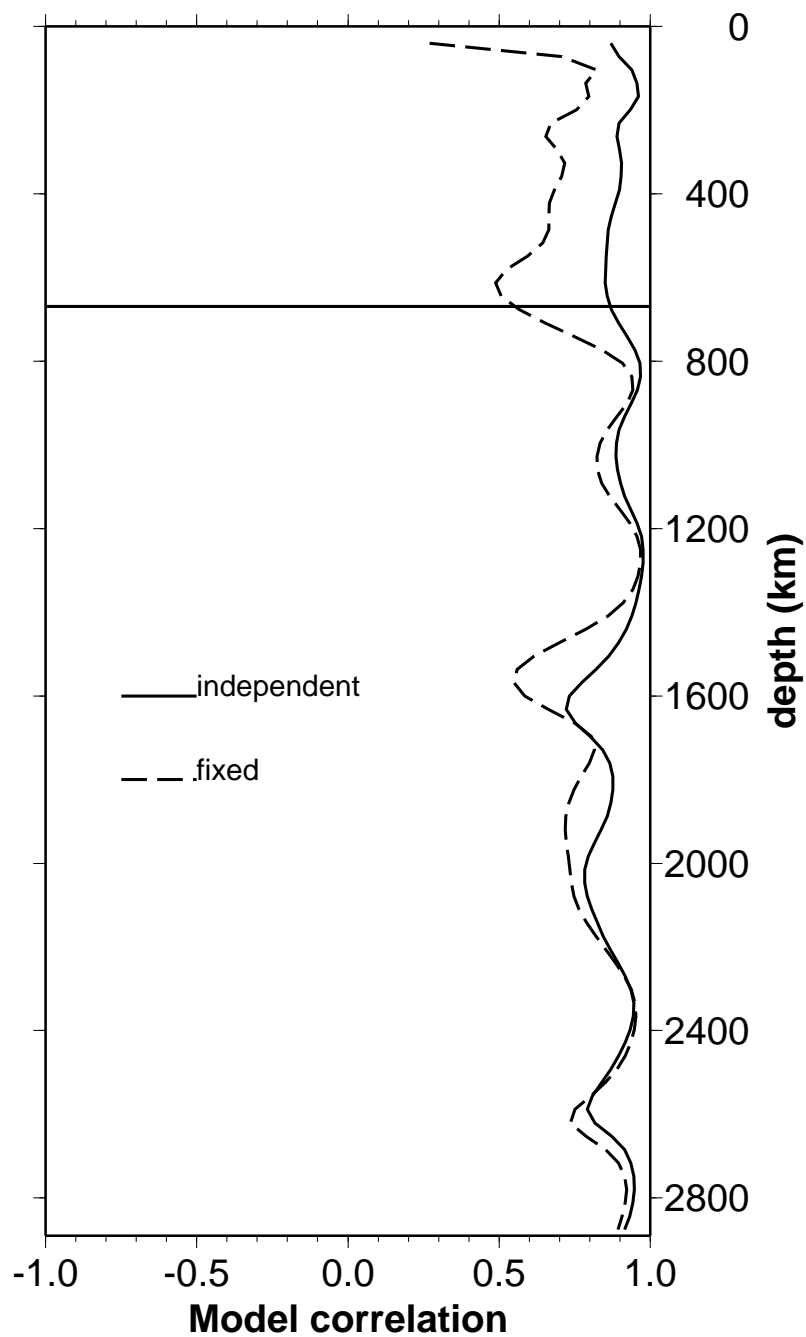
Figure 4.24: Correlation with the final ξ model as function of depth for a model with ϕ and η structure fixed (solid), and a model with ϕ and η treated as independent parameters in the inversion (dashed). Both models are inverted from data not including source parameters discussed in section 4.3.6. The starting model for the fixed inversion had no ξ structure. For the independent inversion, the starting model included the ξ structure used for the CMT inversions, as well as a starting ϕ and η model.
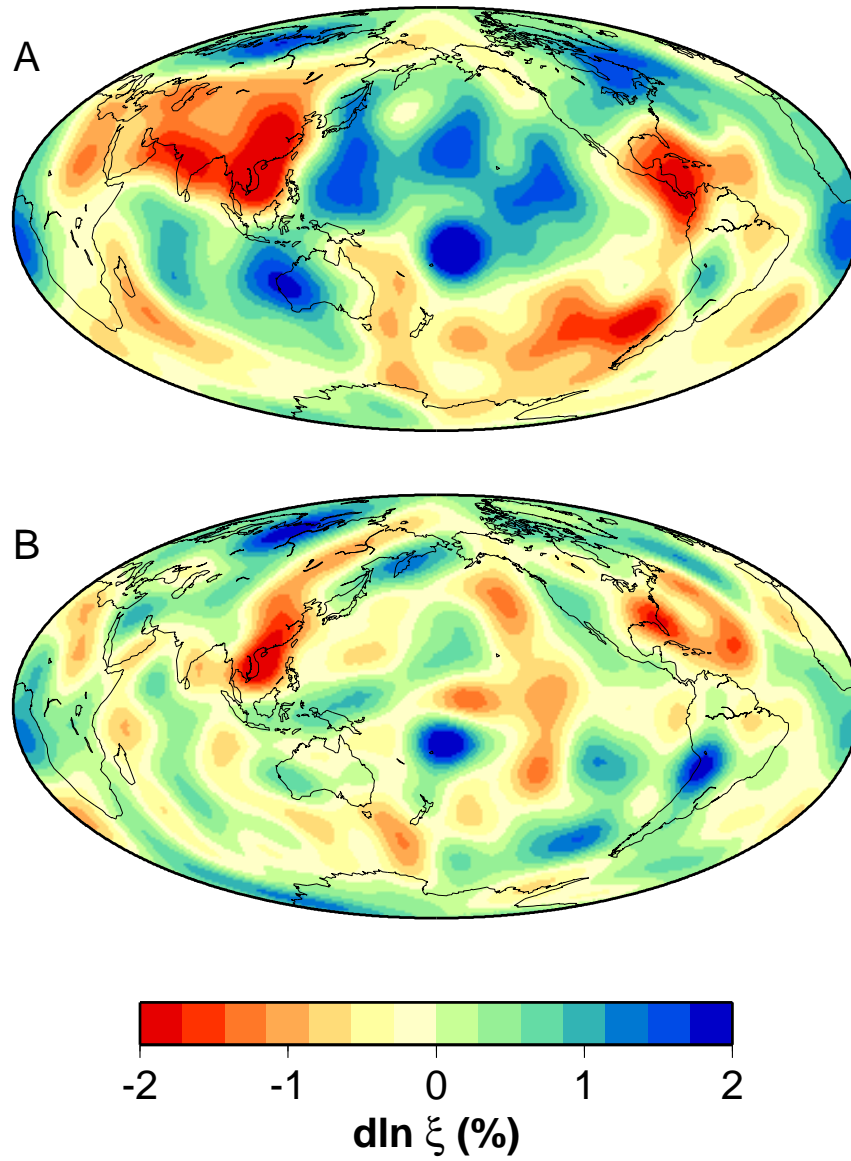
Figure 4.25: Comparison of ξ structure at 670 km depth in the final model (A), and the model with fixed ϕ and η structure (B). Note the strong differences under the Pacific and Indian Oceans, as well as under North and South America.
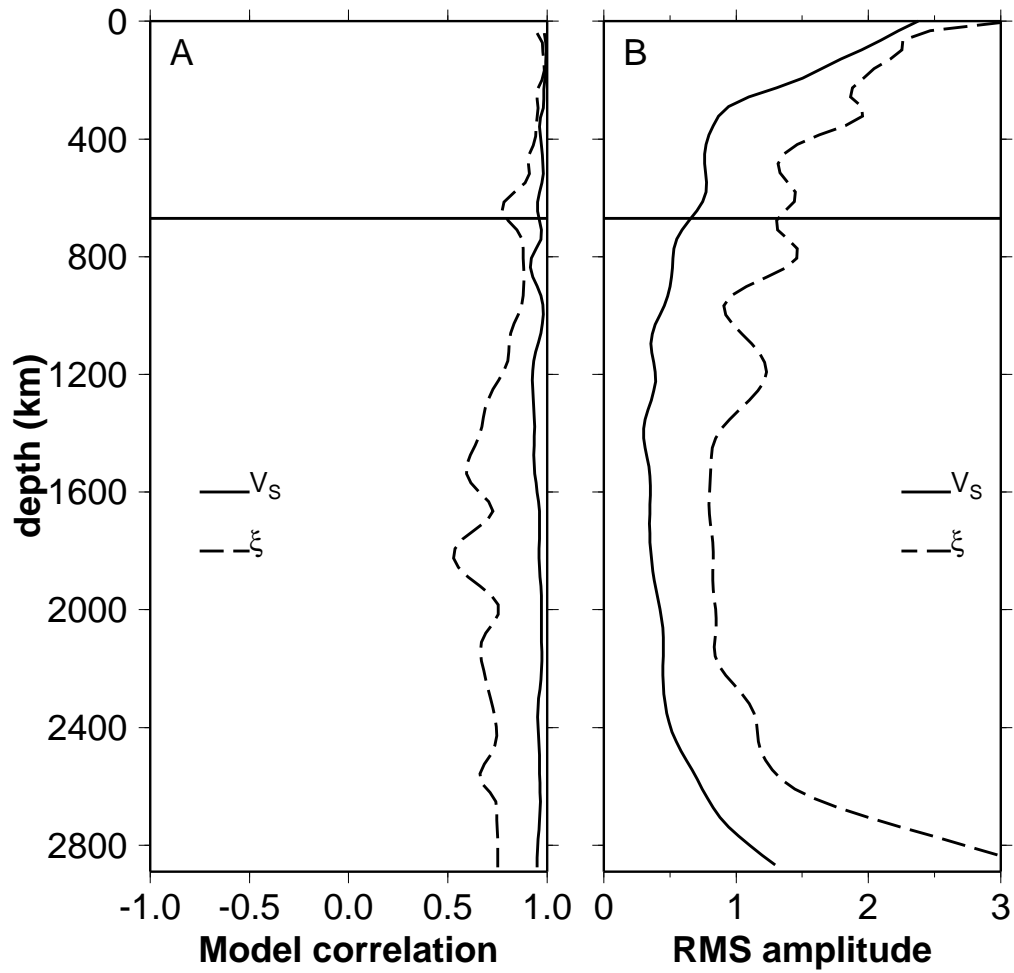
Figure 4.26: Correlation to SAW16B16-AN as a function of depth (A) and RMS profiles (B) for V_S (solid) and ξ (dashed) calculated from an inversion for V_{SV} and V_{SH}. Compare to the rms profiles for the preferred model shown in figure 4.9.

Chapter 5

Near-source velocity structure and isotropic moment tensors: a case study of the Long Valley Caldera

This chapter has been published in *Geophysical Research Letters* [*Panning et al.,* 2001] under the title:'Near-source velocity structure and isotropic moment tensors: a case study of the Long Valley Caldera.'

Summary

The effect of near-source velocity structure on the recovery of the isotropic component in moment tensor inversions is explored using a finite-difference method. Synthetic data generated using a 3D Long Valley Caldera (LVC) velocity model (V_p +/- 20%) were inverted for the full moment tensor using a standard linear time-domain scheme utilizing Green's functions calculated from 1D models. While inversions of synthetic data with input isotropic components recovered isotropic components with 95% sig-

nificance according to an F-test relative to deviatoric inversions (isotropic component constrained to zero), inversions of synthetic data with no input isotropic component recovered only nominal isotropic components with less than 75% significance. This study demonstrates that near-source structure does not appear to falsely produce significant isotropic components of moment tensor inversions in the passband typically employed by regional inversion methods.

5.1 Introduction

There has been disagreement about the source processes of earthquakes in and around Long Valley Caldera (LVC) for over twenty years. After the Wheeler Crest earthquake on October 4, 1978, and a swarm of earthquakes including four magnitude 6 earthquakes in 1980, there was much debate concerning the observed non-double-couple (NDC) component of several of these events [*Julian and Sipkin,* 1985; *Wallace,* 1985]. More recently, another earthquake swarm in late 1997 and early 1998 consisted of several earthquakes above magnitude 4 with significant NDC components [*Dreger et al.,* 2000] (Figure 5.1).

With the data available in the 1980's, debate focused on the significance of observed compensated-linear-vector-dipole (CLVD) component [*Knopoff and Randall,* 1970] for three of the earthquakes. It is agreed that the radiation of these events departs significantly from that of a double-couple, but the underlying mechanism is not understood. Three hypotheses for the mechanisms behind the anomalous moment tensor have been proposed. The first is that complication results from complexity in the rupture process, where rupture on two differently oriented double-couple (DC) fault planes sum to create a NDC component [*Wallace,* 1985]. Second, it has been suggested that structural complexity, which is very pronounced in the LVC due to magmatic resurgence, may lead to propagation anomalies which potentially bias the
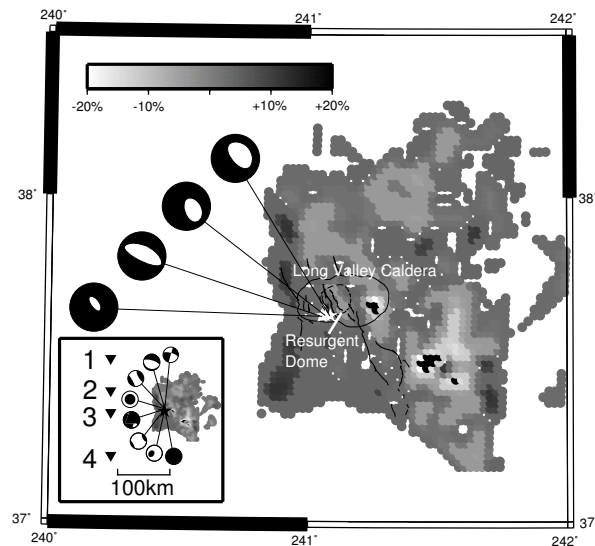
Figure 5.1: Map of the LVC showing the variation in V_p for a 6 km depth slice in the H. Benz tomographic model [written communication, 1999]. The white background represents areas with no deviation from the reference model. Moment tensor inversions for 4 events in 1997 are shown [*Dreger et al.,* 2000]. Inset: configuration for the finite-difference simulations. The source is the star, and the triangles are the receivers used in the moment tensor inversions. The mechanisms shown are input mechanisms 1-2, 3-5, 6-7, 8, 9, 10, 11, and 12 used in the finite-difference simulations (Table 5.1).

inversion [*Wallace,* 1985]. Third is the proposal that the NDC component is caused by tensile fracturing related to magmatic or hydrothermal fluid intrusion rather than tectonic shear faulting, which would lead to a predominantly CLVD moment tensor [*Julian,* 1983]. With the high quality digital broadband data available for the events in the 1997 swarm, *Dreger et al.* [2000] argued the anomalous moment tensors for this swarm contained not only CLVD components, but also isotropic components implying significant volumetric expansion during the source process further suggesting fluid-related fracture. This study attempts to quantitatively test the second hypothesis and determine possible biases in the recovery of NDC and isotropic components due to unmodeled 3D wave propagation in the case of severe near-source heterogeneity.

5.2 Methodology

To model the effects of the LVC structure on the moment tensor inversion, we utilized an elastic finite-difference code, E3D [*Larsen and Schulz,* 1995], to calculate synthetic seismograms for a 3D velocity and density model. This code solves for the velocity-stress field with a 4th order staggered grid finite-difference scheme that is 2nd order accurate in time. For the model of LVC structure, we embedded a local/teleseismic P-wave tomography model of the region from H. Benz [written communication, 1999] in an averaged flat layer model extending out to fill an area 326 km on a side and 89 km in depth with 1 km grid spacing. S-wave structure was derived by assuming a Poisson's ratio of 0.25 and density was specified following *Birch,* [1961]. The model has severe (+/- 20%) velocity heterogeneity in the LVC.

Point sources with known moment tensors were located in this model at varying depths, and synthetic seismograms were calculated at 4 stations (Figure 5.1, inset). Although due to computational concerns the distance range for the stations in the simulations was limited to 100 to 150 km rather than the 50 to 300 km to the sta-
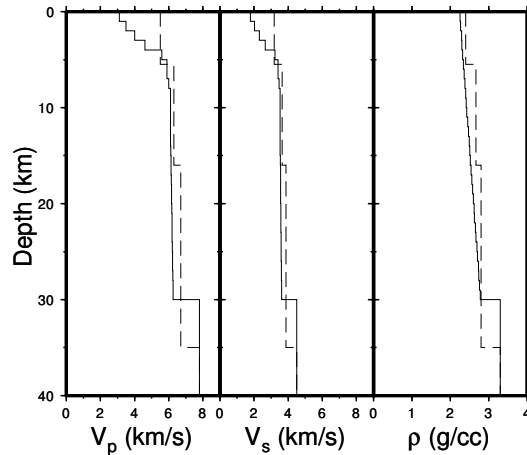
Figure 5.2: Comparison of V_p, V_s, and ρ for the AveTomo (solid) and the SoCal model (dashed).

tions used in the inversion for the 1997 events [*Dreger et al.,* 2000], the azimuthal distribution is similar.

Given the lowest velocity in the model of 1.59 km/s, we simulated synthetic velocity data to a maximum frequency of 0.159 Hz for 10 grid points per minimum wavelength. The synthetic data was then created by integrating to displacement and filtering between 0.02 and 0.05 Hz. Within the frequency range of the moment tensor inversions, grid dispersion from the finite difference method is negligible [*Moczo et al.,* 2000]. Inversion kernels (Green's functions) were calculated using a frequency-wavenumber integration (FKI) technique for a simple layered velocity model. Two layered models were considered. The first was SoCal, a model shown to be effective in describing regional wave propagation in southern California and the Sierra Nevada region [*Dreger and Helmberger,* 1993; *Pasyanos et al.,* 1996], and the second (AveTomo) was determined by averaging the velocities in each 1 km thick layer of the tomographic model (Figure 5.2). Green's functions from both models were used to invert for deviatoric and complete moment tensors using the method employed by *Dreger et al.,* [2000].

To assess solution quality when comparing the deviatoric inversion to the full inver-

sion, which has one more unknown parameter, we use the F-test [*Menke,* 1989]. With 200 seconds of data, 4 stations, 3 components at each station, and assuming a 20 s correlation length for the filtered data, and taking into account 5 unknowns in the deviatoric inversion, and 6 unknowns in the full moment tensor inversion, the critical values for the F ratio ($\sigma^2_{dev}/\sigma^2_{full}$) are 1.14, 1.36 and 1.55 at the 75%, 95% and 99% confidence levels respectively.

5.3   Results

There are many ways to decompose a moment tensor. Throughout this paper, we use the DC, CLVD and isotropic decomposition, which requires that the P and T axes of each component have the same orientation [*Jost and Hermann,* 1989; *Knopoff and Randall,* 1970].

In order to test the limits of the method in the absence of near-source velocity heterogeneity, synthetic data was calculated using E3D with only the AveTomo model. The same model was used to calculate the inversion kernels with the FKI technique with a 0.5 km source depth mismatch caused by a limitation in the FKI code (where the source cannot lie at a boundary with differing media properties). For mechanisms with no input isotropic component, the inversion recovered from 1% to 9% isotropic component with F ratios ranging from 1 to 1.04, indicating less than 75% significant improvement in fit relative to the deviatoric inversion. Mechanisms closely matched input mechanisms with rotations of the P and T axes of less than 7°. These differences are attributed to the differences in source depth and in the method used to compute synthetic data and inversion kernels. A notable exception is an input vertical CLVD, which as expected due to its similar radiation pattern to a purely isotropic source, recovered slightly higher isotropic component (14%) at a higher F ratio of 1.14 indicating just over 75% significance. Tests with input isotropic components all recovered

significant amounts of isotropic component (though less than the input amount due to contamination with a vertical CLVD) at greater than 99% significance. Inversion of a purely explosive input source resulted in 63% vertical CLVD, but the remaining isotropic component improved the data fit very significantly with an F ratio of 5.13.

Results for the tests with the input 3D LVC velocity and density model are shown in Table 5.2. While one inversion for a source at a depth of 3 km with no input isotropic component shows a 17% isotropic component, this result only shows a slight improvement in variance reduction over the deviatoric inversion, with no significant improvement in data fit by the F test criteria. For all deeper sources, the results are similar to the tests with no 3D structure, possibly corresponding to a decrease in heterogeneity of the tomographic model below 4 km depth. Rotations of the P and T axes (ΔP & ΔT) are small with the exception of the unconstrained P axes in the CLVD sources used. For the sources with an isotropic component, the amount is underestimated to a similar degree as in the test runs, and the full inversion shows improvement in fit to the data with 99% significance.

We also looked at the results when the data was inverted using Green's functions calculated from the SoCal model [*Dreger and Helmberger,* 1993] (Figure 5.2). This model is quite different than AveTomo, but synthetic seismograms in the low frequency passband are similar (Figure 5.3). The inversion results and F ratios for tests using these Green's functions are summarized in Table 5.3. As might be expected from less accurate Green's functions, the recovered moment tensors do not match the input as well as shown by the greater ΔP and ΔT values, but most inversions recovered similar isotropic component as discussed earlier. The rotations of the P and T axes also were not enough to change the nature of the mechanism (i.e. strike-slip, normal, reverse). The shallow (3 km) strike-slip and CLVD mechanisms, however, both produced higher isotropic component (29% and 28% respectively), but the F ratios are near unity, indicating little significance for the isotropic component. This demonstrates the method employed in *Dreger et al.* [2000] is a useful tool to recover mechanisms with real isotropic components.
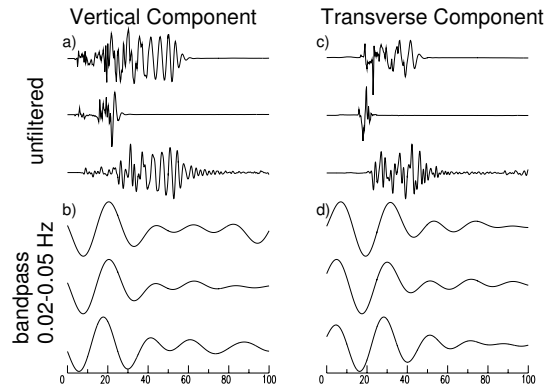
Figure 5.3: Comparison of synthetic seismograms calculated for a normal mechanism from the AveTomo model (top trace), SoCal model (middle trace), and 3D tomographic model (bottom trace) for both unfiltered data and in the passband used in the inversion for the vertical component (a and b) and the transverse component (c and d). The 3D model unfiltered data was convolved with a normalized 2 s gaussian source-time function in the finite difference code. All seismograms are for station 3 (see figure 5.1).

5.4 Conclusions

False recovery of isotropic components due to severe 3D velocity heterogeneity is not a significant effect in the passband tested, and therefore cannot explain the large isotropic component in the 1997 LVC events recovered by *Dreger et al.,* [2000], which appear to be real features of the source process. If 3D structure did effect a bias, then moment tensor inversions of synthetic data would result in large isotropic components and significantly decrease the data variance. Even the few inversions which resulted in an isotropic component greater than 10%, however, were not shown to be a significant improvement in fit over the deviatoric inversion at even a 75% confidence level. This is in marked contrast to the inversions performed on the actual LVC data, which recovered isotropic components between 27% to 42% with greater than 90% significance measured by the F-test [*Dreger et al.,* 2000].

While the results described above certainly appear to indicate that structural com-
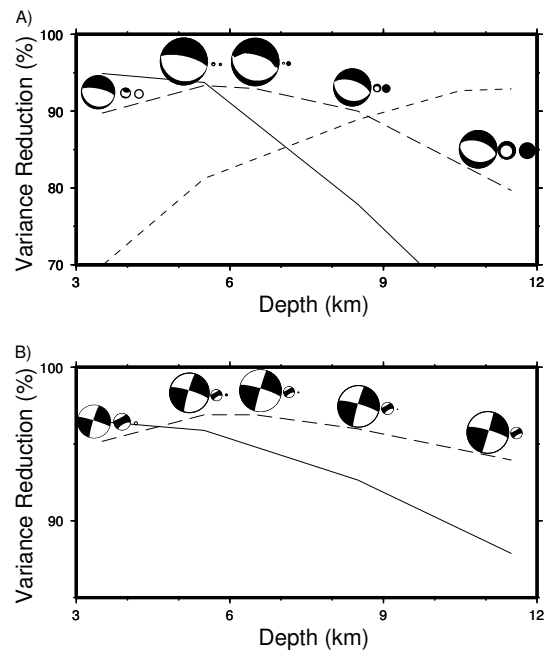
Figure 5.4: Percentage variance reduction versus source depth of the kernels used in the moment tensor inversion (using the SoCal model) for normal (a) and strike-slip (b) mechanisms for 3 km (solid line), 6 km (dashed line), and 10 km (dotted line) actual source depths. Recovered double-couple, CLVD, and isotropic components are shown scaled to moment for tests with 6 km actual source depth.

Table 5.1: Input Mechanisms

No.	Type	Depth	%DC/CLVD/ISO
1	Strike-slip	3	100/0/0
2	Strike-slip	6	100/0/0
3	Normal	3	100/0/0
4	Normal	6	100/0/0
5	Normal	10	100/0/0
6	Hor. CLVD	3	0/100/0
7	Hor. CLVD	6	0/100/0
8	Ver. CLVD	6	0/100/0
9	DC/ISO	6	57.1/0/42.9
10	CLVD/ISO	6	0/57.4/42.6
11	DC/CLVD/ISO	6	21.4/39/4/39.3
12	Explosion	6	0/0/100

Summary of the different input source mechanisms used
in all runs. Numbers are same as used in following tables.

plexity alone can not be responsible for the observed isotropic component of events in the 1997 swarm, there are other sources of bias that should be explored. For example, previous studies on the observability of the various components of the moment tensor [*Patton and Aki,* 1979; *Kawakatsu,* 1996; *Dufumier and Rivera,* 1997] have suggested that errors in event location can lead to significant bias in inversion results. To explore this, we performed inversions using Green's functions calibrated for sources at different depths in the SoCal model (Figure 5.4). While the amount of isotropic component recovered increased for incorrect depths (decompositions of the recovered moment tensors are shown for the tests with actual source depth of 6 km), the variance reduction is at a maximum around the correct source depth suggesting that spurious isotropic component can be minimized by carefully testing the source depth in this manner. The effects of finite faults in severe near-source structural heterogeneity, including rupture on non-parallel planes, is another source of bias that should be investigated.

	Deviatoric Inversion				Full Inversion				
No.	%DC/CLVD/ISO	VR	ΔT	ΔP	%DC/CLVD/ISO	VR	ΔT	ΔP	F Ratio
1	87/13/0	96.5	2	1.4	90/2/8	96.5	3	1	1.01
2	78/22/0	96.9	10	6.3	78/20/2	96.9	10	6.3	1.00
3	95/5/0	94.9	5.1	5.5	77/12/11	95.2	7	7.4	1.06
4	97/3/0	92.9	3	3.1	91/3/7	93.2	4	4	1.04
5	97/3/0	92.7	1	1.1	98/1/1	92.7	1	1.1	1.00
6	5/95/0	96.5	2.2	25.2	14/69/17	96.7	2.2	81.8	1.06
7	32/68/0	96.3	1.4	30.1	28/67/5	96.3	1	34.1	1.00
8	4/96/0	90.2	3	40	3/87/10	90.8	3	42	1.07
9	60/40/0	93.5	13	43	56/13/31	96.6	14	60	1.96
10	84/16/0	93.9	30.1	1.4	45/23/32	96.6	52.2	1	1.84
11	49/51/0	90.3	7.1	15.9	29/46/26	95.3	9.4	18.8	2.10
12	6/94/0	73.5	n/a	n/a	1/62/36	93.9	n/a	n/a	4.41

Summary of deviatoric and full moment tensor inversion results using AveTomo to calculate the inversion kernels. Percentage double-couple, CLVD, and isotropic component are shown for each as well as the data variance reduction for the inversions. The percent CLVD is calculated from the minimum and maximum eigenvalues ($|\lambda_3| < |\lambda_2| < |\lambda_1|$), where $\varepsilon = |\lambda_1/\lambda_3|$ and %CLVD = 200ε and %DC = 100 - 200ε. The percent isotropic is the ratio of the isotropic moment to the sum of the isotropic and deviatoric moments. ΔT and ΔP refer to the angle (°) between input and recovered T and P axes. The F ratio ($\sigma^2_{dev}/\sigma^2_{full}$) for each input mechanism is also shown.

Table 5.3: SoCal Inversions

	Deviatoric Inversion				Full Inversion				
No.	%DC/CLVD/ISO	VR	ΔT	ΔP	%DC/CLVD/ISO	VR	ΔT	ΔP	F Ratio
1	99/1/0	92.6	34.4	4.9	40/31/29	92.8	26.3	16.3	1.04
2	52/48/0	93.5	31.6	10.2	54/36/10	93.6	28.4	12	1.01
3	92/8/0	88.8	3	4.7	92/6/2	88.8	2	3.7	1.00
4	86/14/0	89.6	2	2.4	68/21/11	90	4	4.4	1.04
5	91/9/0	86.7	1.4	1.6	73/18/9	87.4	1.3	1.6	1.06
6	57/43/0	92.9	16.7	42.7	53/20/28	93.3	10.4	61.1	1.08
7	55/45/0	93.7	13.1	34.5	48/43/10	93.8	11.2	39.7	1.01
8	2/98/0	92	4	49.1	2/84/13	92.2	5	54.1	1.03
9	77/23/0	88.5	26.5	37.5	57/5/38	93.2	20.2	59.1	1.75
10	84/16/0	89.6	29.5	11.7	52/11/37	92.7	55.8	4.5	1.44
11	56/44/0	88.2	7	15.3	29/41/20	92.8	11.2	20.7	1.69
12	3/97/0	69.5	n/a	n/a	0/55/45	93	n/a	n/a	4.65

Same as Table 5.2, with inversion kernels calculated with the SoCal model [*Dreger and Helmberger,* 1993].

Chapter 6

Conclusions

We used long-period waveforms to model 3D anisotropic mantle structure, as well as earthquake source processes on both a global and regional scale. Here we attempt to briefly summarize the findings of these studies.

We used normal mode asymptotic coupling theory to model 3 component body and surface waveforms. First we used the approach to develop a model of mantle radial anisotropy of shear velocity in order to focus on structure in the lowermost few hundred kilometers of the mantle, or D″. While the isotropic velocity was quite similar to other tomographic models of D″ structure, there were several notable features of the anisotropic portion of the model. Chiefly, there was a strong spherically symmetric signature of a positive perturbation to the anisotropic parameter ξ, meaning horizontally polarized shear waves travel faster than vertically polarized shear waves. The deviations from this signature were associated with the large low velocity superplumes, thought to be regions of large-scale upwelling. This suggests a model of the development of anisotropy in the predominantly horizontal flow of a mechanical boundary layer for mantle convection. However, the signature is changed when it approaches the large-scale upwellings through a variety of possible mechanisms.

We extended this approach to develop a multi-iteration model of anisotropic velocity in the whole mantle. This model confirmed the observations of the first modelling work on D″ structure, as well as previous results demonstrating the development of positive ξ anomalies beneath oceans beginning at ∼80 km and at greater depths beneath old continents, likely related to anisotropy generated in the strongly sheared zones beneath oceanic and continental lithosphere. Additionally, we observed a strong correlation of negative ξ anomalies with fast-spreading ridges between 200 and 300 km, and apparent negative ξ anomalies associated with subduction zones between 400 and 600 km. Anisotropy in mid-mantle depth ranges between 800 and 2000 km was generally low in amplitude, and did not strongly affect the fit to the data, consistent with previous work suggesting the bulk of the lower mantle is nearly isotropic. As part of this modelling, we also iteratively inverted for source parameters for the events in our dataset. While the changes in mechanism were small, we did see evidence of systematic relocations due to the improved structural model in the major subduction zones around the Pacific Ocean.

We also used a numerical technique to look at regional, rather than teleseismic, waveforms, and applied it to a different earthquake source modelling approach. We used a finite-difference code to model waveforms propagating through a very heterogeneous medium in the vicinity of the Long Valley Caldera, a volcanic region in eastern California. Using these synthetic waveforms and a set of known seismic sources, we performed source inversions utilizing Green's functions based on simple 1D velocity models. While the recovered source parameters showed some complications due to the unmodelled near-source velocity structure, they did not show statistically significant volumetric components. This lends support to earlier observations that some sources from an earthquake swarm in the late 1990's experienced volumetric expansion during the source process, with important implications for hydrothermal processes occuring during earthquakes in volcanically active regions.

There are, of course, many possible future directions of related research. The anisotropic modelling approach should be extended to include azimuthal anisotropy, as

well as incorporating higher degree resolution isotropic velocity models. Extending the approach to higher frequency waveforms would also allow for higher resolution, not only of velocity structure, but also of topography of the 670 discontinuity and the core-mantle boundary. As we rapidly expand our computing resources, the global modelling can also be approached with numerical techniques similar to that used for our regional case study, in order to help understand the effects of the assumptions made in the development of the mode-coupling theory.

Bibliography

Aki, K. and P.G. Richards, *Quantitative Seismology: Theory and Methods,* W. H. Freeman, New York, 1980.

Babuska, V. and M. Cara, *Seismic Anisotropy in the Earth*, Kluwer Academic Press, Boston, 1991.

Beghein, C. and J. Trampert, Probability density functions for radial anisotropy: implications for the upper 1200 km of the mantle, *Earth Planet. Sci. Lett.*, **217**, 151-162, 2003.

Beghein, C. and J. Trampert, Probability density functions for radial anisotropy from fundamental mode surface wave data and the Neighbourhood Algorithm, *Geophys. J. Int.*, **157**, 1163-1174, 2004.

Birch, A. F., The velocity of compressional waves in rocks to 10 kilobars; Part 2, *J. Geophys. Res.*, **66,** 2199-2224, 1961.

Boschi, L. and A. Dziewonski, Whole Earth tomography from delay times of P, PcP, PKP phases: lateral heterogeneities in the outer core, or radial anisotropy in the mantle?, *J. Geophys. Res.*, **104**, 25,267-25,594, 2000.

Dahlen, F.A. and J. Tromp, *Theoretical Global Seismology,* Princeton Univ. Press, Princeton, New Jersey, 1998.

Daradich, A., J.X. Mitrovica, R.N. Pysklywec, S.D. Willett and A.M. Forte, Mantle flow, dynamic topography, and rift-flank uplift of Arabia , *Geology*, **30**, 901-904, 2003.

DeMets, C., R.G. Gordon, D.F. Argus and S. Stein, Current plate motions, *Geophys. J. Int.*, **101**, 425-478, 1990.

Dreger, D. and D. V. Helmberger, Determination of source parameters at regional distances with single station or sparse network data, *J. Geophys. Res.*, **98,** 8107-8125, 1993.

Dreger, D., H. Tkalčić, and M. Johnston, Dilational processes accompanying earthquakes in the Long Valley caldera, *Science,* **288,** 122-125, 2000.

Dufumier, H. and L. Rivera, On the resolution of the isotropic component of a moment tensor, *Geophys. J. Int.,* **131,** 595-606, 1997.

Dziewonski, A.M. and D.L. Anderson, Preliminary Reference Earth Model, *Phys. Earth planet. Inter.*, **25,** 297-356, 1981.

Dziewonski, A.M. and J.H. Woodhouse, Studies of the seismic source using normal-mode theory, in *Earthquakes: observation, theory and interpretation*, pp. 45-137, eds. Kanamori, H. and E. Boschi, North-Holland Publ. Co., Amsterdam, 1983.

Edmonds, A.R., *Angular momentum in quantum mechanics*, Princeton University Press, Princeton, New Jersey, 1960.

Efron, B. and R.J. Tibishirani, *An Introduction to Bootstrap*, Chapman and Hall, New York, 1993.

Ekström, G. and A.M. Dziewonski, The unique anisotropy of the Pacific upper mantle, *Nature,* **394,** 168-172, 1998.

Fouch, M.J. and K.M. Fischer, Mantle anisotropy beneath northwest Pacific subduction zones, *J. Geophys. Res.*, **101**, 15,987-16,002, 1996.

Fouch, M.S., K.M. Fischer and M.E. Wysession, Lowermost mantle anisotropy beneath the Pacific: Imaging the source of the Hawaiian plume, *Earth Planet. Sci. Lett.*, **190,** 167-180, 2001.

Fung, Y.C., *Foundations of solid mechanics*, Prentice-Hall, Inc., Englewood Cliffs, New Jersey, 1965.

Garnero, E.J. and T. Lay, Lateral variations in lowermost mantle shear wave anisotropy beneath the north Pacific and Alaska, *J. Geophys. Res.*, **102**, 8121-8135, 1997.

Gilbert, F., Excitation of the normal modes of the Earth by earthquake sources, *Geophys. J. R. Astr. Soc.*, **22**, 223-226, 1971.

Graves, R.W., Modeling three-dimensional site response effects in the Marina district basin, San Francisco, California, *Bull. Seism. Soc. Am.*, **83**, 1042-1063, 1993.

Gu, Y.J., A.M. Dziewonski, W. Su, and G Ekström, Models of the mantle shear velocity and discontinuities in the pattern of lateral heterogeneities, *J. Geophys. Res.*, **106,** 11,169-11,199, 2001.

Gung, Y., *Lateral variations in attenuation and anisotropy of the upper mantle from seismic waveform tomography*, Ph.D. thesis, University of California at Berkeley, Berkeley, CA, 2003.

Gung, Y. and B. Romanowicz, Q tomography of the upper mantle using three-component long-period waveforms , *Geophys. J. Int.*, **157,** 813-830, 2004.

Gung, Y., M. Panning and B. Romanowicz, Global anisotropy and the thickness of continents, *Nature*, **422,** 707-711, 2003.

Grand, S., Global seismic tomography: a snapshot of convection in the Earth, *GSA Today*, **7**, 1-7, 1997.

Hager, B.H., Subducted slabs and the geoid - constraints on mantle rheology and flow, *J. Geophys. Res.*, **89**, 6003-6015, 1984.

Hall, C.E., K.M. Fischer, E.M. Parmentier and D.K. Blackman, The influence of plate motions on three-dimensional back arc mantle flow and shear wave splitting, *J. Geophys. Res.*, **105**, 28,009-28,033, 2000.

Hess, H., Seismic anisotropy of the uppermost mantle under oceans, *Nature*, **203**, 629-631, 1964.

Iitaka, T., K. Hirose, K. Kawamura and M. Murakami, The elasticity of the MgSiO$_3$ post-perovskite phase in the Earth's lowermost mantle, *Nature*, **430**, 442-445, 2004.

Jordan, T.H., A procedure for estimating lateral variations from low-frequency eigenspectra data, *Geophys. J. R. Astr. Soc.*, **52**, 441-455, 1978.

Jost, M. L. and R. B. Hermann, A student's guide to and review of moment tensors, *Seismol. Res. Lett.,* **60,** 37-57, 1989.

Julian, B. R., Evidence for dyke intrusion earthquake mechanisms near Long Valley caldera, California, *Nature,* **303,** 323-325, 1983.

Julian, B. R. and S. A. Sipkin, Earthquake processes in the Long Valley caldera area, California, *J. Geophys. Res.*, **90,** 11,155-1,169, 1985.

Kanamori, H., The energy release in great earthquakes, *J. Geophys. Res.*, **82**, 2981-2987, 1977.

Karato, S.-I., Some remarks on the origin of seismic anisotropy in the D" layer, *Earth Planets Space*, **50,** 1019-1028, 1998a.

Karato, S.-I., Seismic anisotropy in the deep mantle, boundary layers and the geometry of mantle convection, *Pure Appl. Geophys.*, **151**, 565-587, 1998b.

Kawakatsu, H., Observability of the isotropic component of a moment tensor, *Geophys. J. Int.,* **126,** 525-544, 1996.

Kawasaki, I. and F. Konno, Azimuthal anisotropy of surface waves and the possible type of seismic anisotropy due to preferred orientation of olivine in the uppermost mantle beneath the Pacific ocean, *J. Phys. Earth*, **32**, 229-244, 1984.

Kendall, J.-M. and P.G. Silver, Constraints from seismic anisotropy on the nature of the lowermost mantle, *Nature,* **381,** 409-412, 1996.

Knittle, E. and R. Jeanloz, Earth's core-mantle boundary; results of experiments at high pressures and temperatures, *Science,* **251,** 1438-1443, 1991.

Knopoff, L. and M. J. Randall, The compensated linear-vector dipole: A possible mechanism for deep earthquakes, *J. Geophys. Res.*, **75,** 4957-4963, 1970.

Larsen, S. and C. A. Schulz, ELAS3D: 2D/3D elastic finite-difference wave propagation code, *Technical Report No. UCRL-MA-121792,* 19 pp., 1995.

Lay, T. and D.V. Helmberger, The shear-wave velocity gradient at the base of the mantle, *J. Geophys. Res.*, **88**, 8160-8170, 1983.

Lay, T., Q. Williams and E.J. Garnero, The core-mantle boundary layer and deep Earth dynamics, *Nature*, **392**, 461-468, 1998a.

Lay, T., Q. Williams and E.J. Garnero, L. Kellogg and M.E. Wysession, Seismic wave anisotropy in the D" region and its implications, in *The Core-Mantle Boundary Region*, pp. 299-318, eds. Gurnis, M., M.E. Wysession, E. Knittle and B. Buffett, Amer. Geophys. Union, Washington, D.C., 1998b.

Levander, A., Fourth-order finite-difference P-SV seismograms, *Geophysics*, **53**, 1425-1436, 1988.

Li, X.D. and T. Tanimoto, Waveforms of long-period body waves in a slightly aspherical Earth model, *Geophys. J. R. Astr. Soc.*, **112**, 92-102, 1993.

Li, X.D. and B. Romanowicz, Comparison of global waveform inversions with and without considering cross-branch modal coupling, *Geophys. J. Int.*, **121**, 695-709, 1995.

Li, X.D. and B. Romanowicz, Global mantle shear velocity model developed using nonlinear asymptotic coupling theory, *J. Geophys. Res.*, **101**, 22,245-22,272, 1996.

Lithgow-Bertelloni, C. and M.A. Richards, The dynamics of Cenozoic and Mesozoic plate motions, *Rev. Geophys.*, **36**, 27-78, 1998.

Love, A.E.H., *A Treatise on the Theory of Elasticity*, Cambridge Univ. Press, Cambridge, 1927.

Masters, G., S. Johnson, G. Laske and H. Bolton, A shear-velocity model of the mantle, *Philos. Trans. R. Soc. London Ser. A*, **354**, 1385-1411, 1996.

Masters, G., G. Laske, H. Bolton and A. Dziewonski, The relative behavior of shear velocity, bulk sound speed, and compressional velocity in the mantle: implications for chemical and thermal structure, in *Earth's Deep Interior*, AGU Monograph 117, pp. 63-86, eds. Karato, S., A.M. Forte, R.C. Liebermann, G. Masters and L. Stixrude, Amer. Geophys. Union, Washington, D.C., 2000.

Matzel, E., K. Sen and S.P. Grand, Evidence for anisotropy in the deep mantle beneatch Alaska, *Geophys. Res. Lett.*, **23**, 2417-2420, 1997.

McEvilly, T.V., Central U.S. crust-upper mantle structure from Love and Rayleigh wave phase velocity inversion, *Bull. Seism. Soc. Am.*, **54**, 1997-2015, 1964.

McNamara, A.K., P.E. van Keken, and S.-I. Karato, Development of anisotropic structure in the Earth's lower mantle by solid-state convection, *Nature*, **416**, 310-314, 2002.

Meade, C., P.G. Silver and S. Kaneshima, Laboratory and seismological observations of lower mantle isotropy, *Geophys. Res. Lett.*, **22**, 1293-1296, 1995.

Mégnin, C., *The shear velocity structure of the mantle from the inversion of time-domain waveform data*, Ph.D. thesis, University of California at Berkeley, Berkeley, CA, 1999.

Mégnin, C. and B. Romanowicz, The 3D shear velocity structure of the mantle from the inversion of body, surface and higher mode waveforms, *Geophys. J. Int.*, **143**, 709-728, 2000.

Menke, W. H., *Geophysical Data Analysis: Discrete Inverse Theory, Revised Ed.*, Academic Press, Inc., New York, 1989.

Mochizuki, E., The free oscillations of an anisotropic and heterogeneous Earth, *Geophys. J. R. Astr. Soc.*, **86,** 167-176, 1986.

Moczo, P., J. Kristek, and L. Halada, 3D fourth-order staggered-grid finite-difference schemes: Stability and grid dispersion, *Bull. Seism. Soc. Am.*, **90,** 587-603, 2000.

Montagner, J.-P. and D.L. Anderson, Petrological constraints on seismic anisotropy, *Phys. Earth planet. Inter.*, **54**, 82-105, 1989.

Montagner, J.-P. and B.L.N. Kennett, How to reconcile body-wave and normal-mode reference earth models, *Geophys. J. Int.*, **125**, 229-248, 1996.

Montagner, J.-P. and J. Ritsema, Interactions between ridges and plumes, *Science*, **294**, 1472-1473, 2001.

Montagner, J.-P. and T. Tanimoto, Global upper mantle tomography of seismic velocities and anisotropies, *J. Geophys. Res.*, **96,** 20,337-20,351, 1991.

Mooney W.D., G. Laske and G. Masters, Crust 5.1: a global crustal model at $5\deg \times 5\deg$, *J. Geophys. Res.*, **103,** 727-747, 1998.

Morelli, A. and A.M. Dziewonski, Topography of the core-mantle boundary and lateral homogeneity of the liquid core, *Nature*, **325,** 678-683, 1987.

Nataf, H.-C., I. Nakanishi and D.L. Anderson, Measurements of mantle wave velocities and inversion for lateral heterogeneities and anisotropy: 3. inversion, *J. Geophys. Res.*, **91**, 7261-7307, 1986.

Panning, M.P.and B. Romanowicz, Inferences on flow at the base of Earth's mantle based on seismic anisotropy, *Science*, **303,** 351-353, 2004a.

Panning, M.P. and B. Romanowicz, A three dimensional radially anisotropic model of shear velocity in the whole mantle, submitted to *Geophys. J. Int.*, 2004b.

Panning, M.P., D. Dreger, and H. Tkalčić, Near-source velocity structure and isotropic moment tensors: a case study of the Long Valley Caldera, *Geophys. Res. Lett.*, **28,** 1815-1818, 2001.

Park, J., Asymptotic coupled mode expressions for multiplet amplitude anomalies and frequency shifts on an aspherical Earth, *Geophys. J. R. Astr. Soc.*, **90**, 129-169, 1987.

Pasyanos, M. E., D. Dreger, and B. Romanowicz, Towards real-time estimation of regional moment tensors, *Bull. Seism. Soc. Am.*, **86,** 1255-1269, 1996.

Patton, H. and K. Aki, Bias in the estimate of seismic moment tensor by the linear inversion method, *Geophys. J. R. Astr. Soc.*, **52,** 359-364, 1979.

Phinney, R.A. and R. Burridge, Representation of the elastic-gravitational excitation of a spherical earth model by generalized spherical harmonics, *Geophys. J. R. Astr. Soc.*, **34**, 451-487, 1973.

Pulliam, J and M.K. Sen, Seismic anisotropy in the core-mantle transition zone, *Geophys. J. Int.*, **135**, 113-128, 1998.

Rayleigh, Lord, *The Theory of Sound*. New York: Dover Publication, 1945.

Revenaugh, J. and T.H. Jordan, Observations of first-order mantle reverberations, *Bull. Seism. Soc. Am.*, **77**, 1704-1717, 1987.

Ricard, Y. and C. Vigny, Mantle dynamics with induced plate tectonics, *J. Geophys. Res.*, **94**, 17,543-17,560, 1989.

Ritsema, J. and H.-J. van Heijst, Seismic imaging of structural heterogeneity in Earth's mantle: evidence for large-scale mantle flow, *Science Progress*, **83**, 243-259, 2000.

Romanowicz, B., Multiplet-multiplet coupling due to lateral heterogeneity: asymptotic effects on the amplitude and frequency of Earth's normal modes, *Geophys. J. R. Astr. Soc.*, **90**, 75-100, 1987.

Romanowicz, B. and Y. Gung, Superplumes from the core-mantle boundary to the lithosphere: implications for heat flux, *Science*, **296**, 513-516, 2002.

Romanowicz, B. and G. Roult, First order asymptotics for the eigenfrequencies of the Earth and application to the retreival of large-scale lateral variations of structure, *Geophys. J. R. Astr. Soc.*, **87**, 209-239, 1986.

Romanowicz, B. and R. Snieder, A new formalism for the effect of lateral heterogeneity on normal modes and surface waves-II. General anisotropic perturbation, *Geophys. J. Int.*, **93**, 91-99, 1988.

Romanowicz, B., M. Cara, J.F. Fels and D. Rouland, Geoscope: a French initiative in long-period three-component global seismic networks, *EOS Trans. AGU*, **65,** 753-754, 1984.

Russell, S.A., T. Lay and E.J. Garnero, Small-scale lateral shear velocity and anisotropy heterogeneity near the core-mantle boundary beneath the central Pacific imaged using broadband ScS waves, *J. Geophys. Res.*, **104,** 13,183-13,199, 1999.

Silver, P.G., Seismic anisotropy beneath the continents: probing the depths of geology, *Annu. Rev. Earth Planet. Sci.*, **24**, 385-432, 1996.

Smith, S.W., IRIS: a program for the next decade, *EOS Trans. AGU*, **67,** 213-219, 1986.

Stixrude, L., Elastic constants and anisotropy of $MgSiO_3$, perovskite, periclase, and SiO_2 at high pressure, in *The Core-Mantle Boundary Region*, pp. 83-96, eds. Gurnis, M., M.E. Wysession, E. Knittle and B. Buffett, Amer. Geophys. Union, Washington, D.C., 1998.

Tanimoto, T., A simple derivation of the formula to calculate synthetic long-period seismograms in a heterogeneous earth by normal mode summation, *Geophys. J. R. Astr. Soc.*, **77**, 275-278, 1984.

Tanimoto, T. and D.L. Anderson, Lateral heterogeneity and azimuthal anisotropy of the upper mantle: Love and Rayleigh waves 100-250 s, *J. Geophys. Res.*, **90**, 1842-1858, 1985.

Tarantola, A. and Valette, B., Generalized nonlinear inverse problems solved using the least squares criterion, *Rev. Geophys. Space Phys.*, **20**, 219-232, 1982.

Thomas, C. and J.-M. Kendall, The lowermost mantle beneath northern Asia; II, Evidence for lower-mantle anisotropy, *Geophys. J. Int.*, **151,** 296-308, 2002.

Trampert, J. and H.J. van Heijst, Global azimuthal anisotropy in the transition zone, *Science*, **296**, 1297-1299, 2002.

Tsuchiya, T., J. Tsuchiya, K. Umemoto and R.M. Wentzcovitch, Elasticity of post-perovskite MgSiO$_3$, *Geophys. Res. Lett.*, **31**, L14603, doi:10.1029/2004GL020278, 2004.

Vinnik, L.P., V. Farra and B.A. Romanowicz, Observational evidence for diffracted SV in the shadow of the Earth's core, *Geophys. Res. Lett.*, **16,** 519-522, 1989.

Vinnik, L.P., L.I. Makeyeva, A. Milev and Y. Usenko, Global patterns of azimuthal anisotropy and deformations in the continental mantle, *Geophys. J. Int.*, **111**, 433-447, 1992.

Wallace, T., A reexamination of the moment tensor solutions of the 1980 Mammoth Lakes earthquakes, *J. Geophys. Res.*, **90,** 11,171-11,176, 1985.

Woodhouse, J.H., The coupling and attenuation of nearly resonnant multiplets in the earth's free oscillation spectrum, *Geophys. J. R. Astr. Soc.*, **61**, 261,283, 1980.

Woodhouse, J.H., The joint inversion of seismic wave forms for lateral variations in Earth structure and earthquake source parameters, in *Earthquakes: observation, theory and interpretation*, pp. 366-397, eds. Kanamori, H. & Boschi, E., North-Holland Publ. Co., Amsterdam., 1983.

Woodhouse, J.H. and A.M. Dziewonski, Mapping the upper mantle: Three dimensional modeling of Earth's structure by inversion of seismic waveforms, *J. Geophys. Res.*, **89**, 5,953-5,986, 1984.

Woodhouse, J.H. and T.P. Girnius, Surface waves and free oscillations in a regionalized earth model, *Geophys. J. R. Astr. Soc.*, **68**, 653-673, 1982.

Woodward, R.L., A.M. Forte, W.J. Su and A.M. Dziewonski, Constraints on the large-scale structure of the Earth's mantle, in *Evolution of the Earth and Planets*, pp. 89-109, eds. Takahashi, E., R. Jeanloz and D. Rubie, Amer. Geophys. Union, Washington, D.C, 1993.

Wysession, M.E., K.M. Fischer, G.I. Al-eqabi, P.J. Shore and I. Gurari, Using MOMA broadband array ScS-S data to image smaller-scale structures at the base of the mantle, *Geophys. Res. Lett.*, **28,** 867-870, 2001.

Appendix A

Automatic wavepacket picking algorithm

The early models developed using *NACT* (section 2.3), were constructed using only transverse (T) component data [*Li and Romanowicz,* 1996; *Mégnin and Romanowicz,* 2000], the component of horizontal motion perpendicular to the great circle path between source and receiver. Because of the relative simplicity of these waveforms, the wavepackets used in these inversions were picked by hand. Because there is no coupling with P energy, the body wave phases are, in general, well isolated, allowing for quick visual assessment of data quality and definition of wavepacket windows utilizing an interactive approach.

To develop anisotropic models, such as those developed in chapters 3 and 4, we need wavepackets from all three components. The longitudinal (L) component (horizontal motion parallel with the great circle path) and vertical (Z) component of motion measure motion of the coupled P-SV system. There are many more body wave phases on these records, as we have P phases, as well as P to S conversions such as phases that travel through the fluid outer core, and conversions at the free surface and mantle discontinuities, which are not present on the T component. Picking isolated

wavepackets is very difficult, and the definition of wavepacket windows to maximize sensitivity can be a very time-consuming task if done by hand.

In order to gather a sufficient dataset of L and Z component body waveform data, we developed an automatic wavepacket picking algorithm to speed acquisition, although we review each wavepacket visually to insure data quality.

The dataset includes events from 1995 to 1999 recorded on the IRIS and GEOSCOPE networks. We use events with M_W greater than 5.5, but do not use events with seismic moment greater than 10^{20} Nm ($M_W > 7.3$) in order to avoid complications from long source-time functions. We also do not use traces within 15° of the source or the antipode, as the asymptotic calculations break down in these regions. All traces matching these criteria are then filtered to the frequency band used in the inversions. For the body waves, the short period cutoff is 32 s at present, while the long period cutoff is a function of the earthquake magnitude and ranges from 220 seconds to 1 hour.

Each trace is then processed to select the wavepackets to be used in the inversion. First synthetics are calculated using the PREM model [*Dziewonski and Anderson, 1981*]. We define the two quantities

$$RMSR = \frac{\sum_{i=1}^{N}(d_i - s_i) \cdot (d_i - s_i)}{\sum_{i=1}^{N} d_i^2} \tag{A.1}$$

$$RMSS = \frac{\sum_{i=1}^{N}(d_i - s_i) \cdot (d_i - s_i)}{\sum_{i=1}^{N} s_i^2}, \tag{A.2}$$

where N is the number of data points, d_i is the ith data point, and s_i is the ith point in the synthetic trace. Data which has either of these values too large is rejected, as it is either noisy, has an incorrect instrument response, contains glitches, or is strongly affected by focussing or defocussing which we do not model in our theoretical approach.

Traces are then divided into wavepackets based on the predicted travel times of several phases. Examples of the defined wavepackets windows are shown in figures A.1 and A.2. Wavepackets are mostly defined in the window starting just before the predicted first arrival (P, P$_{\text{diff}}$, or PKP) and ending just before the Rayleigh wave. For events deeper than 200 km and epicentral distances between 40º and 90º, we also pick wavepackets in a window after the Rayleigh wave, which contains multiple ScS phases in the reverberative interval [*Revenaugh and Jordan*, 1987] between the 1st and 2nd orbit Rayleigh waves (Fig. A.2).

After the wavepacket windows are defined, each packet is analyzed for data quality, using a number of criteria. First, we calculate the $RMSR$ and $RMSS$ values, and reject packets if either value is greater than 4.0. We also calculate the ratio of maximum data and synthetic amplitudes, and reject the wavepacket if this value is greater than 2.5 or less than 0.4. A correlation coefficient is also calculated, and data is rejected if it is less than 0. Finally the packet is analyzed using a moving window approach which helps eliminate data with persistent low level noise. The $RMSR$ and $RMSS$ values for each packet are stored, and are utilized in the *a priori* data covariance matrix [*Tarantola and Valette,* 1982], which is used to apply a weighting scheme to account for data noise and redundancy [*Li and Romanowicz,* 1996].

This data selection process eliminates approximately 50% of the available data, and stricter criteria can be applied on the $RMSR$ and $RMSS$ values at the time of inversion, if desired. This scheme allows us to gather data much more quickly, although we do review each packet visually to verify its quality. A similar algorithm is used for the picking of surface wavepackets used in the inversion [*Gung*, 2003].
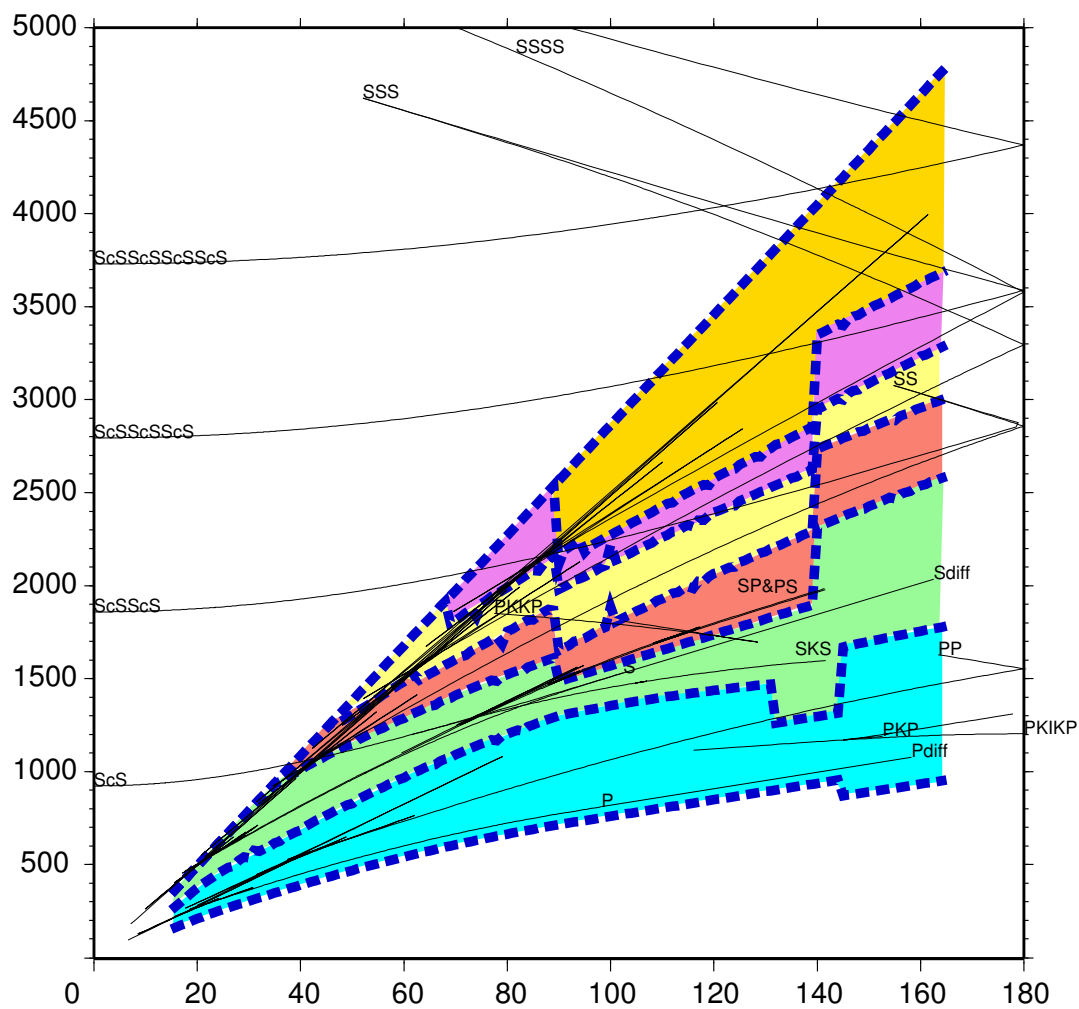
Figure A.1: Wavepacket windows as a function of epicentral distance for events with depth less than 200 km.
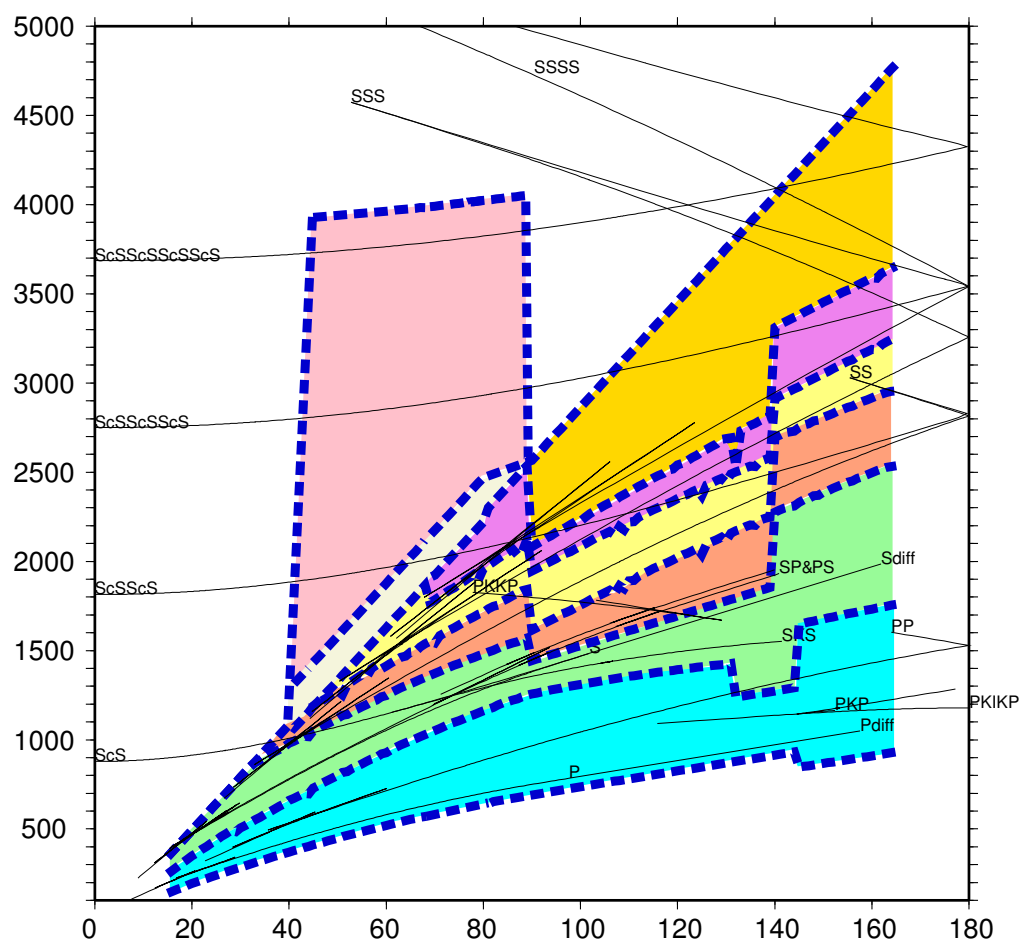
Figure A.2: Wavepacket windows as a function of epicentral distance for events with depth greater than 200 km.